

**INTERFACE CIRCUITS FOR READOUT AND CONTROL OF A  
MICRO-HEMISPHERICAL RESONATING GYROSCOPE**

A Thesis  
Presented to  
The Academic Faculty

by

Curtis Mayberry

In Partial Fulfillment  
of the Requirements for the Degree  
Master of Science in the  
School of Electrical and Computer Engineering

Georgia Institute of Technology  
December 2014

**COPYRIGHT © CURTIS MAYBERRY 2014**

**INTERFACE CIRCUITS FOR READOUT AND CONTROL OF A  
MICRO-HEMISPHERICAL RESONATING GYROSCOPE**

Approved by:

Dr. Farokh Ayazi, Advisor  
School of Electrical and Computer Engineering  
*Georgia Institute of Technology*

Dr. Maysam Ghovanloo  
School of Electrical and Computer Engineering  
*Georgia Institute of Technology*

Dr. Hua Wang  
School of Electrical and Computer Engineering  
*Georgia Institute of Technology*

Date Approved: December 4, 2014

To my family and friends.  
My father Kevin Mayberry.  
My mother Patricia Mayberry.  
My fiancé Alicia Hendrix.

## ACKNOWLEDGEMENTS

I would like to thank Dr. Ayazi for his encouragement and support. As an instructor he provided a great introduction to the multi-disciplinary world of MEMS. As an advisor, he has been able to give me the independence I needed to complete my own work and explore new ideas while also providing support and encouragement. He has helped me grow professionally and I am very thankful to have him as an advisor and for the chance to be a part of IMEMS.

I would like to thank my teammates that have worked with me on the development of the  $\mu$ HRG. Peng Shao for his development and fabrication of the  $\mu$ HSR. Benoit Hamelin for his efforts on trimming and fabrication methods for the  $\mu$ HSR. Dr. Vahid Tavassoli, Dr. Logan Sorenson, and Xin Gao for their contributions to the design of the  $\mu$ HSR. Chang-shun Liu for his early work on the analog front-end design and ring-down measurements. Bhaskar Balachander for his assistance with resonator characterization and ring-down measurements.

I would also like to thank all members of the IMEMS lab for building a great place to learn and develop the next generation of integrated MEMS technology. Specifically I'd like to thank Arashk Norouz Pour Shirazi for his guidance and support. Mojtaba Hodjat-Shamami for being a patient TA while I was first learning about MEMS. Sam Wisher, Roozbeh Tabrizian, Anosh Daruwalla, Ramin Mirjalili and Haoran Wen for their friendship and the many discussions and moments of entertainment that make IMEMS a great place to work.



IMEMS Group, fall 2013

I would like to thank Northrop Grumman and the DARPA microsystems Technology Office for financial support for development of the  $\mu$ HRG through the MRIG program. I would also like to thank James Pavell at Northrop-Gruman for his work on the on-board vacuum chamber. Along with Grant Atikyan, Alexander Trusov, and Dave Rozelle at Northrop Grumman for their support and input to the program.

I would also like to thank my family, friends that have made an immeasurable impact on my life. I would like to thank my mother, Patricia Mayberry, who works so hard to build a family where all five of her children could grow and prosper. I would like to thank my father who always encouraged me and let me know I could achieve anything I wanted to, taught me self-reliance, and started my early interest in engineering. I am also am thankful for the patience and support of my fiancé, Alicia Hendrix. She was understanding of my commitment to my schoolwork and research and without her

support this work would not have been possible. Finally I would like to thank all my friends and teachers who have helped me throughout my life.

# TABLE OF CONTENTS

ACKNOWLEDGEMENTS	iv
LIST OF TABLES	xi
LIST OF FIGURES	xii
LIST OF EQUATIONS	xvi
LIST OF ABBREVIATIONS	xviii
LIST OF SYMBOLS	xxi
SUMMARY	xxiv
Chapter 1 Introduction to MEMS Gyroscopes and the micro-Hemispherical Shell Gyroscope	1
1.1 Applications of Gyroscopes	3
1.2 Micro-hemispherical Shell Resonator Background	5
1.2.1 Gyroscope History	5
1.2.2 Coriolis Vibratory Gyroscope Operating Principles	7
1.2.3 Existing MEMS Technologies	8
1.2.4 Micro-hemispherical Shell Resonator ( $\mu$ HSR)	9
1.3 $\mu$ HRG Gyroscope Performance Characterization	12
1.3.1 Scale Factor and Sensitivity	12
1.3.2 Resolution	13
1.3.3 Allan Variance	13
1.3.4 Bandwidth	16
1.3.5 Dynamic Range	16
1.4 Gyroscope Interface Methods Background	16
1.4.1 System Architectures	17
1.4.2 Whole-angle mode	19

1.4.3	Analog Front-end Designs	19
1.4.4	Mode Matching	21
1.4.5	Quadrature Compensation	23
1.4.6	Automatic Gain Control	23
1.4.7	Bias Drift Compensation	27
Chapter 2 $\mu$ HRG Rate Interface Design and Analysis		29
2.1	Device Characterization	29
2.1.1	Frequency Response and Frequency Split	29
2.1.2	Matched Frequency Response and Modelling	30
2.1.3	Ring-down Measurements	31
2.1.4	Linearity	34
2.1.5	Substrate Feed-through Effects	36
2.2	$\mu$ HSR Model	37
2.2.1	Drive Mode Analysis: First Order Model	38
2.2.2	Device Electrostatic Interface	39
2.2.3	Drive Forcer Electrodes	40
2.2.4	Modal Dynamics	41
2.2.5	Drive Pickoff Electrodes	42
2.2.6	Electrical Model	43
2.2.7	Sense Mode Analysis: Second Order Model	45
2.3	Analog Front-End	47
2.3.1	Pick-off Channels	48
2.3.2	Forcer Channels	52
2.3.3	Feed-through Cancellation Channels	53
2.3.4	Quadrature and Tuning Voltage Amplifiers	56
2.3.5	On-board Vacuum Chamber and Chassis	58
2.3.6	Analog Front-end Interfaces	60

2.3.7	Analog Front-end Implementation	61
2.4	Closed Loop Analog Back End	61
2.4.1	System Design	61
2.4.2	Drive Loop Design	63
2.4.3	Automatic Level Control Design	68
2.4.4	Sense Channel Design	74
2.4.5	Digital ALC, Quadrature and Frequency Tuning System	81
2.4.6	Analog Back-end Implementation and Summary	82
Chapter 3	Gyroscope Performance Characterization	83
3.1	Drive Loop Characterization	85
3.2	Scale Factor Characterization	90
3.2.1	AM readout scale factor	90
3.2.2	AM/FM hybrid Readout with expanded dynamic range	91
3.3	Noise Characterization	93
Chapter 4	Conclusion and Future Work	95
4.1	Conclusion	95
4.2	Contributions and lessons	96
4.2.1	Rate Mode Readout and Control Interface	96
4.2.2	Non-linearity	96
4.2.3	Feed-through Cancellation	97
4.2.4	On-board Vacuum Chamber	97
4.3	Future Work Summary	97
4.4	Next stage goals	98
4.5	New interface Architecture	98
4.6	Quadrature and Frequency Tuning Control	98
4.6.1	Automatic mode matching	98
4.6.2	Closed Loop Quadrature Control	99

4.7 Improved Instrumentation	99
4.8 Improved Device and System Modelling	100
4.9 Mixed Signal ASIC	100
4.10 Resonator Design Feedback	101
Appendix A : Analog Front-end Schematic	102
Appendix B : Analog Front-end Layout	105
Appendix C : Analog Front End Errata	111
Appendix D : On-board Vacuum Chamber Mechanical Drawings	112
Appendix E : Closed Loop Interface (GTBE-A) Schematic	118
Appendix F : Closed Loop Interface (GTBE-A) Layout	123
Appendix G : Closed Loop Interface (GTBE-A) Revised Schematic	126
Appendix H : gyroChar MATLAB Toolbox	131
Appendix I : Digital Control Firmware	132
References	133

# LIST OF TABLES

TABLE 1: GYROSCOPE PERFORMANCE CATEGORIES [14] .....	4
TABLE 2: BIAS STABILITY PERFORMANCE OF MACRO-SCALE GYROSCOPES [23, 26] .....	6
TABLE 3: $\mu$ HSR PROPERTIES.....	11
TABLE 4: MECHANICAL TO ELECTRICAL MODELLING ANALOGY EQUALIVANT COMPONENTS.....	43
TABLE 5: OPA2140/OPA140 SPECIFICATIONS .....	49
TABLE 6: ADA4898 KEY SPECIFICATIONS.....	64
TABLE 7: COMPARISON OF CALCULATED AND MEASURED PARAMETERS .....	83

# LIST OF FIGURES

FIGURE 1: CROSS-SECTIONAL VIEW OF A MICRO-HEMISPHERICAL SHELL RESONATOR ( $\mu$ HSR).....	2
FIGURE 2: ALLEN VARIANCE OF MACRO-SCALE HIGH PERFORMANCE GYROSCOPES. ASTRIX 120 AND ASTRIX 200 ARE TWO DIFFERENT MODELS OF FOG. [26].....	6
FIGURE 3: ILLUSTRATION OF THE CORIOLIS FORCE THE TOP SHOWS A VIEW FROM AN INERTIAL REFERENCE FRAME AND THE BOTTOM SHOWS A VIEW IN THE NON-INERTIAL ROTATING REFERENCE FRAME (A) POSITIONS BEFORE MOVEMENT OF THE BALL AND CC TABLE ROTATION (B) POSITION AFTER THE BALL MOVEMENT AND CC TABLE ROTATION [27].....	7
FIGURE 4: GYROSCOPE OPERATION OF THE DRIVE MODE, X, AND SENSE MODE, Y, IN (A) MODE-SPLIT GYRO OPERATION (B) MODE-MATCHED GYRO OPERATION .....	8
FIGURE 5: COMMON TYPE I GYROSCOPE STRUCTURES [9].....	9
FIGURE 6: (A) BIRD-BATH RESONATOR DEVELOPED AT THE UNIVERSITY OF MICHIGAN [44] , (B) GLASS- BLOWN HEMISPHERICAL RESONATOR DEVELOPED AT THE UNIVERSITY OF CALIFORNIA [46] , AND (C) BALL-BEARING MOLD HEMISPHERICAL SHELL RESONATOR FROM THE UNIVERSITY OF UTAH [6] .	9
FIGURE 7: $\mu$ HSR STRUCTURE WITH AN (A) EXPLODED AND (B) CROSS-SECTIONAL SCHEMATIC VIEW .....	10
FIGURE 8: (A) BIRD'S EYE VIEW OF THE $\mu$ HSR. (B) CLOSE-UP OF INTEGRATED ELECTRODES FOR CAPACITIVE ACTUATION, CONTROL, AND READOUT OF THE $\mu$ HRG.....	11
FIGURE 9: EXAMPLE ALLAN VARIANCE PLOT HIGHLIGHTING THE GYROSCOPE NOISE PERFORMANCE METRICS [55] .....	14
FIGURE 10: ANALOG FRONT-END DESIGNS [63] .....	20
FIGURE 11: AUTOMATIC LEVEL CONTROL SYSTEM .....	24
FIGURE 12: FREQUENCY RESPONSE OF THE INTERFACED $\mu$ HSR .....	29
FIGURE 13: FREQUENCY SPLIT BETWEEN THE M=2 MODES .....	30
FIGURE 14: TWO M=2 MODES AS THE FREQUENCY SPLIT BETWEEN THE MODES IS REDUCED FROM 27HZ TO 5 HZ. ....	31
FIGURE 15: MODE-MATCHED M=2 PEAK .....	31
FIGURE 16: RINGDOWN MEASUREMENT CONFIGURATION .....	32
FIGURE 17: RING DOWN TIME MEASUREMENTS.....	33
FIGURE 18: RING DOWN TIME MEASUREMENT OF A POLYSILICON DEVICE WITH A Q OF 30K.....	34

FIGURE 19: DEVICE DRIVE DISPLACEMENT AMPLITUDE WITH A DC BIAS OF 40V, 20 $\mu$ M GAP SIZE AND AN AC DRIVE VOLTAGE OF 30 MV .....	35
FIGURE 20: FREQUENCY RESPONSE AS VAC IS SWEPT FROM 4.75MV TO 115MV SHOWING THE ONSET OF NON-LINEARITY AS VAC INCREASES.....	35
FIGURE 21: FEEDTHROUGH MODEL.....	36
FIGURE 22: TOP-SIDE SUBSTRATE BOND EFFECT ON FEED-THROUGH .....	37
FIGURE 23: FIRST ORDER HARMONIC OSCILLATOR SYSTEM.....	37
FIGURE 24: DRIVE MODE MODEL.....	38
FIGURE 25: DEVICE ELECTROSTATIC INTERFACE .....	39
FIGURE 26: $\mu$ HSR WITH ALL 16 ELECTRODES WIRE-BONDED TO THE AFE.....	40
FIGURE 27: MECHANICAL TO ELECTRICAL MODELLING ANALOGY .....	43
FIGURE 28: MEASURED RESONATOR FREQUENCY RESPONSE.....	44
FIGURE 29: DEVICE MODEL OF BOTH THE DRIVE AND SENSE MODES.....	45
FIGURE 30: ANALOG FRONT-END SUBSYSTEM CONFIGURATION.....	48
FIGURE 31: PICKOFF CHANNEL DESIGN.....	48
FIGURE 32: PICKOFF CHANNEL FREQUENCY RESPONSE (GAIN IN DB $\Omega$ ).....	50
FIGURE 33: FORCER CHANNEL BUFFER DESIGN .....	53
FIGURE 34: FORCER CHANNEL FREQUENCY RESPONSE SIMULATION .....	53
FIGURE 35: SIMULATION OF (A) FREQUENCY RESPONSE WITH THE FEED-THROUGH CANCELLATION MISMATCHED BY 10% (B) FREQUENCY RESPONSE WITH FEEDTHROUGH CANCELLATION PERFECTLY MATCHED.....	54
FIGURE 36: FEED-THROUGH CANCELLATION DESIGN .....	55
FIGURE 37: QUADRATURE AMPLIFIERS (A) NON-INVERTING CONFIGURATION (B) INVERTING CONFIGURATION .....	57
FIGURE 38: THE EFFECT OF VACUUM CHAMBER PRESSURE ON QUALITY FACTOR .....	58
FIGURE 39: ANALOG FRONT-END COPPER RING TO ACCOMMODATE AN ON-BOARD VACUUM CHAMBER .....	59
FIGURE 40: ON-BOARD VACUUM CHAMBER CONFIGURATION.....	60
FIGURE 41: ANALOG FRONT END INTERFACE PIN-OUT.....	60
FIGURE 42: AFE IMPLEMENTATION WITH ATTACHED ADAPTER BOARD FOR EARLY $\mu$ HSR TESTING .....	61

FIGURE 43: ANALOG RATE INTERFACE BLOCK DIAGRAM .....	62
FIGURE 44: SECOND DRIVE POST-AMP WITH OPTIONAL PHASE SHIFTER .....	63
FIGURE 45: VCA810 TYPICAL GAIN ERROR PLOT .....	64
FIGURE 46: SIMULATED POST-AMP FREQUENCY RESPONSE .....	65
FIGURE 47: DRIVE LOOP FEED-THROUGH FILTER DESIGN.....	66
FIGURE 48: GAIN AND PHASE OF FEED-THROUGH LPF SIMULATION .....	66
FIGURE 49: EXPECTED DRIVE LOOP GAIN AND PHASE AT $F_{RES} = 6.7\text{KHZ}$ .....	67
FIGURE 50: OPEN-LOOP FREQUENCY RESPONSE .....	68
FIGURE 51: AUTOMATIC LEVEL CONTROL (ALC) DESIGN .....	69
FIGURE 52: POSSIBLE CONFIGURATIONS OF THE FLEXIBLE PEAK DETECTOR DESIGN. (A) BASIC PEAK DETECTOR USED IN THIS DESIGN, (B) AND (C) REDUCE THE LEAKAGE FROM THE VPEAK NODE WHICH IS USEFUL FOR LONG TIME CONSTANTS .....	70
FIGURE 53: PEAK DETECTOR TRANSIENT SIMULATION SHOWING THE INPUT WAVEFORM IN PURPLE, THE HOLDING CAPACITOR VOLTAGE WITH RIPPLE IN BLUE AND THE SMOOTHED OUTPUT AFTER THE LPF.....	71
FIGURE 54: ALC LEVEL SHIFTER .....	72
FIGURE 55: AUTOMATIC LEVEL CONTROL AND DRIVE LOOP OSCILLATOR SIMULATION TEST BENCH.....	73
FIGURE 56: TRANSIENT SIMULATION TO VERIFY THE DESIGN OF THE DRIVE LOOP OSCILLATOR. THE LIGHT BLUE SIGNAL IS THE DRIVE FORCER SIGNAL .....	73
FIGURE 57: TRANSIENT SIMULATION SHOWING THE STEP RESPONSE OF THE ALC AS THE SET POINT, THE RED STEP SIGNAL, WAS STEPPED FROM THE NORMAL OPERATING POINT OF 124MV TO 200MV. THE BLUE SIGNAL IS THE REGULATED DRIVE VOLTAGE, VREG. THE GREEN SIGNAL IS THE ALC ERROR VOLTAGE.....	74
FIGURE 58: SENSE CHANNEL DESIGN .....	75
FIGURE 59: FREQUENCY RESPONSE OF THE SENSE CHANNEL DRIVE AMPLIFIER .....	77
FIGURE 60: FREQUENCY RESPONSE OF THE SENSE PICKOFF AMPLIFIER WITH PHASE COMPENSATION .....	78
FIGURE 61: AD835 ANALOG MULTIPLIER CONFIGURATION .....	78
FIGURE 62: SENSE CHANNEL 2ND ORDER LPF.....	79
FIGURE 63: FREQUENCY RESPONSE OF THE SENSE CHANNEL LOW PASS FILTER .....	80
FIGURE 64: SENSE CHANNEL TRANSIENT SIMULATION .....	81

FIGURE 65: ANALOG BACK-END PCB .....	82
FIGURE 66: GYROSCOPE CHARACTERIZATION SETUP .....	84
FIGURE 67: ASSEMBLED GYROSCOPE CHARACTERIZATION PLATFORM SHOWING (A) AND (B) THE AFE MOUNTED IN THE CHASSIS WITH THE SIGNAL BREAKOUT BOARD ATTACHED (C) THE PLATFORM MOUNTED ON THE RATE TABLE, AND (D) THE ANALOG BACK-END BOARD (RIGHT) AND DRIVE LOOP FEED-THROUGH FILTER (LEFT) .....	85
FIGURE 68: SPECTRUM OF DRIVE LOOP $V_{REG}$ .....	86
FIGURE 69: FREQUENCY RESPONSE OF THE AFE INCLUDING THE $\mu$ HSR.....	87
FIGURE 70: REGULATED DRIVE VOLTAGE WITH THE DUT UNDER ROTATION ( $V_{REG}$ ) (1 SEC/DIV, 100MV/DIV) .....	87
FIGURE 71: FM RATE RESPONSE SCALE FACTOR .....	89
FIGURE 72: FM TRANSIENT RATE RESPONSE TO A 100.531 °/S ROTATION RATE.....	89
FIGURE 73: RATE RESPONSE FOR A RATE INPUT OF 25 °/SEC .....	90
FIGURE 74: RATE RESPONSE SHOWING A SCALE FACTOR OF 8.57 MV/°/S .....	91
FIGURE 75: HYBRID AM/FM $\mu$ HRG BLOCK DIAGRAM.....	92
FIGURE 76: AM (BLUE) AND FM (RED) ROTATION RATE RESPONSES SHOWING SCALE FACTORS OF 8.57 MV/O/S AND 1.46 MHZ/O/S, RESPECTIVELY .....	92
FIGURE 77: TCF AND QUALITY FACTOR TEMPERATURE DEPENDENCE .....	93
FIGURE 78: ALLAN VARIANCE (DEVIATION) .....	94

# LIST OF EQUATIONS

EQUATION 1: CORIOLIS FORCE.....	8
EQUATION 2: RESOLUTION ( $TNE\Omega$ ).....	13
EQUATION 3: MECHANICAL NOISE [53] .....	13
EQUATION 4: ALLEN VARIANCE RELATIONSHIP TO THE NOISE PSD [55] .....	14
EQUATION 5: TOTAL ALLAN VARIANCE.....	15
EQUATION 6: ARW ALLAN VARIANCE CONTRIBUTION .....	15
EQUATION 7: ANGLE RANDOM WALK (ARW) AND $TNE\Omega$ .....	15
EQUATION 8: RATE RANDOM WALK ALLAN VARIANCE CONTRIBUTION .....	15
EQUATION 9: GYROSCOPE BANDWIDTH.....	16
EQUATION 10: WHOLE ANGLE MODE ANGULAR READOUT .....	19
EQUATION 11: TOTAL NOISE OF THE TIA PICK-OFF FRONT-END .....	21
EQUATION 12: ELECTRICAL NOISE EQUIVALENT ACCELERATION ( $ENE\Omega$ ) OF THE TIA PICK-OFF FRONT-END .....	21
EQUATION 13: FUNDAMENTAL FREQUENCY SPLIT SCALING LAW [47] .....	22
EQUATION 14: DERIVATION OF THE ELECTROSTATIC SPRING SOFTENING CONSTANT IN A PARALLEL PLATE TRANSDUCER .....	23
EQUATION 15: SPRING CONSTANT MATRIX WITH ELECTROSTATIC QUADRATURE AND FREQUENCY COMPENSATION .....	23
EQUATION 16: DERIVATION OF THE ALC DYNAMICS, EQUILIBRIUM POINT, AND STABILITY CRITERIA [65, 66].....	27
EQUATION 17: RING DOWN TIME RELATIONSHIP WITH QUALITY FACTOR.....	32
EQUATION 18: DRIVE MODE MAGNITUDE AND PHASE .....	38
EQUATION 19: DERIVATION OF THE DRIVE FORCER ELECTRODES' TRANSFER FUNCTION .....	41
EQUATION 20: DERIVATION OF THE DRIVE MODAL DYNAMICS.....	42
EQUATION 21: DERIVATION OF THE DRIVE FORCER DISPLACEMENT TO DRIVE PICKOFF DISPLACEMENT ..	42
EQUATION 22: DERIVATION OF THE DRIVE PICKOFF ELECTRODES' TRANSFER FUNCTION .....	43
EQUATION 23: ELECTRICAL DOMAIN EQUIVALENT MODEL OF THE $\mu$ HSR .....	44
EQUATION 24: RESONATOR DRIVE MODE EQUIVALENT RLC MODEL PARAMETERS.....	45
EQUATION 25: DERIVATION OF THE SENSE MODAL DYNAMICS.....	46

EQUATION 26: SENSE MODE DISPLACEMENT TO MOTIONAL CURRENT TRANSFER FUNCTION .....	47
EQUATION 27: PHASE RELATIONSHIP BETWEEN DRIVE VOLTAGE AND SENSE CURRENT .....	47
EQUATION 28: PICKOFF CHANNEL GAIN AND PHASE AT $\Omega_{RES}$ .....	50
EQUATION 29: AFE PICKOFF CHANNEL NOISE CALCULATION SHOWING A PREDICTED $ENE\Omega = 1.27^\circ/HR$ AND ARW OF $27.34 * 10^{-3}^\circ/hr$ .....	51
EQUATION 30: MNE $\Omega$ CALCULATION SHOWING MNE $\Omega = 13.14^\circ/HR$ .....	52
EQUATION 31: RESOLUTION CALCULATION SHOWING TNE $\Omega = 13.2^\circ/HR$ .....	52
EQUATION 32: FEED-THROUGH CANCELLATION CIRCUIT OPERATING PRINCIPLE .....	55
EQUATION 33: SIMULATED POST-AMP GAIN AND PHASE AT THE RESONANT FREQUENCY OF 6.7KHZ.....	65
EQUATION 34: BARKHAUSEN CRITERIA FOR OSCILLATION.....	67
EQUATION 35: PI CONTROLLER GAINS.....	71
EQUATION 36: ALC STABILITY CRITERIA .....	72
EQUATION 37: SCALED SENSITIVITY ESTIMATE.....	76
EQUATION 38: SENSE CHANNEL GAIN .....	76
EQUATION 39: SCALE FACTOR ESTIMATE .....	76
EQUATION 40: PHASE SHIFTER TRANSFER FUNCTION .....	77
EQUATION 41: DEMODULATOR TRANSFER FUNCTION .....	79

# LIST OF ABBREVIATIONS

3D-HARPSS	three-dimensional high aspect ratio poly- and single-crystalline silicon
AC	alternating current
ADI	analog devices incorporated
AFE	analog front-end
AGC	automatic gain control
ALC	automatic level control (synonymous with AGC)
AM	amplitude modulated
ASIC	application specific integrated circuit
ARW	angle random walk
BW	bandwidth
C+SWaP	cost, size, weight, and power consumption
CC	counterclockwise
CMG	control moment gyroscope
CVG	Coriolis vibratory gyroscope
DC	direct current
DOF	degree of freedom
DTG	dynamically tuned gyroscope

DSP	digital signal processing
DUT	device under test
FEA	finite element analysis
FEM	finite element method
FFT	fast Fourier transform
FOG	fiber optic gyroscopes
FM	frequency modulation
GPS	global positioning system
HCI	human-computer interaction
HRG	hemispherical resonating gyroscope
IMUs	inertial measurement units
LPF	low-pass filter
M <sup>2</sup> -TFG	mode-matched tuning fork gyroscope
MEMS	micro-electro-mechanical systems
MRIG	micro-scale rate integrating gyroscope
μHRG	micro-hemispherical resonating gyroscope
μHSR	micro-hemispherical shell resonator
NMR	nuclear magnetic resonance
PCB	printed circuit board
PI	proportional-integral controller

PID	proportional-integral-differential controller
PM	phase modulation
PSD	power spectral density
QFM	quadrature frequency modulation
RIG	rate-integrating gyroscope
RLC model	resistor (R)-inductor (L)-capacitor (C) model
RLG	ring laser gyroscopes
SWaP+C	size, weight, power consumption, or cost
TED	thermal elastic dampening
TIA	transimpedance amplifier
TFG	tuning fork gyroscopes
TRA	trans-resistance amplifier
ZRO	zero rate output

# LIST OF SYMBOLS

$2\pi/\omega_0$		the resonance frequency period
$C_0$	rest capacitance between the shell and each electrode	
$D$		damping matrix
$ENE\Omega$		electrical noise equivalent rotation
$F_d$		electrostatic force
$g, g_0$		resting gap size
$h_0$		average thickness
$h_4$	coefficient of the fourth harmonic of the fourier series representation of the thickness around the z-axis	
$I_{mot-d}$		motional current
$\overline{i_{op-amp}}$		op-amp input current noise density
$\overline{I_{N-tot}}$		total input current noise density
$k_{elec}$		extra spring constant
$k_I$		integral gain
$k_P$		proportional gain
$M$		effective mass of the mode
$M_{eff}$		effective mass of the mode
$\lambda$	angular cut-off frequency of the ALC peak detector filter	
$M_0$		average mass per unit angle

$M_4$	the fourth harmonic of the mass distribution
$MNE\Omega$	mechanical noise equivalent rotation
$Q$	quality factor
$Q_{\text{eff}}$	effective quality factor
$Q_{\text{TED}}$	thermo-elastic dampening quality factor limit
$S_{\Omega}(f)$	two-sided PSD of the rate output
$\theta$	angle of the vibration pattern with respect to the x mode
$\sigma_{ARW}^2(\tau)$	angular random walk Allan variance contribution
$\sigma_{Bias}^2(\tau)$	bias instability Allan variance contribution
$\sigma_{RRW}^2(\tau)$	rate random walk Allan variance contribution
$\tau_{\text{LPF}}$	LPF time constant
$TNE\Omega$	total noise equivalent rotation
$V_{\text{ac}}$	AC drive voltage
$V_c$	gain control voltage
$\overline{v_{\text{opamp}}}$	op-amp input voltage noise density
$V_{\text{ac}}$	AC component of the drive voltage
$V_P$	polarization voltage
$V_{Pd}$	drive channel effective polarization voltage
$V_{Ps}$	sense channel effective polarization voltage
$V_Q$	electrostatic quadrature tuning voltage

$V_{Q1}$	+22.5° electrostatic quadrature tuning voltage
$V_{Q2}$	-22.5° electrostatic quadrature tuning voltage
$V_{reg}$	nodal voltage in the drive loop regulated by the AGC
$V_T$	electrostatic frequency tuning voltage
$V_{T1}$	drive mode electrostatic frequency tuning voltage
$V_{T2}$	sense mode electrostatic frequency tuning voltage
$X_d$	drive displacement magnitude
$x_{df}$	drive forcer displacement
$x_{dp}$	drive pickoff displacement
$\Delta f$	modal frequency split
$\epsilon_0$	vacuum permittivity
$\omega$	angular frequency
$\omega_0$	resonant frequency
$\omega_{res}$	angular resonant frequency

## SUMMARY

Gyroscopes are inertial sensors that measure the rate or angle of rotation. The emergence of MEMS gyroscopes has produced sensors that are smaller, lower cost, lighter weight, and consume less power than previous solutions. However, traditional macro-scale solutions are capable of reaching higher performance levels than current MEMS solutions, with lower noise and higher dynamic ranges. MEMS gyroscopes have already come to dominate the low- to mid-performance consumer, automotive, and industrial markets and become one of the fastest growing segments of the microsensor market. The development of a high performance MEMS gyroscope that retains the operational benefits of existing MEMS solutions would not only make MEMS competitive with macro-scale solutions in high-performance applications, but also open entirely new applications to inertial sensing.

One of the most promising technologies for reaching a high-performance MEMS gyroscope has been development of the micro-hemispherical shell resonator. ( $\mu$ HRSR) The  $\mu$ HRSR has shown the potential to become the sensing element of a high performance gyroscope. Theoretical calculations and simulations have shown that the  $\mu$ HRSR is capable of very high quality factors (Q) of over a million. It has a small stiffness that causes low frequency resonant modes. It also has an axisymmetric structure that is very isotropic and results in small frequency splits between the degenerate  $m=2$  modes and low quadrature levels that allow the modes to be matched electrostatically.

All these advantages enable a gyroscope capable of operating in whole angle or rate integrating mode, where the angle of rotation is measured directly, eliminating errors that accumulate in the integration of the rotation rate. This mode also increases the dynamic range which, unlike the AM rate mode, isn't limited by the narrow bandwidth of the high Q resonator. At the same time it keeps the operational advantages inherent to MEMS gyroscopes. It uses low-cost batch fabrication techniques that enable wafer-level

mass fabrication. It is also small and light weight with a diameter of only 1.2mm and utilizes capacitive transduction and readout which enables a low-power interface.

However, the development of a high quality resonator alone does not make a high performance gyroscope. The interface and control systems must be carefully designed to take full advantage of the resonator's capabilities and compensate for its non-idealities. The design and implementation of the electronic control and read-out interface is just as important as that of the resonator for defining the final performance of the gyroscope.

This thesis presents the electronic control and read-out interface that has been developed to turn the micro-hemispherical shell resonator ( $\mu$ HSR) into a fully functional micro-hemispherical resonating gyroscope ( $\mu$ HRG) capable of measuring the rotation rate. First, the characterization of the  $\mu$ HSR, which both enabled the design of the interface and led to new insights into the linearity and feed-through characteristics of the  $\mu$ HSR, is presented. Then a detailed analysis of the design of each subsystem, including calculations and simulations, is presented.

Next, the performance characterization of the gyroscope is presented. The characterization starts with a verification of the drive loop to ensure the drive oscillator is locked to the resonant frequency of the  $\mu$ HSR and the drive loop amplitude is regulated to a level that avoids non-linear duffing. Then the transient response and scale factor of the AM rate response were characterized, showing the expected linear response with a scale factor of 8.57 mV/ $^{\circ}$ /s. Then the noise performance of the rate response was characterized by measuring the Allan variance, which showed a bias instability of 330  $^{\circ}$ /hr, and an angle random walk (ARW) of  $34^{\circ}/\sqrt{hr}$ . It is believed that the performance of the current device is limited by the interconnect parasitics and test set up non-idealities. The overall accuracy of the  $\mu$ HRG can be improved to sub  $^{\circ}$ /hr by optimizing the  $\mu$ HSR design, interface circuits, and test setup.

The characterization of the  $\mu$ HSR and the rate interface developed are major milestones in the development of the  $\mu$ HRG into a high performance gyroscope. It also

provides a good platform for the development of a high performance micro-hemispherical rate integrating gyroscope. ( $\mu$ HRIG)

# Chapter 1

## Introduction to MEMS Gyroscopes and the micro-Hemispherical Shell Gyroscope

While inertial sensing at the micro-scale has made great progress in many applications by reducing the cost and size of the sensing element, the noise performance, dynamic range, and accuracy levels required for some high performance applications has remained elusive. [1] However, many new device and interface designs have been developed that have the potential to solve this eminent problem. One of these new devices is the micro-hemispherical shell resonator. ( $\mu$ HSR)[2-6] The characterization and electronic interface and control systems that have developed the  $\mu$ HSR into a micro-hemispherical resonating gyroscope ( $\mu$ HRG) [7, 8] will be presented.

The  $\mu$ HRG is a chip scale type I [9] Coriolis vibratory gyroscope (CVG) with a  $\mu$ HSR that is 1.2mm in diameter, 1 $\mu$ m in thickness and operates at low frequencies from 6kHz to 7kHz. The  $\mu$ HSR is batch fabricated using a three-dimensional high aspect ratio poly- and single crystalline silicon (3D-HARPSS) process. It was inspired by the macro-scale HRG, a robust inertial grade gyroscope with a diameter of 35mm [10] which has been used extensively for demanding inertial navigation applications. [10, 11] The original device design achieves a quality factor of over 11,000 with improved designs showing a quality factor up to 40,000.

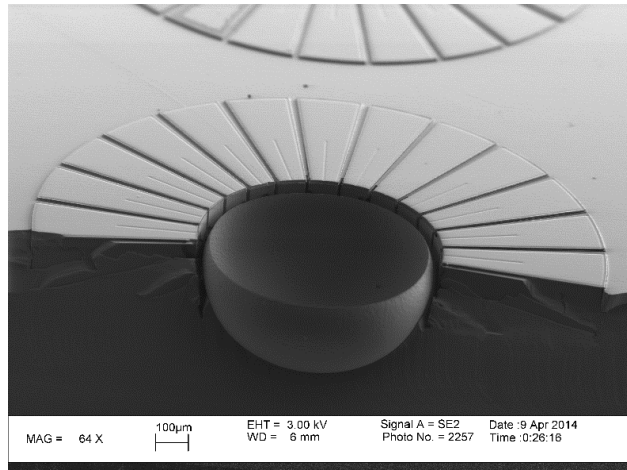


**Figure 1: Cross-sectional View of a micro-hemispherical shell resonator ( $\mu$ HSR)**

The rate interface of the  $\mu$ HRG consists of a closed loop drive channel to actuate the device and a synchronous read-out sense channel that reads the rotation rate of the device from the amplitude modulated (AM) sense mode output current. An electrostatic tuning system provides the DC biasing that enables electrostatic actuation and capacitive readout. It also provides the tuning voltages for aligning and tuning the frequency of the modes. Feed-through cancellation and filtering compensate for the capacitive feed-through of the device. The interface also incorporates an on-board vacuum chamber that allows the device to operate in sub-mTorr vacuum pressure.

The  $\mu$ HRG is operated under mode-matched conditions with polarization ( $V_P$ ), tuning ( $V_T$ ), and quadrature balancing ( $V_Q$ ) voltages that are 14 volts or less. These relatively low tuning voltages are enabled by the low stiffness of the  $\mu$ HSR and are suitable for generation on-chip in some processes. Higher polarization voltages can cause the drive mode to become non-linear and duff for the same drive amplitude.

The gyroscope rate response has been characterized. It has a scale factor of  $8.57\text{mV}/^\circ/\text{s}$ , measured over the range of  $\pm 40^\circ/\text{s}$ . The Allan Variance of the gyroscope was measured and showed a bias instability of  $330^\circ/\text{hr}$  and angle random walk (ARW) of  $34^\circ/\sqrt{\text{hr}}$ .

This rate interface is the first step toward turning the  $\mu$ HSR from a resonator into a micro-hemispherical rate integrating gyroscope. ( $\mu$ HRIG) Further development of the electronic interface would allow whole angle operation and improve the dynamic range and bandwidth of the gyroscope while eliminating rate integration errors. The development of automatic open and closed loop mode matching, the amplitude control loop, and a revised sense channel will be required for rate integrating operation.

### ***1.1 Applications of Gyroscopes***

Micro-scale gyroscopes are used in a wide variety of consumer and industrial markets. The consumer market includes image stabilization, automotive ride stabilization and rollover detection, navigation[12], amateur drone guidance, context awareness, location based services, human-computer interaction (HCI) devices and a variety of applications in motion sensing such as gaming and gesture recognition. [13] The industrial and military markets include applications in precision robotics, platform stabilization, projectile guidance, remote monitoring, down-hole electronics in the petroleum industry, precision agriculture[14], dead-reckoning, GPS augmentation, and other high performance applications. Many of these applications have become commercially successful, with many commercial products available, but also many open market opportunities.

These opportunities will only grow as the performance of microgyroscopes improves. Gyroscopes can be categorized according to performance into three application groups as shown in Table 1. [15] Many opportunities exist in the tactical and inertial grade performance levels, including the replacement of existing macro-scale gyroscopes in traditional navigation markets in the aerospace and defense industries and the creation of entirely new markets that were previously limited by size, weight, power consumption, or cost (SWaP+C) of traditional solutions. Many applications that were previously limited to military and industrial markets due to size and cost have the

potential to be opened up to the consumer market. This has already started as new multi-DOF IMUs enter the consumer market as can be seen in new consumer products such as the iPhone 6 which incorporates an Invensense MP67B 6-axis gyroscope and accelerometer Combo. [16]

**Table 1: Gyroscope Performance Categories [14]**

Parameter	Rate Grade	Tactical Grade	Inertial Grade
Angle Random Walk (o/vhz)	> 0.5	0.5 - 0.05	< 0.001
Bias Drift o/hr	10 - 1000	0.1 - 10	<0.01
Scale Factor Accuracy (%)	0.1 - 1	0.01 - 0.1	<0.001
Full Scale Range (o/sec)	50 - 1000	> 500	>400
Mac. Shock in 1ms (g's)	0.1 - 1	$10^3 - 10^4$	$10^3$
Bandwidth (Hz)	> 70	$\approx 100$	$\approx 100$

Today the performance of multi-degree of freedom (multi-DOF) inertial measurement units (IMUs) is limited by the performance of the Gyroscope. However as the performance of gyroscopes has improved, the development of MEMS multi-DOF IMUs has been advanced by companies such as Analog Devices, Invensense, STMicroelectronics, and others. However there is potential for substantial growth as the performance of micro-gyroscopes continues to improve. [17] Some more recent products not-only integrate multi-DOF sensing elements but also the sensor fusion processing or microcontroller into a system-in-package IMU solution. Further integration of not only the sensing elements but also the compensation, sensor fusion, and strap down navigation algorithms will continue to improve performance and overall SWaP+C of MEMS sensor based inertial systems.

## ***1.2 Micro-hemispherical Shell Resonator Background***

### **1.2.1 Gyroscope History**

The very first Coriolis vibratory gyroscopes were not made by man, but were rather natural adaptations developed by insects for navigation and flight stabilization. [18] These vibratory gyroscopes consist of a pair of appendages known as halteres. They are driven by flapping them similar to a wing. The Coriolis force can then be directly measured by the neural system [19, 20] and the rotational information can be processed for flight control.

Early man-made gyroscopes consisted of gyroscopes with moving parts and used the Coriolis force, such as Foucault's pendulum, or large inertial masses in what are now known as mechanical gyroscopes. Mechanical gyroscopes are based on the inertia of a spinning rotor. They initially gained popularity as gyrocompasses in the early 1800s. [21] They regained popularity in the aerospace industry of the 1960's. The Dynamically Tuned Gyroscope (DTG), for example, was used as part of the IMU used on the space shuttle and the Control Moment Gyroscope (CMG) has been used for platform stabilization on satellites. [22] However reliability issues with the bearings required to sustain their motion, along with the poor SWaP+C of the mechanical gyroscope lead to their obsolescence.

Modern high performance macro-scale gyroscopes include ring laser gyroscopes (RLG), fiber optic gyroscopes (FOG), nuclear magnetic resonance (NMR) [23] gyroscopes and macro-scale Coriolis vibratory gyroscopes (CVG) [24] such as the hemispherical resonating gyroscope. (HRG) The RLG and FOG both utilize the Sagnac effect [25] on electromagnetic waves and CVGs utilize the Coriolis effect on stress waves to measure rotation. The drift and stability performance of these solutions continues to outperform MEMS gyroscopes with bias stability and ARW values as shown in Table 2

and Allan variance shown in Figure 2. However these solutions have been eclipsed in terms of SWaP+C by MEMS technologies.

**Table 2: Bias Stability Performance of Macro-scale Gyroscopes [23, 26]**

Bias Stability Performance of Macro-scale Gyroscopes				
	RLG	FOG	NMR	HRG
Min. Bias Stability ( $^{\circ}$ /hr)	0.002	-	0.01	0.0015
ARW ( $^{\circ}$ /√hz)	0.004	0.0002	0.001	-

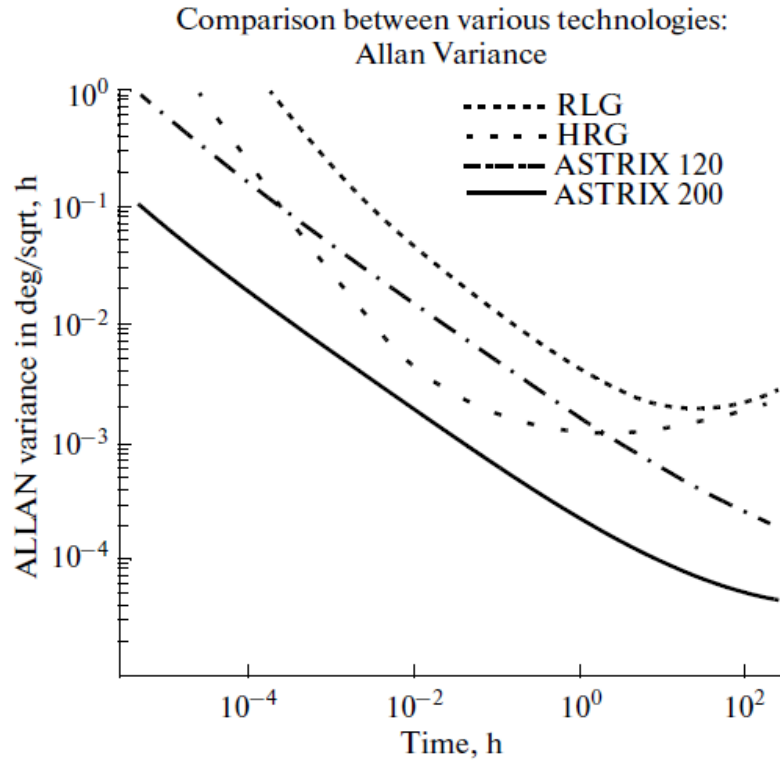


**Figure 2: Allen Variance of macro-scale high performance gyroscopes. Astrix 120 and Astrix 200 are two different models of FOG. [26]**

## 1.2.2 Coriolis Vibratory Gyroscope Operating Principles

The Coriolis force is a non-inertial force that is generated in rotating frames. It is demonstrated in Figure 3. The top of each figure shows the dynamics as seen from an inertial reference frame and the bottom shows the dynamics as seen from the non-inertial rotating frame on the table. Notice the location of the dot fixed on the surface of the table. When the table rotates counterclockwise (CC) between Figure 3(a) and Figure 3 (b) you can see that in the non-inertial rotating frame the ball takes a curved trajectory. The force that causes this curvature is known as the Coriolis force.

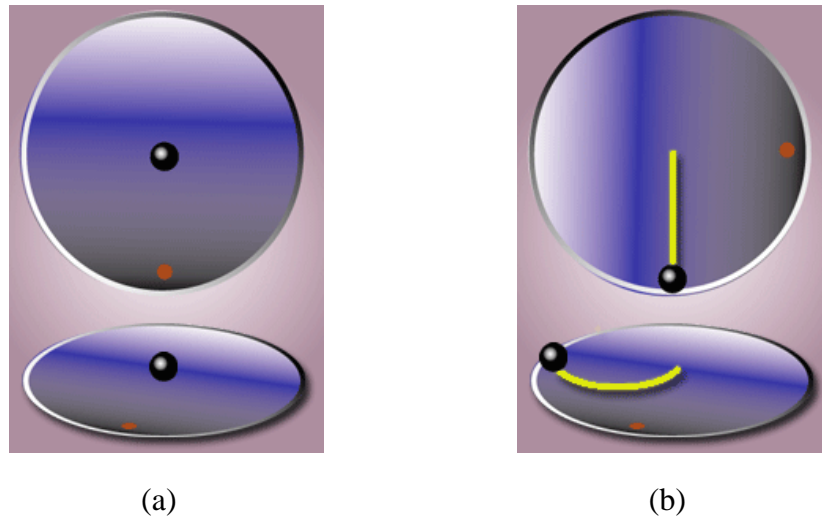


**Figure 3: Illustration of the Coriolis Force** The top shows a view from an inertial reference frame and the bottom shows a view in the non-inertial rotating reference frame (a) Positions before movement of the ball and CC table rotation (b) Position after the ball movement and CC table rotation [27]

A Coriolis vibratory gyroscope (CVG) operates by utilizing this “imaginary” force in the rotating frame to measure the rotation of the disk. First a force is applied to a mass to get it to vibrate at a constant velocity. If this mass is turned, then the Coriolis force, as shown in Equation 1, causes a force orthogonal to the velocity of the vibration and the axis of rotation (out of the page in Figure 3). This force then causes a vibratory

motion orthogonal to the first. This second vibratory motion can then be measured and related to the angular rotation rate or rotation whole angle.

$$F_C = -2M\Omega \times V$$

**Equation 1: Coriolis force**

### 1.2.3 Existing MEMS Technologies

The vast majority of modern MEMS gyroscopes in production are type II and most of these are tuning fork gyroscopes. (TFG) Type II gyroscopes measure the angular rate of rotation and have two distinct drive and sense modes. [9] They can be operated with the drive mode frequency much lower than the sense mode frequency (mode-split), providing large bandwidths and robust insensitivity to environmental effects [28] or they can be operated with the modal frequencies matched which substantially enhances (by a factor of the sense Q) the sensitivity and resolution of the device. [29] These two operating methods are illustrated in Figure 4. An example of split-mode and mode-matched gyroscopes are the Analog Devices (ADI) ADXRS [30] and The Georgia Tech M<sup>2</sup>-TFG gyroscopes [31], respectively.

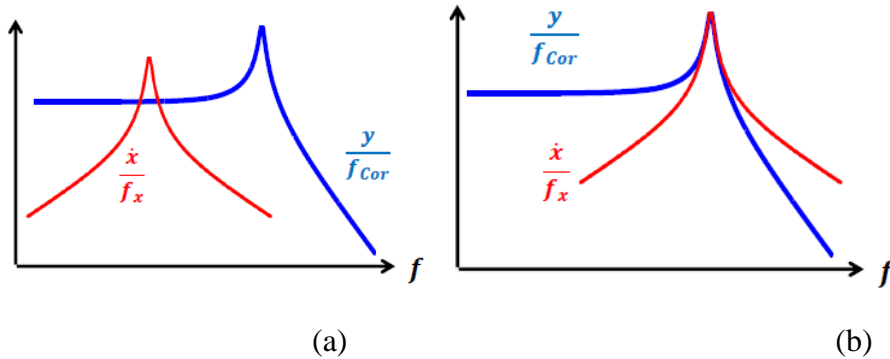


**Figure 4: gyroscope operation of the drive mode, x, and sense mode, y, in (a) Mode-split gyro operation (b) mode-matched gyro operation**

While type II gyroscopes measure angular rotation rate, type I gyroscopes are capable of measuring both the rate of rotation and the angle of rotation directly in what is known as rate-integrating or whole angle operation. This type of gyro has great potential

to increase the dynamic range and bandwidth of rotation sensing. Type I gyroscopes are most commonly axisymmetric in structure with some common structures shown in figure 5. Examples structures include rings [32], disks [33-37], cylinders [38-40], bird-baths [41-44], glass-blown wine-glass shells [45-47], and, of course,  $\mu$ HRG wine-glass shells. [2, 3, 7, 8, 48, 49] Resonator designs currently under research are illustrated in Figure 6. They are often operated in the  $m=2$  or  $m=3$  modes with two degenerate modes and 4 or 6 sets, respectively, of nodes and antinodes.

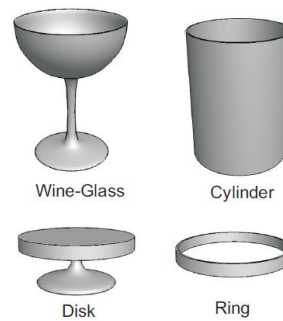
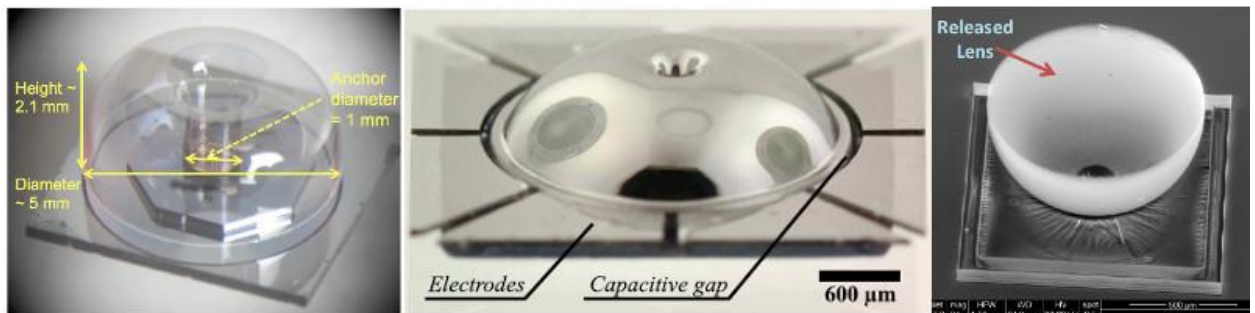


**Figure 5: Common Type I gyroscope structures [9]**

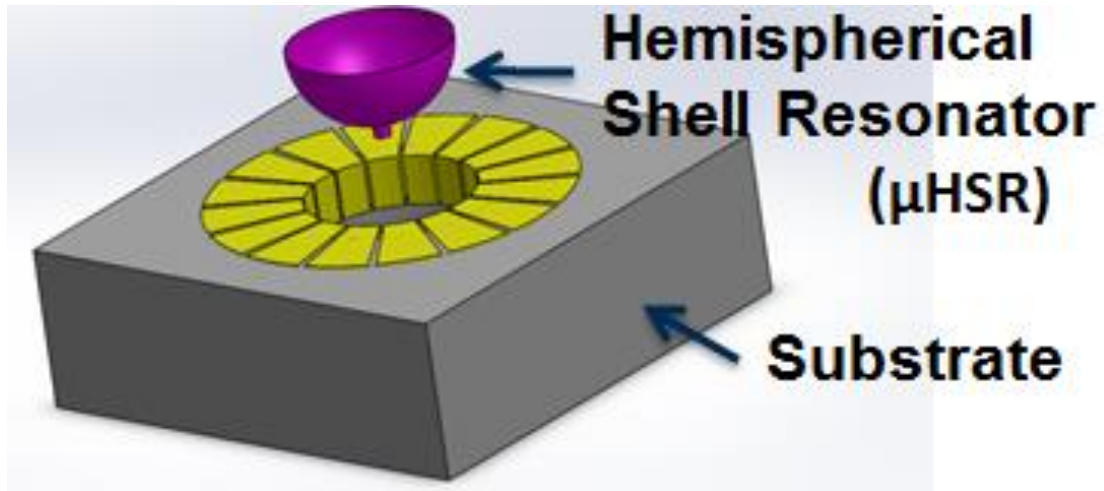


(a) (b) (c)  
**Figure 6: (a) Bird-bath resonator developed at the University of Michigan [44] , (b) glass-blown hemispherical resonator developed at the University of California [46] , and (c) ball-bearing mold hemispherical shell resonator from the university of Utah [6]**

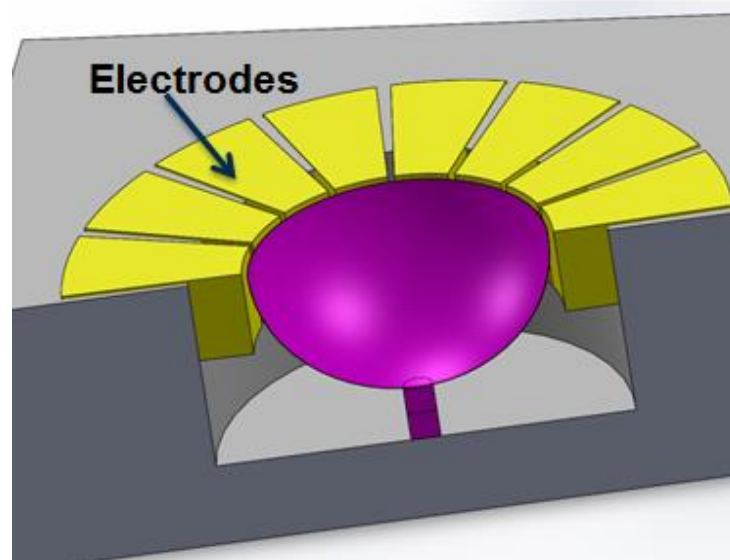
### 1.2.4 Micro-hemispherical Shell Resonator ( $\mu$ HSR)

The  $\mu$ HSR, shown in Figure 1, Figure 7 and Figure 8, is a three dimensional wine-glass shaped MEMS resonator. The resonator is made up of a poly-silicon shell surrounded by 16 tall electrodes integrated on the same silicon substrate but isolated by a

nitride layer as shown in Figure 8 (b). The device is fabricated using a low-cost batch fabrication 3D-HARPSS process in the Georgia Tech clean room. The device has a shell diameter of  $1200\ \mu\text{m}$ , a shell thickness of  $700\text{nm}$ , a resonance frequency of  $6.6\ \text{kHz}$ , and a mode-matched quality factor of  $11,000$ . [7, 50] A summary of the properties of the  $\mu\text{HSR}$  is given in Table 3.

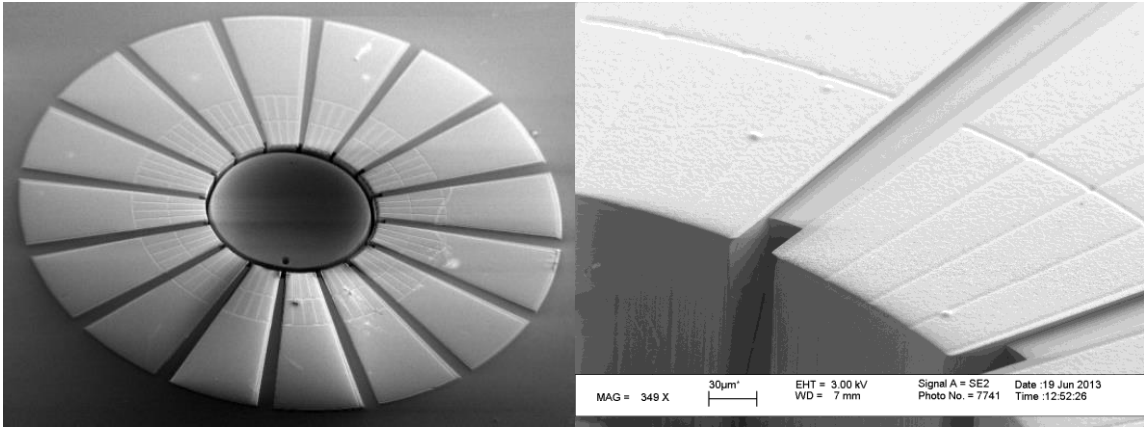


(a)



(b)

**Figure 7:  $\mu\text{HSR}$  structure with an (a) exploded and (b) cross-sectional schematic View**



(a)

(b)

**Figure 8: (a) Bird's eye view of the  $\mu$ HSR. (b) Close-up of integrated electrodes for capacitive actuation, control, and readout of the  $\mu$ HRG**

**Table 3:  $\mu$ HSR Properties**

$\mu$ HSR Properties	
Shell Material	Polysilicon
Shell Diameter	1240 $\mu$ m
Shell Thickness	0.7 $\mu$ m
Gap Size	20 $\mu$ m
Frequency (m=2)	6.7 kHz
Quality Factor	11,000
Frequency Split	105 Hz

The device structure presents a number of advantages over previous state of the art structures. The device has the potential to reach very high quality factors, low frequencies, and a small frequency splits between the two degenerate m=2 modes. The axial symmetric structure and low frequency of the device make it an excellent candidate for a rate-integrating gyroscope (RIG) capable of operating in whole-angle mode in order to measure the angle of rotation directly while increasing the dynamic range and bandwidth of the device when compared to the rate mode. Characterization of the device will be covered in section 2.1.

The resonator has the potential to reach very high quality factors. Thermal elastic dampening (TED) is caused by internal material friction creating heat gradients in the material. [51, 52] The low TED of poly-silicon enables a  $Q_{TED}$  of 10.3 million. [4] FEM simulations of  $Q_{TED}$  for the  $m=2$  mode, indicate a strong interaction between  $Q_{TED}$  and the presence of the support post when operating in the  $m=2$  mode, but little interaction for the  $m=3$  and  $m=4$  modes. [8] This indicates that for the  $m=2$  wineglass modes, support loss could be a major contributor to energy loss in the  $\mu$ HSR, but not  $Q_{TED}$ .

### ***1.3 $\mu$ HRG Gyroscope Performance Characterization***

#### **1.3.1 Scale Factor and Sensitivity**

The scale factor is the coefficient of the linear relation between the input rotation rate and output voltage. It is calculated by applying a least squares regression to the measured input rate to output voltage characteristics of the gyroscope. The magnitude and stability of the scale factor are both important performance metrics of a gyroscope

The sensitivity divides the scale factor into two separate components, the sensitivity of the resonator to rotation changes and the sensitivity of the analog front-end to capacitance changes. The sensitivity of the resonator is the ratio of the capacitance change of the sense electrodes to the input rotation rate. The sensitivity of the capacitive analog front end is the ratio of the output voltage to the capacitance change.

While the sensitivity is traditionally separated at the transducer, sometimes it is more convenient to include the transducer in the sensitivity of the resonator. The resonator current sensitivity is defined as the ratio of the output current to the input rotation rate and the analog front-end current sensitivity is the ratio of the output voltage to the motional current. This definition allows the current sensitivity of the analog front-end to be independent of the device characteristics. However it makes the device current sensitivity dependent on the biasing of the transducer which is set by the interface.

### 1.3.2 Resolution

The resolution of a gyroscope is the minimum detectable angular rate. The noise floor of the gyroscope sets the resolution and includes both mechanical and electrical noise components that are expressed in terms of their equivalent rotation rate, mechanical noise equivalent rotation ( $MNE\Omega$ ) and electrical noise equivalent rotation ( $ENE\Omega$ ). The Resolution is then equal to the total noise equivalent rotation ( $TNE\Omega$ ) and is given by Equation 2.

$$Resolution = TNE\Omega = \sqrt{MNE\Omega^2 + ENE\Omega^2}$$

**Equation 2: Resolution ( $TNE\Omega$ )**

The mechanical noise is caused by the Brownian noise of the resonator. It can be shown that by equating the displacement caused by Brownian motion to the displacement caused by the Coriolis force [32] the  $MNE\Omega$  can be calculated as shown in Equation 3.

$$MNE\Omega \propto \frac{1}{x_{drive}} \sqrt{\frac{4K_B T}{\omega M Q_{eff}}} \sqrt{BW}$$

**Equation 3: Mechanical Noise [53]**

The electrical noise comes from the interface electronics' sense pickoff channel. The pick-off analog front end of the sense channel has the most significant effect on the  $ENE\Omega$  since noise from later amplification stages of the sense channel are divided by the gain of the pick-off front-end. Hence the  $ENE\Omega$  can be calculated by dividing the current noise seen at the input by the resonator current sensitivity as shown in Equation 12.

### 1.3.3 Allan Variance

The Allan Variance [54] of a gyroscope is a way to characterize the gyroscope's random error processes over different averaging time scales. The Allan variance is specified as a plot of the variance at different averaging periods. The Allan variance is measured by sampling the rate output of the gyroscope with no rotation rate applied at a

high sampling frequency. The samples are then binned and each of the bins are averaged. This is done with a number of different binning periods to form the Allan variance plot. The Allan variance,  $\sigma^2(\tau)$ , is a time domain measure of the noise performance of a gyroscope. It is directly related to the more traditional frequency-domain two-sided PSD,  $S_{\Omega}(f)$ , by Equation 4. The Allan variance plot allows the origin of a noise term to be identified. Different noise terms dominate in different regions of the Allan variance plot.

$$\sigma^2(\tau) = 4 \int_0^{\infty} S_{\Omega}(f) \frac{\sin^4(\pi f \tau)}{(\pi f \tau)^2} df$$

**Equation 4: Allen Variance relationship to the noise PSD [55]**

These different regions of the averaging period in the Allan variance plot will have different slopes. The variance in each region is generated by a different type of random process in the gyroscope and is associated with a different metric of the gyroscope performance. These different regions and the associated slopes and noise performance metrics are shown in Figure 9. The total Allan variance is given by Equation 5.

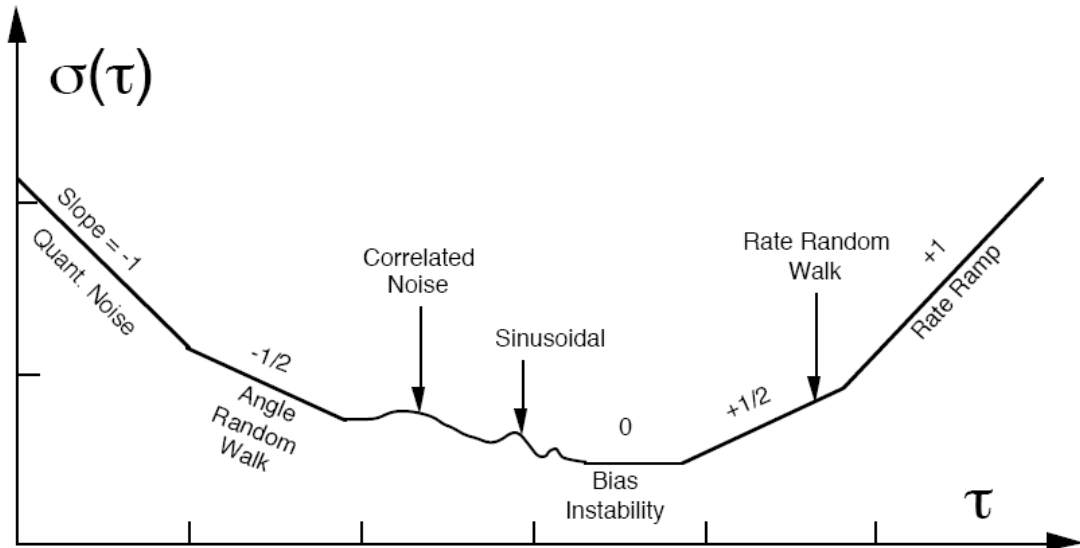


**Figure 9: Example Allan Variance plot highlighting the gyroscope noise performance metrics [55]**

$$\sigma_{Total}^2(\tau) = \sigma_{ARW}^2(\tau) + \sigma_{Bias}^2(\tau) + \sigma_{RRW}^2(\tau) + \dots$$

**Equation 5: Total Allan variance**

Angle random walk (ARW) has a slope of -1/2 in the Allan variance plot with an Allan variance contribution given by Equation 6. The ARW is caused by white noise in the gyroscope. It is a measure of the buildup of error in the angular rate. In particular it is a measure of the short term stability of the rate output that can be improved by filtering with longer time constants, but can have an important effect on the stability at startup. [56] The ARW can also be specified in terms of the TNEΩ with the relationship given by Equation 7, which can be derived using simple dimensional analysis.

$$\sigma_{ARW}^2(\tau) = \frac{N^2}{\tau}$$

**Equation 6: ARW Allan Variance Contribution**

$$ARW\left(\frac{^\circ}{\sqrt{hr}}\right) = \frac{1}{60} TNE\Omega\left(\frac{^\circ/hr}{\sqrt{hz}}\right)$$

**Equation 7: Angle Random Walk (ARW) and TNEΩ**

The bias instability is the random drift of the output bias or zero rate output. (ZRO) It represents the minimum bias drift possible with an ideal bias averaging period. The bias instability is used to characterize the drift of a gyroscope and is the value reported for bias drift in gyroscope data sheets. A contributing factor to this noise source is the 1/f noise in the pick-off analog front-end electronics and this shows in its 1/f PSD.

The rate random walk has an Allan variance that changes linearly with τ as given by Equation 8. The processes causing the rate random walk have very long time constants, and are related to environmental effects.

$$\sigma_{RRW}^2(\tau) = \frac{K^2}{3} \tau$$

**Equation 8: Rate random walk Allan variance contribution**

### 1.3.4 Bandwidth

The bandwidth of a mode-matched gyroscope, which determines its settling time, is limited by the bandwidth of the matched response. This bandwidth is given by Equation 9. Increasing the quality factor of the resonator and decreasing the resonant frequency reduces the bandwidth. Hence type I gyroscopes that require long ring-down times also have narrow bandwidths. However there are a number of methods to compensate the bandwidth of resonators with large quality factors. These include operating the sense channel in force-to-rebalance mode, intentionally loading the quality factor, operating the modes at a controlled frequency split, and operating in whole angle mode. Also, high precision applications that type I gyroscopes are focused on, such as inertial navigation, can tolerate low bandwidths since long term stability is more important than response time.

$$BW = \frac{f_0}{2Q}$$

**Equation 9: Gyroscope Bandwidth**

### 1.3.5 Dynamic Range

The dynamic range of a gyroscope is the range of rotation rates that can be measured. The dynamic range can be found by taking the difference between the largest linear rate response and the noise floor. The dynamic range is extended substantially in whole angle mode. Often WAGs are operated in rate mode until the rotation rate reaches the limits of the force feedback, after which it is operated in whole angle mode where the vibration pattern is allowed to freely rotate with a large dynamic range.

## ***1.4 Gyroscope Interface Methods Background***

A rotation rate interface was developed to make the micro-hemispherical shell resonator ( $\mu$ HRSR) into a micro-hemispherical resonating gyroscope ( $\mu$ HRG). An overview of different system architectures will be given. The design of the analog front-

end, which sets the noise performance of the system is considered. Then techniques to tune and compensate for non-idealities such as the frequency split between the two modes, the quadrature errors, the anisotropy of the resonator, and instability of the device are considered.

### **1.4.1 System Architectures**

There are several different architectures for the readout of the rotation rate of a CVG. The first and most common is amplitude modulation (AM). However there are several other methods, including frequency modulation (FM) and phase modulation (PM) architectures.

AM gyroscope interfaces are the most commonly used interface architecture and are widely used in commercial MEMS gyroscopes. A single mode, the drive mode, is excited at a constant velocity. The sense loop is then operated in either an open-loop configuration or a force-to-rebalance configuration. Under rotation, the drive mode couples to the sense mode through the Coriolis force, directly modulating the amplitude of the sense mode readout signal. The rate output can be read by demodulating the sense mode pickoff current with respect to the drive input signal and taking the DC component by low-pass filtering. The rate output can also be read using a force-to-rebalance method where the sense mode is nulled using a control loop. The control voltage of this loop is then directly proportional to the force required to null the Coriolis force and hence is proportional to the rotation rate.

FM or quadrature FM (QFM) interfaces drive both the drive and sense modes at an equal amplitude and a frequency close to the natural frequency of the two degenerate modes. [57] This causes the trajectory of the equivalent pendulum model of the device to rotate in a circular pattern. If the device is then rotated, the frequency of this rotation will remain exactly the same in the inertial frame of the pendulum, however it will appear to

shift in frequency in the rotating reference frame. Hence the rotation rate can be sensed in the rotating frame by measuring this perceived frequency shift.

The FM interface has several advantages when compared to an AM interface. The scale factor is independent of  $Q$ , the electromechanical coupling factor, and angular acceleration. It has a larger bandwidth and Mode matching is also trivial since you are driving both modes and hence have greater controllability and observability of the sense mode in comparison to open loop sense architectures common in AM interfaces. This easy mode matching leads to advantages in the noise performance and reduces the errors caused by small mismatches in mode-matched AM interfaces. However the FM interface has a worse rate offset and the scale factor is still sensitive to anisotropic damping. It also requires a very accurate frequency reference or the use of dual resonators to measure the change in frequency differentially, cancelling out the common mode zero rate frequency as done in [57]. This differential design also has the potential to cancel out many common mode environmental effects if a linear orbital trajectory is used instead of a circular one. [58, 59]

Phase modulated interfaces read the angular rotation rate by reading the phase difference caused by the Coriolis force. [60] Similar to the FM interface, the PM readout requires that both modes, now termed I and Q, are excited with equal amplitudes. The current sense outputs of each of the two modes are equal in amplitude but the phase shift between the sense output of each mode and its drive input is directly proportional to the rotation rate. This method of read-out also enables self-calibration and self-test methods without physical rotation of the device. [61, 62]

The three main components of the interface are the drive channel, sense channel, and biasing and compensation channel. The drive channel actuates the device, driving it into resonance. The sense channel reads out the rotational signal being sensed. The biasing and compensation channel provides the DC biasing to enable the capacitive interface and electrostatically compensate for fabrication imperfections.

### 1.4.2 Whole-angle mode

One of the great advantages of the axial-symmetric structure of the  $\mu$ HRG is that the device can be operated in whole-angle or rate integrating mode. This mode of operation allows the angle of rotation to be directly measured. Direct measurement of the rotation angle avoids the integration of the rotation rate that normally introduces further drift into measurements of the rotation angle.

In whole angle mode the vibration pattern is allowed to precess freely and ideally without a preferential orientation. Since whole-angle mode does not rely on force feedback like force to rebalance operation, it has a larger, ideally infinite, dynamic range. However, since the vibration pattern is no longer fixed along the drive electrodes' axis, the drive and sense electronics are more complex and the performance is more susceptible to anisotropy and is dependent on the ring-down time of the resonator. For example the angle estimate,  $\phi$ , requires the tracking of both the position and velocity of both components, x and y, of the 2-dimensional precessing vibration pattern as shown in Equation 10.

$$\tan 2\phi = \frac{2(\omega_0^2 xy + \dot{x}\dot{y})}{\omega_0^2(x^2 - y^2) + (\dot{x}^2 - \dot{y}^2)}$$

**Equation 10: Whole angle mode angular readout**

The ring-down time of the resonator is the product of the period of the resonator at the resonant frequency and the quality factor. In order to operate in whole-angle mode the quality factor of the device must be large, and the frequency must be low in order to have a long ring-down time. The ring-down time is directly related to the performance of the device and needs to be optimized in the design of the resonator.

### 1.4.3 Analog Front-end Designs

The analog front-end provides a transimpedance stage and post-amplifiers for the sensing of the drive and sense mode currents along with input voltage buffering for the

drive signal and feed-through cancellation. The design of the transimpedance stage is critical for the electrical noise performance of the interface. There are several methods that can be used to implement this stage. These include a simple voltage follower, a switched capacitor integrator, a continuous time charge integrator, or a continuous time transimpedance amplifier (TIA) as shown in Figure 10.

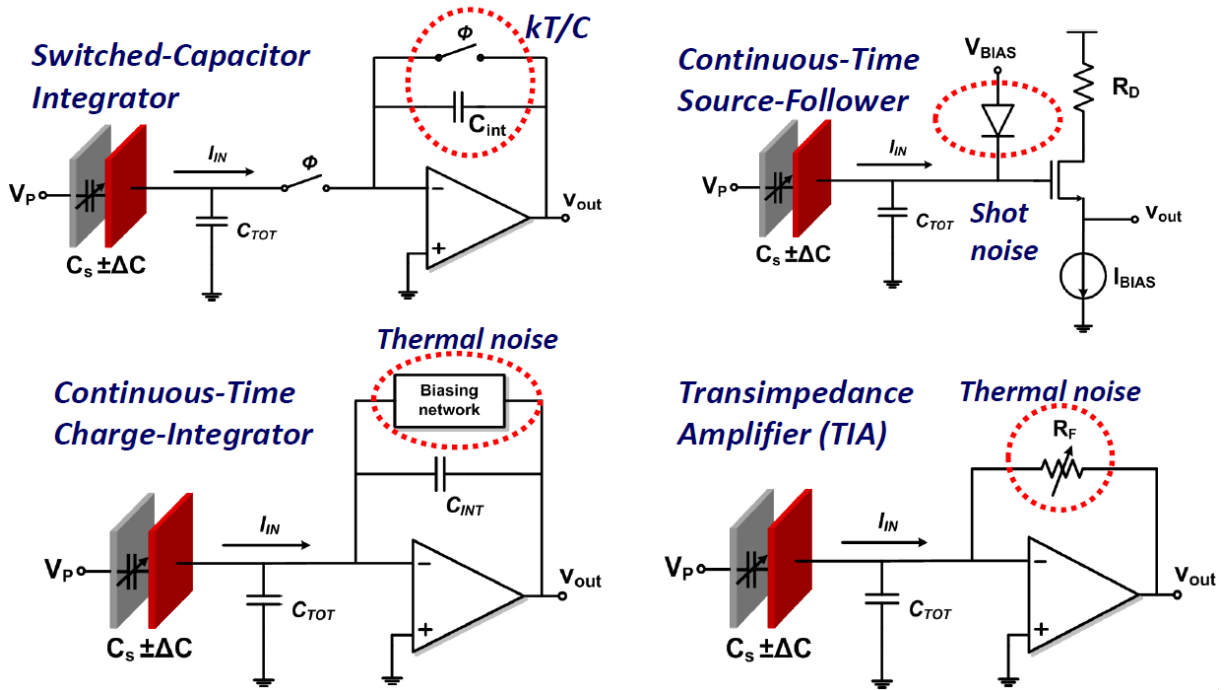


Figure 10: Analog Front-end Designs [63]

The voltage follower was used in [32] however its transimpedance gain relies on parasitic capacitances at the input node that are not well controlled. Also, the DC biasing diode contributes shot noise to the output. A switched capacitor integrator or switched capacitor TIA are common designs in digital systems that already include a clock and are already inherently discrete time systems. Adding a clock to the analog front-end would not only introduce additional complexity but also adds clock feed-through and power consumption concerns.

The continuous time TIA or trans-resistance amplifier (TRA) was used for both the drive and sense channel pick-off amplifiers. This front end design is low-noise and is capable of sensing sub-attofarad level capacitances in the sense channel. [53, 64] The noise performance of the basic TIA, as given in Equation 11 and Equation 12, is dominated by the feedback resistor and voltage noise of the op-amp. The design also lends itself well to AC coupling used to control the DC bias at the electrode in order to tune the frequency of each mode.

$$\overline{I_{N-tot}}^2 = \overline{i_{op-amp}}^2 + \frac{4k_B T}{R_f} + \overline{v_{opamp}}^2 \left( \frac{1}{R_f} + \frac{1}{R_{in-opamp}} + \omega C_{TOT} \right)^2$$

**Equation 11: Total noise of the TIA pick-off front-end**

$$ENE\Omega = \frac{\overline{I_{N-tot}} \sqrt{BW}}{Sensitivity} = \frac{g_0}{4V_{ps} C_0 Q_s X_d} \overline{I_{N-tot}} \sqrt{BW}$$

**Equation 12: Electrical noise equivalent acceleration (ENE $\Omega$ ) of the TIA pick-off front-end**

A continuous time charge integrator or trans-capacitance amplifier would make a suitable alternative. They are able to generate large AC impedances with reasonably sized capacitive feedback with the potential to be integrated into an ASIC. However they also require a very large feedback resistor to DC bias the input which contributes noise.

#### 1.4.4 Mode Matching

In practice the two degenerate modes of the resonator are fabricated with a frequency split between them. This frequency split is caused by fabrication imperfections of the device such as the anisotropy at the ring of the shell. This fundamental (as-fabricated) frequency split can be shown by using the Raleigh-Ritz solution for the resonant frequencies of the two modes to depend only on the fourth harmonic of the thickness variation. [47] It can also be shown that the fundamental frequency split is proportional to the thickness of the shell. This leads to the scaling laws for the fundamental  $\Delta f$  as shown in Equation 13 where  $h_0$  is the average thickness,  $M_0$  the

average mass per unit angle,  $h_4$  the coefficient of the fourth harmonic of the Fourier series representation of the thickness around the z-axis, and  $M_4$  the fourth harmonic of the mass distribution.

$$\frac{\Delta f}{f} \propto \frac{M_4}{M_0} \propto \frac{h_4}{h_0}$$

**Equation 13: Fundamental frequency split scaling law [47]**

The frequency split can be compensated using electrostatic spring softening that electrostatically alters the spring constant of each mode to match the frequency of the two modes. By controlling the DC bias voltage on the electrodes of the  $\mu$ HRG, the frequency of each mode can be tuned. This can be seen as an extra spring constant,  $k_{elec}$ , being added to the modal dynamics by the parallel plate capacitive interface as shown by Equation 14.

$$W = \frac{1}{2}cv^2 \quad \text{and} \quad F_{electrostatic} = \frac{dW}{dx} = \frac{1}{2} \frac{dC}{dx} V^2 = \frac{1}{2} \frac{dC}{dx} (V_P + V_{ac})^2$$

$$M \frac{d^2x}{dt^2} + D \frac{dx}{dt} + kx = F_{elec} = \frac{1}{2} \frac{dC}{dx} (V_P + V_{ac})^2$$

$$C = \frac{\epsilon_0 A}{(g-x)} = \frac{C_0}{(1-\frac{x}{g})}$$

For linear operation of the capacitive transducer the amplitude must be small ( $x < 0.1g$ )

$$\frac{dC}{dx} = \frac{C_0}{g(1-\frac{x}{g})^2} = \frac{C_0}{d} \underbrace{\left(1 + \frac{2}{g}x + \frac{3}{g^2}x^2 + \dots\right)}_{\text{Taylor Series Exp.}} \approx \frac{C_0}{d} \left(1 + \frac{2}{g}x\right)$$

$$F_{elec} = \frac{1}{2} (v_{ac}^2 + v_{ac}V_P + V_P^2) \frac{C_0}{d} \left(1 + \frac{2}{g}x\right)$$

$$= \frac{1}{2} V_P^2 \frac{C_0}{g} + V_P^2 \frac{C_0}{g^2} x + \underbrace{2v_{ac}V_P \frac{C_0}{g^2} x + v_{ac}^2 \frac{C_0}{g^2} x}_{\text{stiffness h.o.t.}} + v_{ac}V_P \frac{C_0}{g} + \underbrace{\frac{1}{2} v_{ac}^2 \frac{C_0}{g}}_{\text{small force h.o.t.}}$$

For a small excitation ( $v_{ac}$ ) the higher order terms (h.o.t.) will be minimized, hence:

$$F_{elec} \approx \frac{1}{2} V_P^2 \frac{C_0}{g} + V_P^2 \frac{C_0}{g^2} x + v_{ac}V_P \frac{C_0}{g}$$

$$M \frac{d^2 x}{dt^2} + D \frac{dx}{dt} + \underbrace{\left( k - V_P^2 \frac{C_0}{g^2} \right)}_{(k_{mech} - k_{elec})} x = \underbrace{\frac{1}{2} V_P^2 \frac{C_0}{g}}_{DC \text{ Force}} + \underbrace{v_{ac} V_P \frac{C_0}{g}}_{AC \text{ force}}$$

$$k_{elec} = -V_P^2 \frac{C_0}{g^2}$$

**Equation 14: Derivation of the electrostatic spring softening constant in a parallel plate transducer**

### 1.4.5 Quadrature Compensation

In order to fully match the modes with no frequency split the modes must not only have the same spring constant along their own axes but the cross-axis terms must be cancelled. The quadrature compensation aligns the modes along the axes of the electrodes by eliminating the cross-axis spring constants.

Similar to frequency tuning, the quadrature compensation can be accomplished using electrostatic spring softening. Since the off-diagonal terms of the spring constant matrix to be cancelled are related to anisotropy of the resonator, off-axis electrodes are used to compensate them. Equation 15 gives the spring constant matrix with the electrostatic quadrature and frequency tuning included.

$$\mathbf{k} = \begin{bmatrix} k_d & k_{ds} \\ k_{sd} & k_s \end{bmatrix} - \frac{1}{2} \frac{C_0}{g} \begin{bmatrix} (V_P - V_{T1})^2 & (V_P - V_{Qds})^2 \\ (V_P - V_{Qsd})^2 & (V_P - V_{T2})^2 \end{bmatrix} = \begin{bmatrix} k & 0 \\ 0 & k \end{bmatrix}$$

where  $V_{Qds}$  and  $V_{Qsd}$  are related to  $V_{Q1}$  and  $V_{Q2}$

**Equation 15: Spring constant matrix with electrostatic quadrature and frequency compensation**

### 1.4.6 Automatic Gain Control

In order to ensure a linear Coriolis force response, as given by Equation 1, the velocity of the drive mode must be held constant. Since the drive pickoff current is proportional to the drive velocity, this signal can be used as the input to a control loop to keep the amplitude of the velocity constant. Hence a second (outer) loop is needed to control the amplitude of the inner oscillator loop.

The automatic gain or level control (AGC or ALC) is a non-linear system. The system can still be analyzed by applying the method of averaging. [65, 66] Since the amplitude and phase of the drive amplitude are slowly varying, we can average their derivatives over one period to find the equilibrium point of the ALC control system. A block diagram of the ALC system is shown in Figure 11. An analysis of the ALC loop dynamics using the method of averaging is given in Equation 16. This analysis shows that in order for the drive loop to be stable, the PID constants and the LPF time constant must satisfy  $\lambda k_p > k_i$  where  $k_p$  is the proportional gain,  $k_i$  the integral gain and  $\lambda$  is related to the LPF time constant,  $\tau_{LPF}$  by  $\lambda = \frac{1}{\tau_{LPF}}$ .

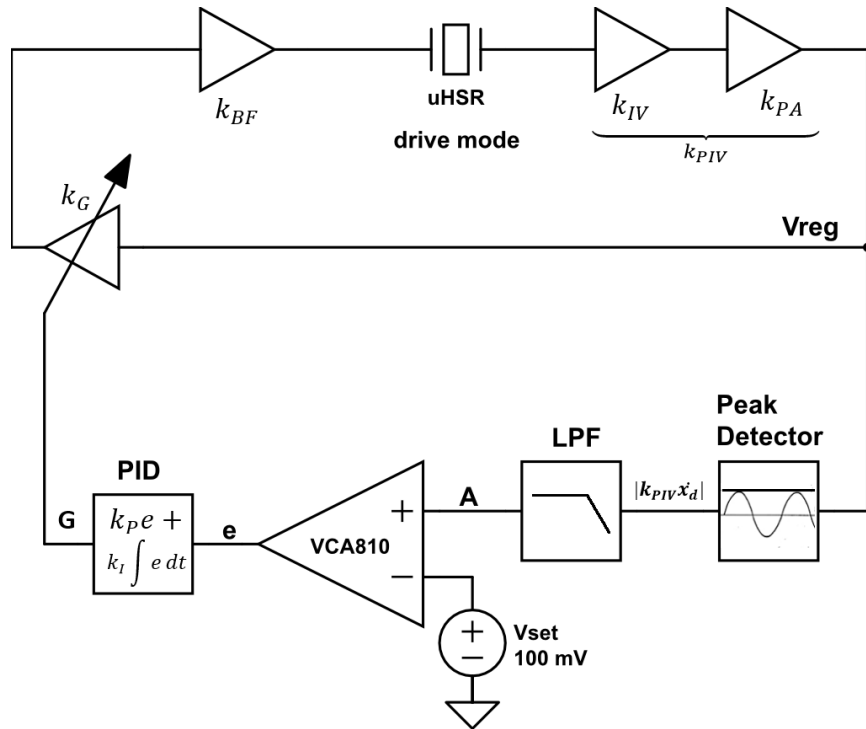


Figure 11: Automatic level control system

$$\ddot{x}_d + \frac{\omega_{nd}}{Q} \dot{x}_d + \omega_{nd}^2 x_d = \frac{F_{elec}}{m} = \frac{k_{PIV} k_{BF} G \dot{x}}{m}$$

Where  $k_{BF} = k_G k_B \underbrace{(-2V_{Pd} \frac{C_0}{g_0})}_{\substack{\text{Forcer} \\ \text{Electrode}}}$  is the Buffer side gain and  $k_{PIV} = \underbrace{2V_{Pd} \frac{C_0}{g_0}}_{\substack{\text{Pickoff} \\ \text{Electrode}}} k_{IV} k_{PA}$

Now we would like to eliminate the dampening hence:

$$\ddot{x}_d + \underbrace{\left( \frac{\omega_{nd}}{Q} - \frac{k_{PIV} G k_{BF}}{m} \right)}_{\text{Dampening} = 0} \dot{x}_d + \omega_{nd}^2 x_d = 0 \quad \rightarrow \quad \ddot{x}_d + \omega_{nd}^2 x_d = 0$$

$$\xrightarrow{\text{solution}} x_d = a(t) \cos(\omega_{nd} t + \phi(t))$$

$$\dot{x}_d = -a\omega_{nd} \sin(\omega_{nd} t + \phi) + \underbrace{\dot{a} \cos(\omega_{nd} t + \phi) - a\dot{\phi} \sin(\omega_{nd} t + \phi)}_{\equiv 0}$$

$$\dot{a} \cos(\omega_{nd} t + \phi) - a\dot{\phi} \sin(\omega_{nd} t + \phi) \equiv 0$$

$$\dot{x}_d = -a\omega_{nd} \sin(\omega_{nd} t + \phi)$$

$$\ddot{x}_d = -\dot{a}\omega_{nd} \sin(\omega_{nd} t + \phi) - a\omega_{nd}(\omega_{nd} + \dot{\phi}) \cos(\omega_{nd} t + \phi)$$

Let  $w = \omega_{nd} t + \phi$  hence by substituting back into the original dynamics we have:

$$\begin{bmatrix} -\dot{a}\omega_{nd} - a\omega_{nd} \left( \frac{\omega_{nd}}{Q} - \frac{k_{PIV} G k_{BF}}{m} \right) \sin(w) - a\omega_{nd} \dot{\phi} \cos w \\ \dot{a} \cos(w) - a\dot{\phi} \sin(w) \end{bmatrix} = \begin{bmatrix} 0 \\ 0 \end{bmatrix}$$

$$\begin{bmatrix} \sin(w) & a \cos(w) \\ \cos(w) & -a \sin(w) \end{bmatrix} \begin{bmatrix} \dot{a} \\ \dot{\phi} \end{bmatrix} = \begin{bmatrix} a \left( \frac{\omega_{nd}}{Q} - \frac{k_{PIV} G k_{BF}}{m} \right) \sin w \\ 0 \end{bmatrix}$$

Now we left multiply by a non-singular matrix:

$$\begin{aligned} & \begin{bmatrix} \cos w & -\sin w \\ \frac{1}{\omega_{nd}} \sin w & \frac{1}{\omega_{nd}} \cos w \end{bmatrix} \begin{bmatrix} \sin(w) & a \cos(w) \\ \cos(w) & -a \sin(w) \end{bmatrix} \begin{bmatrix} \dot{a} \\ \dot{\phi} \end{bmatrix} \\ &= \begin{bmatrix} \cos w & -\sin w \\ \frac{1}{\omega_{nd}} \sin w & \frac{1}{\omega_{nd}} \cos w \end{bmatrix} \begin{bmatrix} a \left( \frac{\omega_{nd}}{Q} - \frac{k_{PIV} G k_{BF}}{m} \right) \sin w \\ 0 \end{bmatrix} \\ & \begin{bmatrix} 0 & a \\ \frac{1}{\omega_{nd}} & 0 \end{bmatrix} \begin{bmatrix} \dot{a} \\ \dot{\phi} \end{bmatrix} = \begin{bmatrix} a \left( \frac{k_{PIV} G k_{BF}}{m} - \frac{\omega_{nd}}{Q} \right) \sin w \cos w \\ \frac{a}{\omega_{nd}} \left( \frac{k_{PIV} G k_{BF}}{m} - \frac{\omega_{nd}}{Q} \right) \sin^2 w \end{bmatrix} \end{aligned}$$

This gives the following set of differential equations:

$$\begin{bmatrix} \dot{a} \\ \dot{\phi} \\ \dot{A} \\ \dot{G} \end{bmatrix} = \begin{bmatrix} a \left( \frac{k_{PIV} G k_{BF}}{m} - \frac{\omega_{nd}}{Q} \right) \sin^2 w \\ \left( \frac{k_{PIV} G k_{BF}}{m} - \frac{\omega_{nd}}{Q} \right) \sin w \cos w \\ \lambda (|k_{PIV} a \omega_{nd} \sin w| - A) \\ -k_p \dot{A} + k_I (R - A) \end{bmatrix}$$

Now in order to apply the method of averaging we need:

$$\frac{k_p}{\omega_d} \propto \frac{k_I}{\omega_d} \propto \frac{\lambda}{\omega_d} \propto \frac{1}{Q} \ll 1$$

Hence since  $k_p, k_I,$  and  $\lambda$  are controlled by the designer and the device is assumed to have a high  $Q$ , we have:

$$\begin{aligned} \ddot{a} &= \frac{1}{T} \int_0^T \dot{a} dt \quad T = \frac{2\pi}{\omega_{nd}} \\ &= \frac{\omega_{nd}}{2\pi} \int_0^{\frac{2\pi}{\omega_{nd}}} \bar{a} \left( \frac{k_{PIV} G k_{BF}}{m} - \frac{\omega_{nd}}{Q} \right) \sin^2(\omega_{nd} t + \phi) dt \\ &= \frac{\bar{a}}{2} \left( \frac{k_{PIV} G k_{BF}}{m} - \frac{\omega_{nd}}{Q} \right) \end{aligned}$$

$$\begin{aligned} \dot{\phi} &= \frac{\omega_{nd}}{2\pi} \int_0^{\frac{2\pi}{\omega_{nd}}} \left( \frac{k_{PIV} G k_{BF}}{m} - \frac{\omega_{nd}}{Q} \right) \sin(\omega_{nd} t + \phi) \cos(\omega_{nd} t + \phi) dt \\ &= 0 \end{aligned}$$

*Note  $\phi$  is a constant that we can set to 0*

$$\begin{aligned} \dot{A} &= \frac{\omega_{nd}}{2\pi} \int_0^{\frac{2\pi}{\omega_{nd}}} \lambda (|k_{PIV} a \omega_{nd} \sin w| - A) dt \\ &= \lambda \left( \frac{2}{\pi} \omega_{nd} k_{PIV} \bar{a} - \bar{A} \right) \end{aligned}$$

Hence we have the following averaged system of equations:

$$\begin{bmatrix} \dot{\bar{a}} \\ \dot{\bar{\phi}} \\ \dot{\bar{A}} \\ \dot{\bar{G}} \end{bmatrix} = \begin{bmatrix} \frac{\bar{a}}{2} \left( \frac{k_{PIV} G k_{BF}}{m} - \frac{\omega_{nd}}{Q} \right) \\ 0 \\ \lambda \left( \frac{2}{\pi} \omega_{nd} k_{PIV} \bar{a} - \bar{A} \right) \\ -k_P \dot{\bar{A}} + k_I (R - \bar{A}) \end{bmatrix}$$

At equilibrium we have  $\dot{\bar{a}} = \dot{\bar{\phi}} = \dot{\bar{A}} = \dot{\bar{G}} = 0$  and hence:

$$\begin{bmatrix} \bar{a}_{eq} \\ \bar{\phi}_{eq} \\ \bar{A}_{eq} \\ \bar{G}_{eq} \end{bmatrix} = \begin{bmatrix} \frac{\pi R}{2 \omega_{nd} k_{PIV}} \\ 0 \\ R \\ \frac{m \omega_{nd}}{Q k_{PIV} k_B} \end{bmatrix}$$

Now we take the Jacobian of the dynamic system at the equilibrium point:

$$J(\bar{a}_{eq}, \bar{A}_{eq}, \bar{G}_{eq}) = \begin{bmatrix} 0 & 0 & \frac{\pi k_{BF} R}{4 \omega_{nd} m} \\ \frac{2}{\pi} \lambda \omega_{nd} k_{PIV} & -\lambda & 0 \\ -\frac{2}{\pi} \lambda \omega_{nd} k_{PIV} k_P & \lambda k_P - k_I & 0 \end{bmatrix}$$

Now we calculate the stability criteria by first calculating the characteristic equation and then applying the Routh-Hurwitz criteria for stability:

$$\begin{aligned} |J(\bar{a}_{eq}, \bar{A}_{eq}, \bar{G}_{eq}) - sI| &= 0 \\ s^3 + \lambda s^2 + \frac{1}{2} \frac{k_{BF} k_{PIV} R}{m} \lambda k_P s + \frac{1}{2} \frac{k_{BF} k_{PIV} R}{m} \lambda k_I &= 0 \end{aligned}$$

$$\text{Stability Condition: } \lambda k_P > k_I$$

**Equation 16: Derivation of the ALC dynamics, equilibrium point, and stability criteria [65, 66]**

### 1.4.7 Bias Drift Compensation

Mode-reversal is a method of cancelling out part of the bias drift caused by low frequency noise by reversing the drive and sense axes. This can be done in several different ways. It can be done by switching between two discrete drive and sense axes.

[67] This method is able to cancel the noise since the Coriolis signal changes sign but not the noise. This is similar to correlated double sampling in an amplifier.

The mode-reversal method can also be applied using a method similar to chopping in an amplifier where the vibration pattern is continuously rotated from the drive to the sense axis. [68] This method avoids aliasing of noise into the rate output and demonstrated a reduction in the bias drift by a factor of about 5.

# Chapter 2

## $\mu$ HRG Rate Interface Design and Analysis

### 2.1 Device Characterization

Before the  $\mu$ HSR could be interfaced, the resonator needed to be characterized to develop an understanding of its performance and limitations. While both the  $m=2$  and  $m=3$  modes can be used for gyroscope operation, the focus will be on the  $m=2$  modes with the lowest frequency. The frequency response, ring down time and linearity of the device were measured. The device characterized is a poly-silicon shell with the characteristics described in Table 3.

#### 2.1.1 Frequency Response and Frequency Split

The frequency response and frequency split between the 2 degenerate modes was measured under a vacuum pressure of less than 5  $\mu$ Torr using an Agilent E5061B network analyzer with a low frequency gain-phase measurement port. The frequency response of the interfaced device is presented in Figure 12. The  $m=2$  modes both exhibit a Q of 8,500 and are centered at 6.6 kHz. The  $m=3$  mode with a Q of 7000 is located at 19.1 kHz and the  $m=4$  mode with a Q of 10,400 is located at 40.4 kHz.

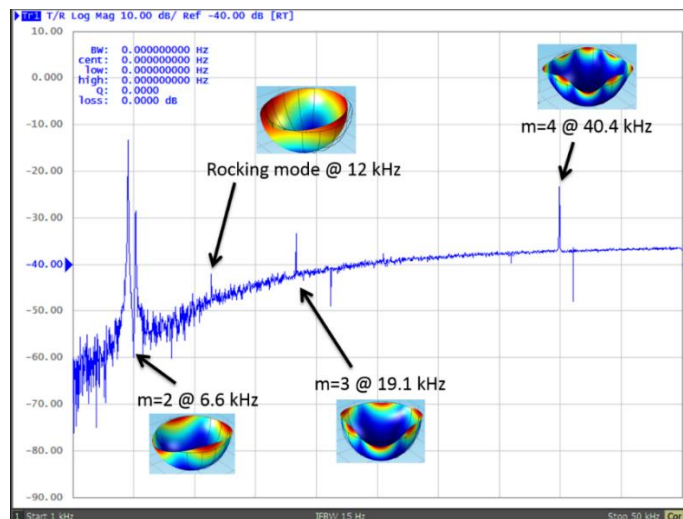


Figure 12: Frequency response of the interfaced  $\mu$ HSR

The frequency split of the  $m=2$  modes is shown in Figure 13. The  $m = 2$  modes have an as-fabricated ( $V_p = 0\text{v}$ ) frequency mismatch of 105 Hz. This small frequency split allows the two modes to be matched using electrostatic tuning.

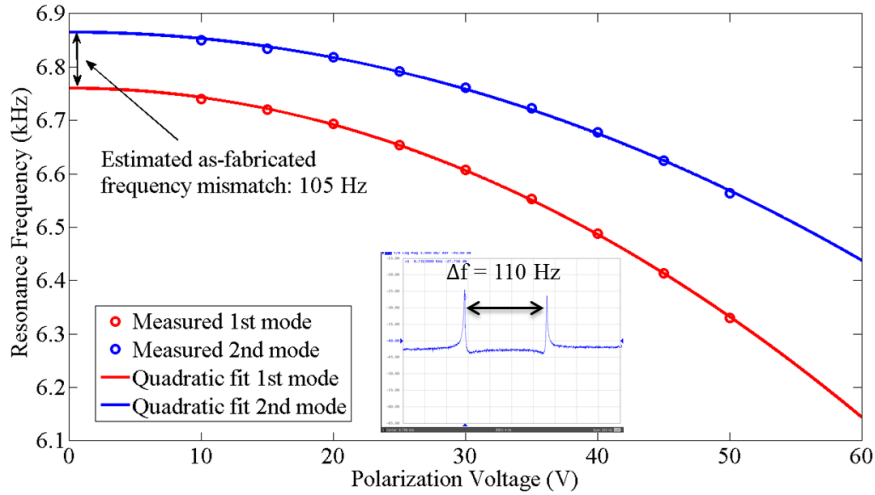
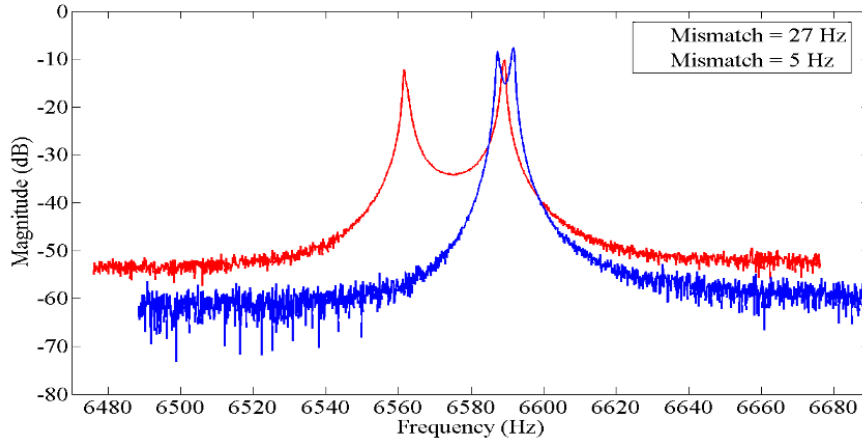


Figure 13: Frequency split between the  $m=2$  modes

### 2.1.2 Matched Frequency Response and Modelling

The two degenerate  $m=2$  modes can be matched using a set of electrostatic quadrature and frequency tuning electrodes. As discussed in section 1.4.4, these electrodes enable one to electrostatically soften the spring constant of each mode and compensate the quadrature. Figure 14 shows the reduction in the frequency split from 27 Hz down to 5 Hz as the two  $m=2$  modes are matched. Figure 15 shows the final resonant peak after mode matching.



**Figure 14: TWO M=2 MODES AS THE FREQUENCY SPLIT BETWEEN THE MODES IS REDUCED FROM 27HZ TO 5 HZ.**

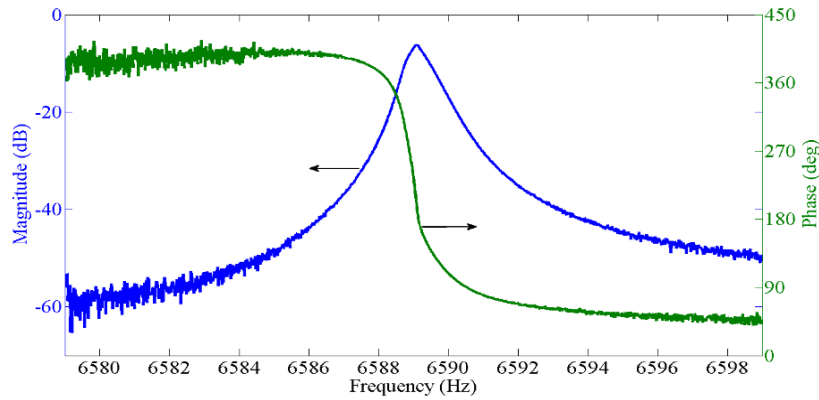


**Figure 15: Mode-matched m=2 peak**

### 2.1.3 Ring-down Measurements

As a low frequency axisymmetric device, the  $\mu$ HRG is an excellent candidate for operating in whole angle mode. In whole angle mode the vibration pattern of the device is allowed to freely rotate. In the absence of an amplitude control loop the amplitude of the vibration pattern will decay exponentially. This decay is caused by a variety of energy dissipation mechanisms including air dampening, support loss, thermo-elastic dampening, and surface roughness. The ring down time is the time constant,  $\tau$ , of the decay's amplitude envelope. The ring down time is related to the quality factor and frequency of the device by Equation 17 where  $Q$  and  $\omega_{res}$  are the quality factor and

angular frequency of the mode. The ring down time can be used as a time domain measure of the energy dissipation of the resonator to complement the frequency domain characterization captured by the quality factor.

$$\tau = \frac{2Q}{\omega_{res}}$$

**Equation 17: Ring down time relationship with quality factor**

The ring down times and quality factors were measured for a  $\mu$ HRG with assembled electrodes and then a  $\mu$ HRG with integrated electrodes. The ring down time was measured using the configuration shown in Figure 16. The device is driven at the resonant frequency using a network analyzer. A pickoff channel implemented with a gain of  $233M\Omega$  was used to monitor the motional current of two different electrodes  $45^\circ$  apart. Ring-down times of 270ms and 292ms were observed for the  $0^\circ$  and  $45^\circ$  electrodes respectively as shown in Figure 17.

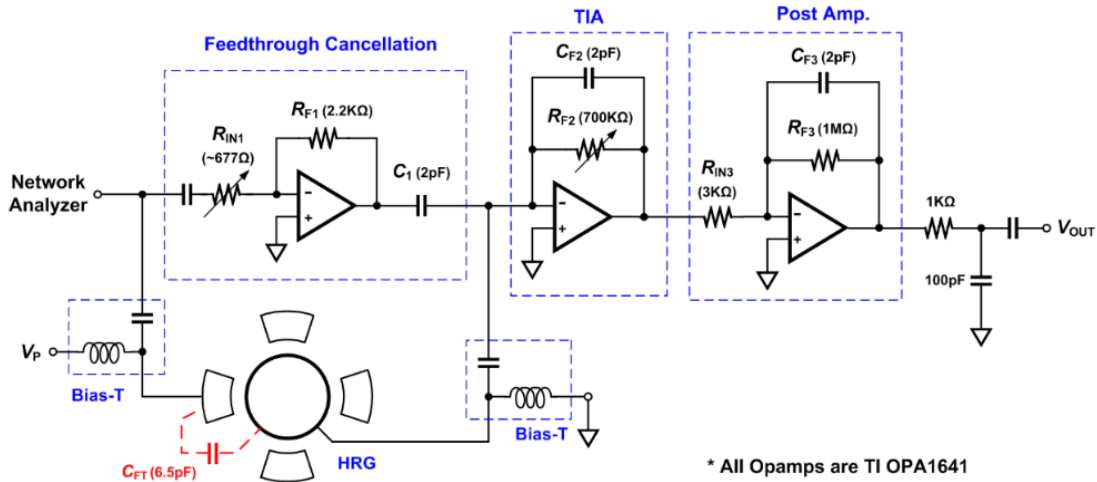


**Figure 16: Ringdown measurement configuration**

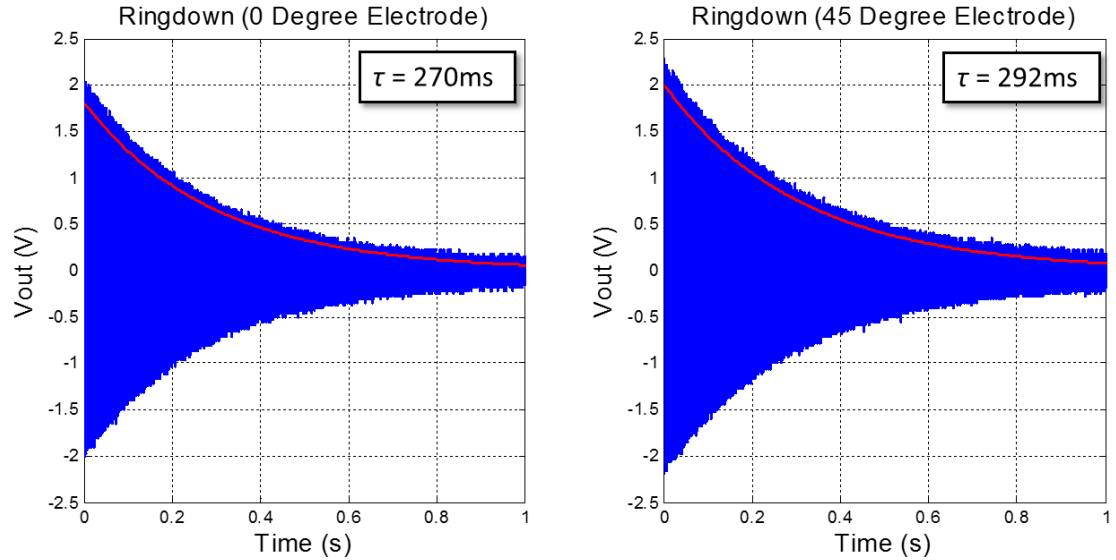


**Figure 17: Ring Down Time Measurements**

Next a polysilicon device with integrated electrodes was tested using a configuration similar to the one in Figure 16. The ring down time, shown in Figure 18, was measured to be 600ms, giving an effective quality factor of 22k. However the frequency response of the device showed a Q of 30k. The frequency response measurement was conducted at a drive amplitude of around 5mV, whereas a drive amplitude of 3v was needed for the ring down measurements in order for the signal levels to be large enough to measure the ring down time. This large drive amplitude drives the device into non-linearity, decreasing the measured ring-down time of the device. This non-linearity can also be seen directly in the ring down measurement plot as a step when the drive signal is removed and the device starts to ring down.

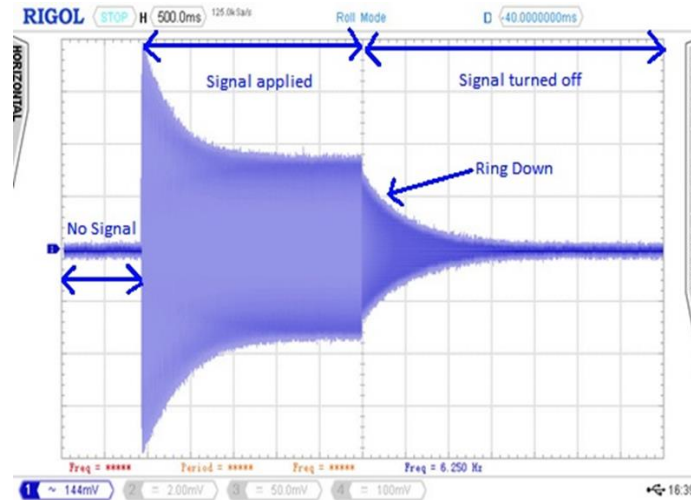
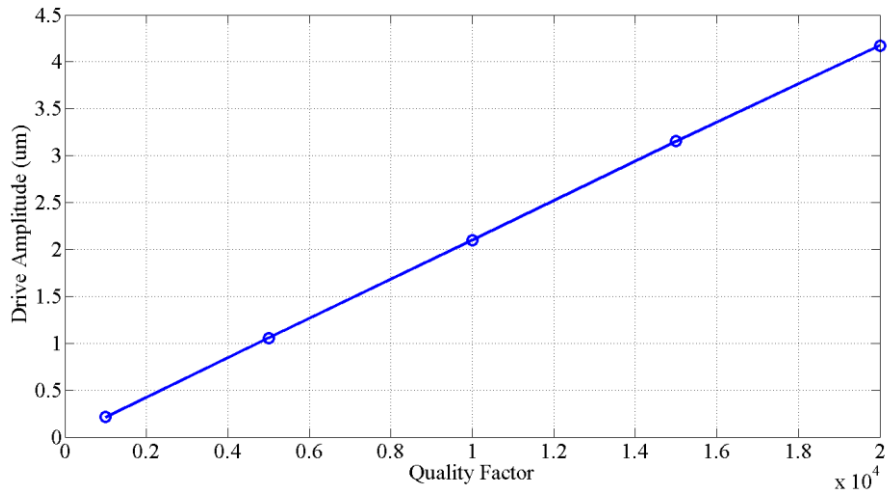


Figure 18: Ring down time measurement of a polysilicon device with a Q of 30k

### 2.1.4 Linearity

The linearity of the  $m=2$  modes is important for the gyroscope performance of the device including the linearity and magnitude of the scale factor. The device has  $20\mu\text{m}$  capacitive gaps between the shell and the integrated electrodes. In order to get an idea of the amplitude of the shell displacement the shell was simulated using finite element method (FEM) software with a DC bias of 40v and an AC drive voltage of 30mV. The drive displacement amplitude as a function of the device quality factor is given in Figure 19. The simulation predicts that with a Q of 11,000, the drive displacement amplitude is  $2.25\mu\text{m}$ . A displacement amplitude of 11% of the gap size for a non-linear sensing element such as a parallel plate electrode can induce non-linearity in the peak shape of the resonance mode.



**Figure 19: Device Drive Displacement Amplitude with a DC bias of 40v, 20  $\mu\text{m}$  gap size and an AC drive voltage of 30 mV**

This non-linearity was measured as the AC drive amplitude was swept from 4.75mV to 115mV with a mode-matched  $\mu\text{HRG}$  at a DC bias voltage of 14v as shown in Figure 19. The device begins to enter non-linearity at drive amplitudes of 12mV and above. This limits the amplitude of the drive mode to less than 10mV.

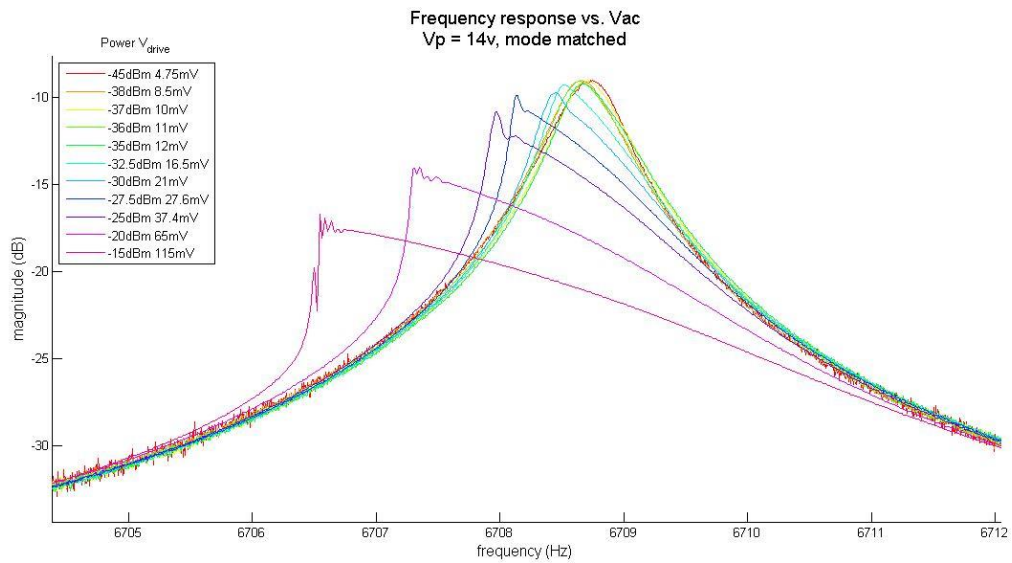


**Figure 20: Frequency response as Vac is swept from 4.75mV to 115mV showing the onset of non-linearity as Vac increases**

### 2.1.5 Substrate Feed-through Effects

The capacitive feed-through of the device from the drive forcer where the device is actuated to both the drive and sense electrodes is mainly caused by capacitive coupling between the substrate and the device electrodes. While in more traditional MEMS structures the feedthrough might be caused by direct coupling between electrodes or the resonant device, the large gap size of the  $\mu$ HRG helps minimize this source of feed-through. The capacitive coupling between the electrodes and the substrate is caused by the large bonding pad area of the electrodes. The resistivity of the device wafers is nominally 10-50 ohm-cm with some of the newer devices with a front-side hole having a resistivity of 5-50 mohm-cm. The device feed-through levels can be effectively reduced by placing multiple bonds connecting the top-side of the device substrate at discrete openings in the passivation layer to  $V_P$ . The reduction of the feed-through level of the  $\mu$ HRG with different quantities of top side substrate bonds is shown in Figure 22.

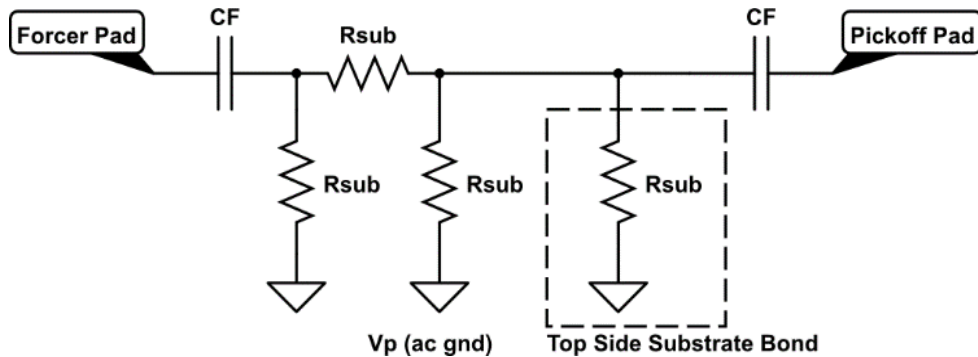


Figure 21: Feedthrough Model

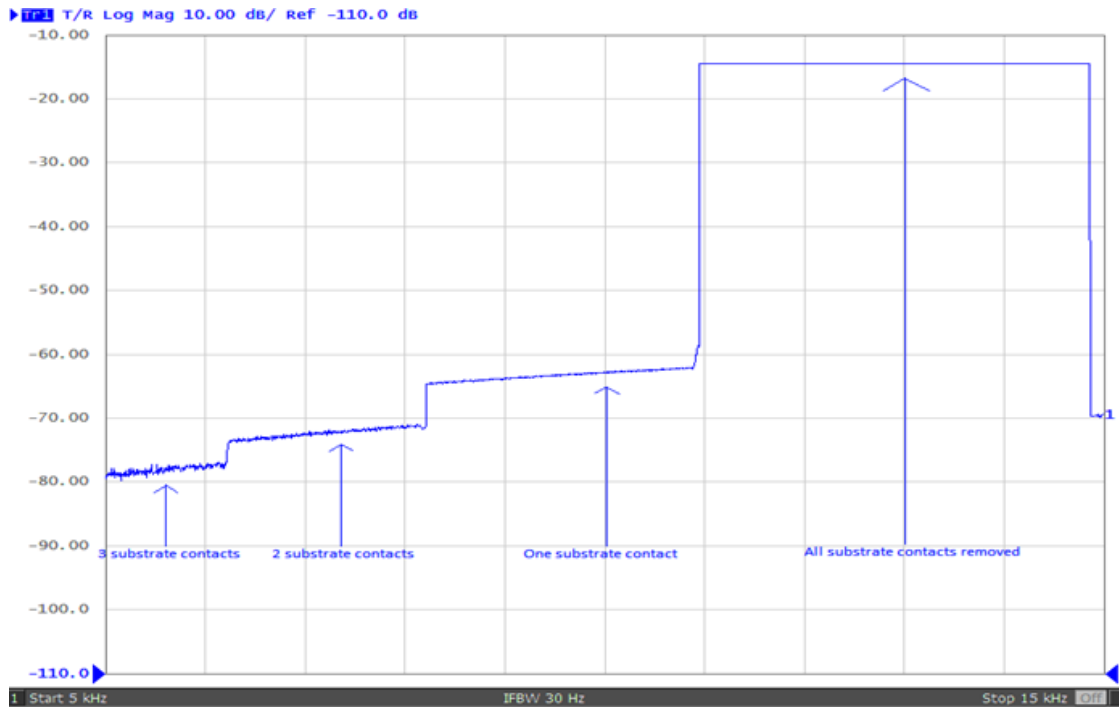


Figure 22: Top-side substrate bond effect on feed-through

## 2.2 $\mu$ HSR Model

The  $\mu$ HSR device model for a single mode is analogous to a one dimensional harmonic oscillator as depicted in Figure 23. The spring constant,  $k$ , is proportional to the stiffness of the device. The dampening constant is proportional to the dampening mechanisms of the device including air dampening, support loss, surface losses, etc. The mass,  $M$ , is the equivalent mass of the shell structure.

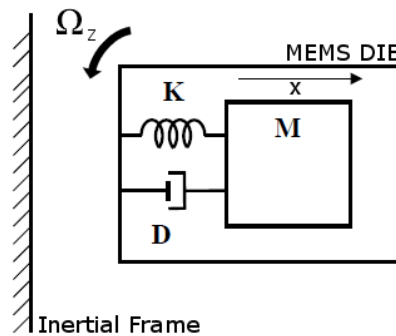


Figure 23: First Order Harmonic Oscillator System

## 2.2.1 Drive Mode Analysis: First Order Model

The analysis of the  $\mu$ HSR drive mode transfer function is best performed by breaking the system down into several series subsystems as shown in Figure 24 for a system in resonance. The first subsystem consists of the drive forcer electrodes that actuate the device to apply an electrostatic force,  $F_d$ , to the shell proportional to the AC drive voltage,  $V_{ac}$ . The second is the transfer function of the device resonance mode that generates a displacement,  $x_{df}$ , from the applied force. The third subsystem captures the phase difference between the drive forcer displacement,  $x_{df}$ , and the drive pickoff displacement,  $x_{dp}$ , caused by the mode shape. The final subsystem is the drive pickoff electrode that generates the motional current,  $I_{mot-d}$ , electrostatically from the displacement of the shell along the electrode's axis. The Magnitude and phase of the drive signal at resonance is given by Equation 18.

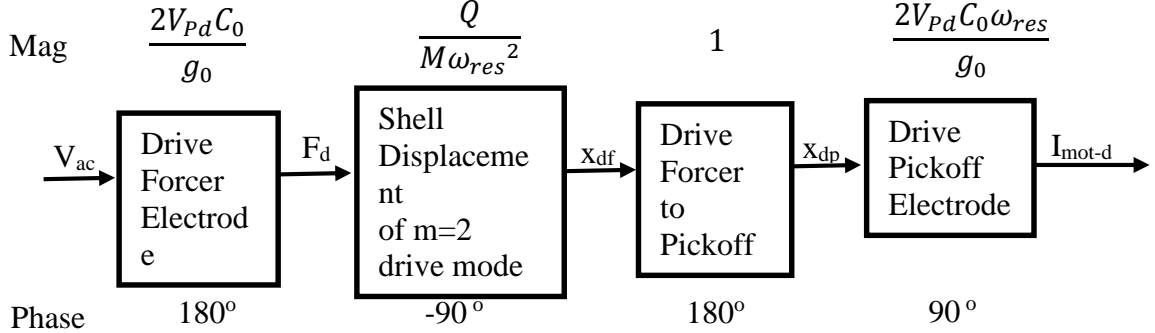


Figure 24: Drive Mode Model

$$\left\| \frac{I_{mot-d}(j\omega_{res})}{V_{ac}(j\omega_{res})} \right\| = \frac{4V_{Pd}^2 C_0^2}{Mg_0^2 \omega_{res}} \quad \text{and} \quad \angle \frac{I_{mot-d}(j\omega_{res})}{V_{ac}(j\omega_{res})} = 0^\circ$$

Equation 18: Drive Mode Magnitude and Phase





Figure 26:  $\mu$ HSR with all 16 electrodes wire-bonded to the AFE.

### 2.2.3 Drive Forcer Electrodes

The device is actuated using integrated electrodes that operate as parallel plate capacitors driven by an AC voltage,  $V_{ac}$ , to apply an electrostatic force,  $F_d$ , to the shell. The transfer function with the gain and phase of this subsystem are derived in Equation 19.

$$W = \frac{1}{2}Cv^2$$

$$F = \frac{dW}{dx} = \frac{1}{2} \frac{dC}{dx} V^2$$

$$F_d = 2(F_{df} - F_{dp}) = \left( v_{ac} - (V_{df} - V_{shell}) \right)^2 \frac{dC_{df0}}{dx_{df}} - (V_{df} - V_{shell})^2 \frac{dC_{dp0}}{dx_{dp}}$$

Assumptions:

$$x_d = x_{dp} = -x_{df} \ll g_0$$

$$C_{df0} = C_{dp0} = C_0$$

$$V_{df} = V_{dp} = V_{T1} \quad \text{by design}$$

$$\begin{aligned}
&\rightarrow V_{Pd} = \text{Drive polarization Voltage} \\
&= V_{df} - V_{shell} = V_{dp} - V_{shell} = V_{T1} - V_{shell} \\
&F_d = ((V_{ac} - V_{Pd})^2 - V_{Pd}^2) \frac{dC_0}{dx_d}
\end{aligned}$$

Taking the first term of the series approximation for  $\frac{dC_0}{dx_d}$  we have:

$$\begin{aligned}
\frac{dC_0}{dx_d} &\approx \frac{C_0}{g_0} \\
F_d &= (v_{ac}^2 - 2v_{ac}V_{Pd}) \frac{C_0}{g_0}
\end{aligned}$$

Since  $v_{ac} < 15\text{mV}$  for linear operation

$$\begin{aligned}
F_d &\approx -2 \frac{V_{ac}V_{Pd}C_0}{g_0} \\
\left\| \frac{F_d}{V_{ac}} \right\| &\approx 2 \frac{V_{Pd}C_0}{g_0} \quad \text{and} \quad \angle \frac{F_d}{V_{ac}} = 180^\circ
\end{aligned}$$

**Equation 19: Derivation of the Drive Forcer Electrodes' Transfer Function**

#### 2.2.4 Modal Dynamics

The dynamics of the drive mode can be modelled as a one-dimensional harmonic oscillator as shown in Figure 23. Starting with the free body diagram for the one-dimensional harmonic oscillator we can derive the transfer function for the drive mode and the gain and phase at resonance as given in Equation 20.

$$\begin{aligned}
M \frac{d^2x_d}{dt^2} + D \frac{dx_d}{dt} + kx_d &= F_d \\
\omega_{res} &= \sqrt{\frac{k}{M}} \quad \text{and} \quad Q = \frac{1}{D} \sqrt{kM} \\
\mathcal{L} \left\{ \frac{x_d(t)}{F_d(t)} \right\} \Big|_{s=j\omega} &= \frac{X_d(j\omega)}{F_d(j\omega)} = \frac{1}{M\omega_{res}^2} \frac{1}{\left(1 - \frac{\omega^2}{\omega_{res}^2}\right) + j\frac{1}{Q}\left(\frac{\omega}{\omega_{res}}\right)} \\
\left\| \frac{X_d(j\omega)}{F_d(j\omega)} \right\| &= \frac{1}{M\omega_{res}^2} \frac{1}{\sqrt{\left(1 - \frac{\omega^2}{\omega_{res}^2}\right)^2 + \left(\frac{1}{Q}\left(\frac{\omega}{\omega_{res}}\right)\right)^2}}
\end{aligned}$$

$$\angle \frac{X_d(j\omega)}{F_d(j\omega)} = \arctan\left(\frac{-\omega/\omega_{res}}{Q\left(1 - \left(\frac{\omega}{\omega_{res}}\right)^2\right)}\right)$$

Operating at resonance  $\omega = \omega_{res}$

$$\left\| \frac{X_d(j\omega)}{F_d(j\omega)} \right\| = \frac{Q}{M\omega_{res}^2} \quad \text{and} \quad \angle \frac{X_d(j\omega)}{F_d(j\omega)} = -90^\circ$$

**Equation 20: Derivation of the drive modal dynamics**

### 2.2.5 Drive Pickoff Electrodes

The drive pickoff electrode is located  $90^\circ$  from the drive forcer electrode. Given this position and the mode shape of the  $m=2$  mode as shown in Figure 25, the drive pickoff electrode is  $180^\circ$  out of phase with the drive forcer electrode as given in Equation 21.

$$x_{df}(t) = -x_{dp}(t)$$

$$\left\| \frac{X_{dp}(j\omega)}{X_{df}(j\omega)} \right\| = 1 \quad \text{and} \quad \angle \frac{X_{dp}(j\omega)}{X_{df}(j\omega)} = 180^\circ$$

**Equation 21: Derivation of the drive forcer displacement to drive pickoff displacement**

The drive pickoff electrode converts the displacement of the shell into the motional current output. The analysis of the drive pickoff electrode is similar to that of the drive forcer as shown in Equation 22.

$$Q = CV$$

$$I(t) = \frac{dQ}{dt} = C \overbrace{\frac{dV}{dt}}^0 + V \frac{dC}{dt} = V \frac{dC}{dt} = V \frac{dC}{dx} \frac{dx}{dt}$$

Applying the Taylor Series Approximation for both sense electrodes:

$$\frac{dC_0}{dx_d} \approx \frac{2C_0}{g_0}$$

$$I(t) = 2V_{Pd} \frac{C_0}{g_0} \frac{dx}{dt}$$

$$I(j\omega) = \mathcal{L} \left\{ 2V_{Pd} \frac{C_0}{g_0} \frac{dx}{dt} \right\} \Big|_{s=j\omega} = 2V_{Pd} \frac{C_0}{g_0} j\omega X(j\omega)$$

$$\frac{I(j\omega)}{X(j\omega)} = j2 \frac{V_{Pd} C_0}{g_0} \omega$$

Operating at resonance  $\omega = \omega_{res}$

$$\left\| \frac{I(j\omega)}{X(j\omega)} \right\| = \frac{2V_{Pd} C_0 \omega_{res}}{g_0} \quad \text{and} \quad \angle \frac{I(j\omega)}{X(j\omega)} = 90^\circ$$

**Equation 22: Derivation of the Drive Pickoff Electrodes' Transfer Function**

Note from Equation 22 that the drive pickoff current is proportional to the velocity of the drive mode. This shows that if the amplitude of the drive pickoff current is regulated a constant drive velocity is set, insuring a linear rotation rate response.

### 2.2.6 Electrical Model

In order to simulate the response of the device along with the circuit design of the interface, an electrical model of the device must be derived. The electrical model is formed by either a series or parallel RLC circuit. We will consider the series circuit. Each electrical component in the model has a direct mechanical analog as shown in Figure 27 and Table 4. The equations for deriving the electrical model from a given frequency response are given in Equation 23.

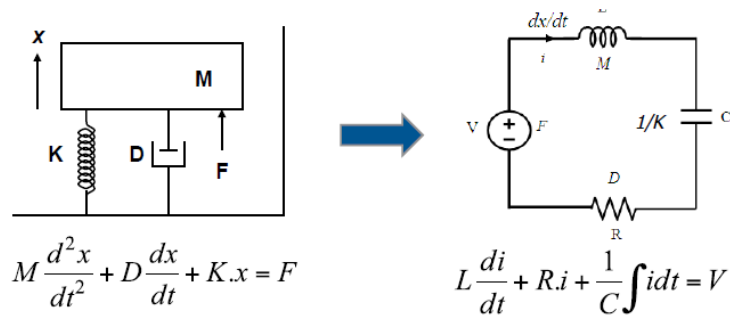


**Figure 27: Mechanical to electrical modelling analogy**

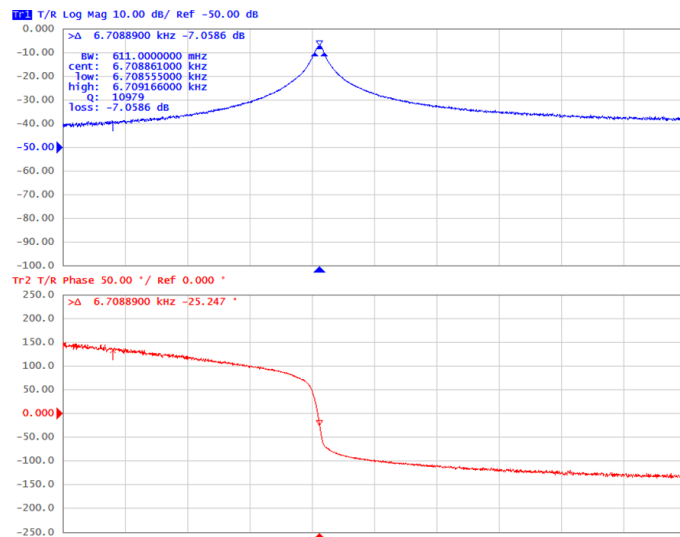
**Table 4: Mechanical to electrical modelling analogy equivalent components**

Mechanical	Electrical
Velocity	Current
Force	Voltage
Spring (K)	Capacitor (1/K)
Mass (M)	Inductor (M)
Damper (D)	Resistance (D)

$$R_{mot} = R_{TIA} 10^{\frac{IL(dB) - A_{post-amp}(dB)}{20}} \quad L_m = \frac{R_m * Q}{2\pi f_o} \quad C_m = \frac{1}{(2\pi f_o)^2 L_m}$$

**Equation 23: Electrical domain equivalent model of the  $\mu$ HSR**

The analogous electrical model of the mode-matched frequency response shown in Figure 28 will be derived. The insertion loss of the device will give us the motional resistance. At resonance the motional resistance along with the TIA forms a non-inverting amplifier which is equal to the insertion loss with the post-amplifier and buffer gains removed. Equation 23 was then applied using the frequency response parameters to derive the equivalent series circuit parameters as shown in Equation 24.



**From frequency response:  $IL = -7.0586 \text{ dB}$   $Q = 10,979$   $f_{res} = 6.70889 \text{ kHz}$**

**Figure 28: Measured Resonator Frequency Response**

$$R_{mot} = (500k\Omega)10^{\frac{-7.0586dB-20dB}{20dB}} = 11.268601 M\Omega$$

$$L_m = \frac{11.268601M\Omega * 10,979}{2\pi(6.70889kHz)} = 2,934,960.4 H$$

$$C_m = \frac{1}{(2\pi * 6.70889kHz)^2(2,934,960.4H)} = 191.75058 aF$$

Equation 24: Resonator drive mode equivalent RLC model parameters

### 2.2.7 Sense Mode Analysis: Second Order Model

In order to understand the relationship between the drive mode and the sense mode a second order model of the resonator is necessary. The model is an extension of the first order model that also models the dynamics of the sense mode. The second order model start with a two dimensional harmonic oscillator.

## Drive Mode

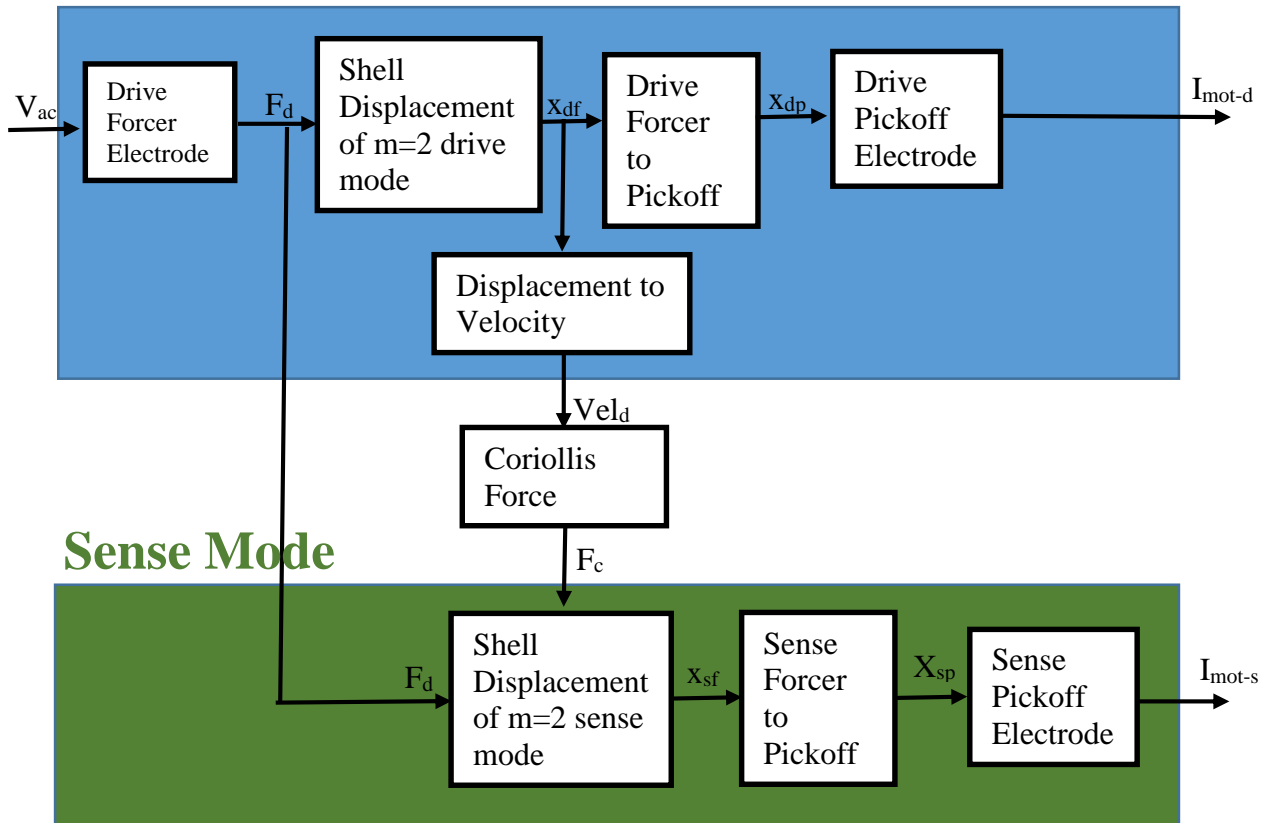


Figure 29: Device Model of both the drive and sense modes

The sense mode dynamics are modelled using the same harmonic oscillator model used for the drive mode. However now rather than using electrodes to drive the sense mode, the sense mode is coupled to the drive mode through the Coriolis force. We start by assuming an idealized model where the off diagonal terms of the dampening and spring matrices are all zero and the two modes are uncoupled. Then assuming the modes are matched we end up with the analysis in Equation 25.

$$M \frac{d^2 x_s}{dt^2} + D \frac{dx_s}{dt} + k x_s = F_c = -2M\Omega_z \frac{dx_d}{dt}$$

$$\omega_{s,res} = \sqrt{\frac{k_s}{M}} \quad \text{and} \quad Q_s = \frac{1}{D_s} \sqrt{k_s M}$$

$$\mathcal{L} \left\{ \frac{x_s(t)}{x_d(t)} \right\} \Big|_{s=j\omega} = \frac{X_s(j\omega_s)}{X_d(j\omega_s)} = \frac{1}{\omega_{s,res}^2} \frac{-2j\omega_d \Omega_z}{\left(1 - \frac{\omega_s^2}{\omega_{s,res}^2}\right) + j \frac{1}{Q_s} \left(\frac{\omega_s}{\omega_{s,res}}\right)}$$

$$\left\| \frac{X_s(j\omega_s)}{X_d(j\omega_d)} \right\| = \frac{1}{M\omega_{s,res}^2} \frac{2\omega_d \Omega_z}{\sqrt{\left(1 - \frac{\omega_s^2}{\omega_{s,res}^2}\right)^2 + \left(\frac{1}{Q_s} \left(\frac{\omega_s}{\omega_{s,res}}\right)\right)^2}}$$

$$\angle \frac{X_s(j\omega_s)}{X_d(j\omega_d)} = \arctan\left(\frac{Q_s \omega_{s,res}}{\omega_s} \left(1 - \left(\frac{\omega_s}{\omega_{s,res}}\right)^2\right)\right)$$

*Operating at resonance with the drive and sense modes matched:  $\omega = \omega_{s-res}$*

$$= \omega_{d-res}$$

$$\left\| \frac{X_s(j\omega_s)}{X_d(j\omega_d)} \right\| = \frac{2Q_s \Omega_z}{\omega_{s,res}} \quad \text{and} \quad \angle \frac{X_s(j\omega_s)}{X_d(j\omega_d)} = 0^\circ$$

**Equation 25: Derivation of the sense modal dynamics**

The sense mode is then read using a pair of parallel plate electrodes which generate a current from the displacement of the sense mode according to the transfer function given in Equation 22. This in combination with the sense modal dynamics gives the sense current as shown in Equation 26.

$$I_s(j\omega) = \frac{I_s(j\omega)}{X_s(j\omega)} \frac{X_s(j\omega_s)}{X_d(j\omega_d)} X_d(j\omega_d) = \frac{4V_{Ps}C_0\Omega_z}{g_0 \left[ \left(1 - \frac{\omega_s^2}{\omega_{s,res}^2}\right) + j \frac{\omega_s}{Q_s\omega_{s,res}} \right]} X_d(j\omega_d)$$

$$\|I_s(j\omega)\| = \frac{4V_{Ps}C_0X_d(j\omega_d)}{g_0 \sqrt{\left(1 - \frac{\omega_s^2}{\omega_{s,res}^2}\right)^2 + \frac{\omega_s^2}{Q_s^2\omega_{s,res}^2}}} \Omega_z$$

*Operating at resonance with the drive and sense modes matched:*

$$\omega = \omega_{s-res} = \omega_{d-res}$$

$$\|I_s(j\omega)\| = \frac{4V_{Ps}C_0X_d(j\omega_d)}{g_0} Q_s\Omega_z \quad \text{and} \quad \angle \frac{I_s(j\omega)}{X_d(j\omega_d)} = -90^\circ$$

**Equation 26: Sense mode displacement to motional current transfer function**

Then we can show the rate output is in phase with the drive forcer voltage that is used to demodulate the sense current:

$$\angle \frac{I_s(j\omega)}{V_{ac}(j\omega)} = \angle \frac{F_d(j\omega)}{V_{ac}(j\omega)} + \angle \frac{X_d(j\omega)}{F_d(j\omega)} + \angle \frac{I_s(j\omega)}{X_d(j\omega_d)} = 180^\circ - 90^\circ - 90^\circ = 0^\circ$$

**Equation 27: Phase relationship between drive voltage and sense current**

### ***2.3 Analog Front-End***

The analog front-end provides analog signal conditioning and feed-through cancellation. It also handles amplification of the quadrature and tuning voltages. It has four main subsystems: 2 forcer channels, 2 pickoff channels, 4 feed-through cancellation channels, and Voltage amplification for the 4 quadrature and tuning voltages. These main subsystems are shown in Figure 30. The analog front-end also includes provisions to accommodate an on-board vacuum chamber and has a custom chassis to provide mechanical support for the interface and on-board vacuum chamber.

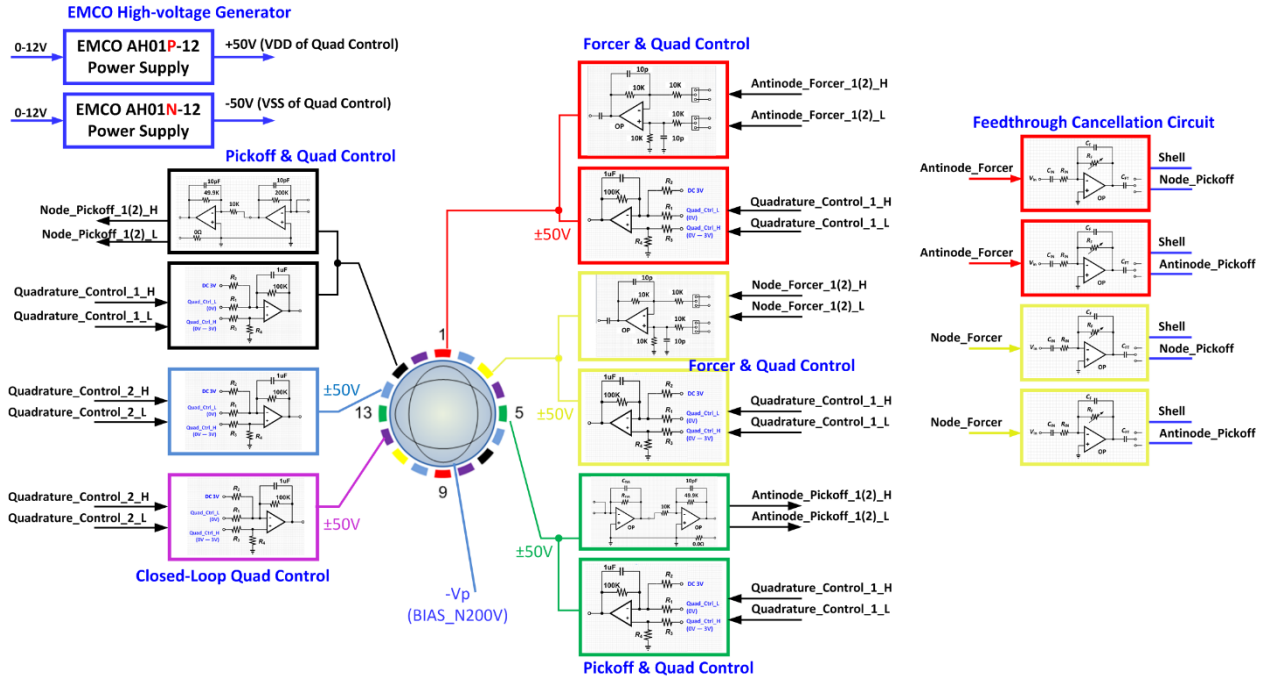


Figure 30: Analog Front-end Subsystem Configuration

### 2.3.1 Pick-off Channels

The pick-off channels for the sense (nodal) and drive (antinodal) modes consist of a trans-impedance amplifier (TIA) followed by a voltage post-amplifier. The input of the TIA is AC coupled to both of the pickoff electrodes through a  $1\mu\text{F}$  capacitor. The pickoff channel design is shown in Figure 31.

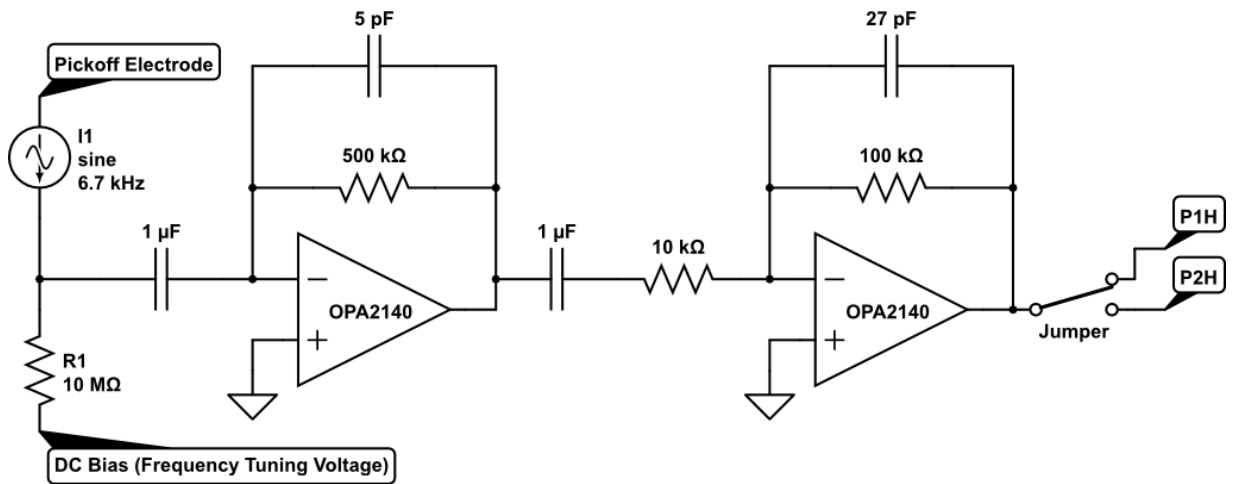


Figure 31: Pickoff Channel Design

The OPA2140 operational amplifier was selected for its low input bias current, low noise, and large bandwidth. The Specifications of the OPA2140 (2 channel) and OPA140 (1 channel) are given in Table 5. Both the TIA and Post-amp feedback capacitors were selected to limit the bandwidth of the device without introducing too much phase shift into the drive loop. Designing the TIA and post amp as low pass filters also prevents the TIA from exhibiting Gain (Qamp) peaking around the corner frequency. The corner frequencies were selected as:

$$TIA: f_c = 64kHz \quad \text{and} \quad Post\ Amp: f_c = 59kHz$$

**Table 5: OPA2140/OPA140 Specifications**

<b>OPA2140 Specifications</b>	
<b>GBW</b>	11 MHz
<b>Input Bias Current</b>	0.5 pA
<b>Voltage Noise</b>	5.1 nV/√Hz
<b>Current Noise</b>	0.8 fA/√Hz
<b>Quiescent Current</b>	2.0 mA/ch

The circuit was then simulated to verify the stability of the selected configuration and the expected frequency response. The AC simulation results are shown in Figure 32. The frequency response at the resonant frequency of 6.7 kHz shows a phase shift of -12.5°. The DC blocking Cap and the DC bias resistor form a high-pass filter at the input of the pickoff channel, but the corner frequency is low enough to prevent any attenuation at the resonant frequency.

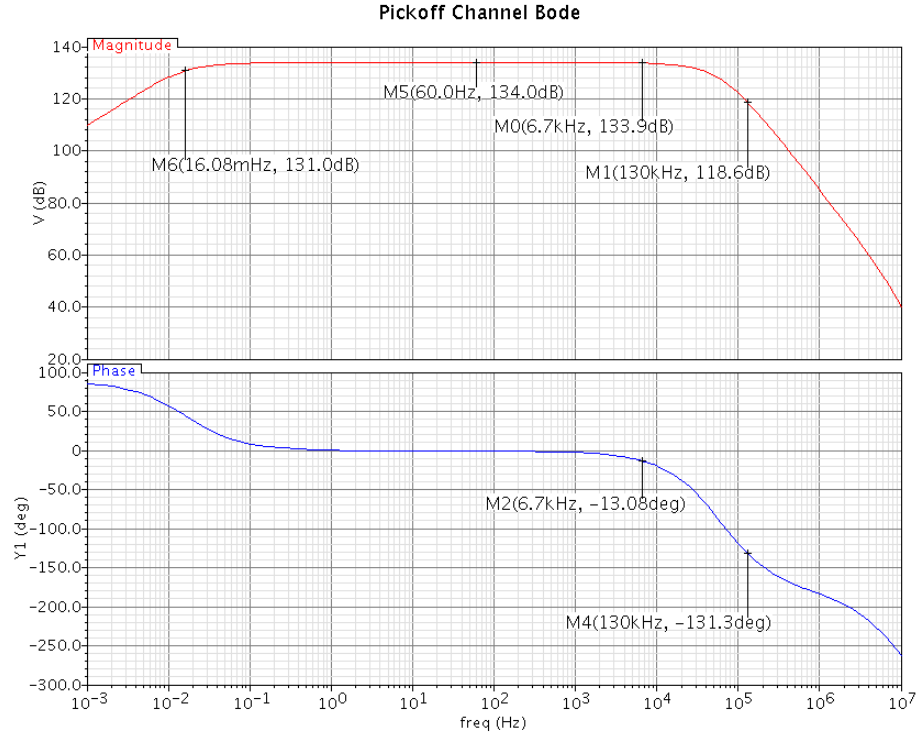


**Figure 32: Pickoff Channel Frequency Response (gain in dBΩ)**

$$\left\| \frac{V_{P2H}(j\omega_{res})}{I_{mot}(j\omega_{res})} \right\| = 133.9dB\Omega \quad \text{and} \quad \angle \frac{V_{P2H}(j\omega_{res})}{I_{mot}(j\omega_{res})} = -13.08^\circ$$

**Equation 28: Pickoff Channel Gain and Phase at  $\omega_{res}$**

The pick-off channel also determines the electrical noise performance of the interface. The TIA noise can be calculated as shown in Equation 29. The calculations predict an  $ENE\Omega$  of 2.2617  $^\circ/hr$  and an ARW of  $27.34 * 10^{-3} \text{ }^\circ/\sqrt{hr}$ . The electrical noise can be compared to the Brownian mechanical noise of the  $\mu HSR$ , which is shown to be 13.14  $^\circ/hr$  in Equation 30. Hence it is clear that the resolution (TNE $\Omega$ ) of 13.2  $^\circ/hr$  will be limited by the mechanical noise of the  $\mu HSR$  as shown in Equation 31 and the pickoff front-end contributes negligible noise to the rate output.

$$\begin{aligned}
\overline{I_{N-tot}}^2 &= \overline{i_{n-opamp}}^2 + \underbrace{\overline{v_{n-opamp}}^2 \left( \frac{1}{R_f} + \frac{1}{R_{in}} + \omega C_{TOT} \right)^2}_{\overline{i_{Nv-opamp}}^2} + \underbrace{\frac{4k_B T}{R_f}}_{\overline{I_{N-RF}}^2} + \underbrace{\frac{4k_B T}{R_{bias}}}_{\overline{I_{N-Rbias}}^2} \\
&= \overline{i_{n-opamp}}^2 + \overline{i_{Nv-opamp}}^2 + \overline{I_{N-RF}}^2 + \overline{I_{N-Rbias}}^2 \\
\overline{i_{Nv-opamp}}^2 &= \left( 5.1 \frac{nV}{\sqrt{Hz}} \right)^2 \left[ \frac{1}{500k\Omega} + \frac{1}{10^{13}\Omega} + 2\pi(6.711kHz)(8pF) \right]^2 \\
&= 1.421 * 10^{-28} \frac{A}{\sqrt{Hz}} \\
\overline{I_{N-RF}}^2 &= \frac{4(1.3806 * 10^{-23} \frac{m^2 kg}{s^2 k})(298.15k)}{500k\Omega} = 1.2931 * 10^{-26} \frac{A}{\sqrt{Hz}} \\
\overline{I_{N-Rbias}}^2 &= \frac{4(1.3806 * 10^{-23} \frac{m^2 kg}{s^2 k})(298.15k)}{100M\Omega} = 1.6466 * 10^{-28} \frac{A}{\sqrt{Hz}}
\end{aligned}$$

$$\begin{aligned}
\overline{I_{N-tot}} &= \left[ \underbrace{\left( 0.8 \frac{fA}{\sqrt{Hz}} \right)^2}_{6.4 * 10^{-31}} + 1.421 * 10^{-28} \frac{A}{\sqrt{Hz}} + 1.2931 * 10^{-26} \frac{A}{\sqrt{Hz}} \right. \\
&\quad \left. + 1.6466 * 10^{-28} \frac{A}{\sqrt{Hz}} \right]^{\frac{1}{2}} = 0.18231 \frac{pA}{\sqrt{Hz}}
\end{aligned}$$

$$ENE\Omega = \frac{\overline{I_{N-tot}} \sqrt{BW}}{Sensitivity} = \frac{\left( 0.18231 \frac{pA}{\sqrt{Hz}} \right) \sqrt{0.6Hz}}{400 \frac{pA}{\% / s}} \left( 3600 \frac{s}{hr} \right) = 1.271 \% / hr$$

$$ARW = \frac{\overline{I_{N-tot}}}{Sensitivity} * 60 = \frac{\left( 0.18231 \frac{pA}{\sqrt{Hz}} \right)}{400 \frac{pA}{\% / s}} 60 = 27.34 * 10^{-3} \% / \sqrt{hr}$$

**Equation 29: AFE pickoff channel noise calculation showing a predicted  $ENE\Omega = 1.27 \% / hr$  and ARW of  $27.34 * 10^{-3} \% / \sqrt{hr}$**

$$\begin{aligned}
MNE\Omega &= \frac{1}{2mA_g x} \sqrt{\frac{4k_B T_0}{\omega_0 M_{eff} Q}} \left(3600 \frac{s}{hr}\right) \left(\frac{180^\circ}{\pi}\right) \\
&= \frac{1}{2 * 2(0.3)(2\mu m)} \sqrt{\frac{4(1.381 * 10^{-23} \frac{m^2 kg}{s^2 k})(300k)}{(2\pi(6500Hz))(1.5775 * 10^{-9} kg)(11000)}} \left(3600 \frac{s}{hr}\right) \left(\frac{180^\circ}{\pi}\right) \\
&= 13.14 \text{ deg/hr}
\end{aligned}$$

**Equation 30: MNE $\Omega$  calculation showing MNE $\Omega$  = 13.14 °/hr**

$$TNE\Omega = \sqrt{MNE\Omega^2 + ENE\Omega^2} = \sqrt{(13.14 \text{ }^\circ/hr)^2 + (2.26 \text{ }^\circ/hr)^2} = 13.2 \text{ }^\circ/hr$$

**Equation 31: Resolution calculation showing TNE $\Omega$  = 13.2 °/hr**

### 2.3.2 Forcer Channels

The forcer channel consists of a buffer amplifier with a variable gain and optional passive low-pass filter at the input as shown in Figure 33. The gain is controlled using a potentiometer and is set to 0dB. The output of the buffer amplifier is then AC coupled into the forcer electrode. The design of the forcer channel was simulated and the frequency response of the design is shown in Figure 34. The gain is 0dB and the phase is 0° at the resonant frequency of 6.7 kHz

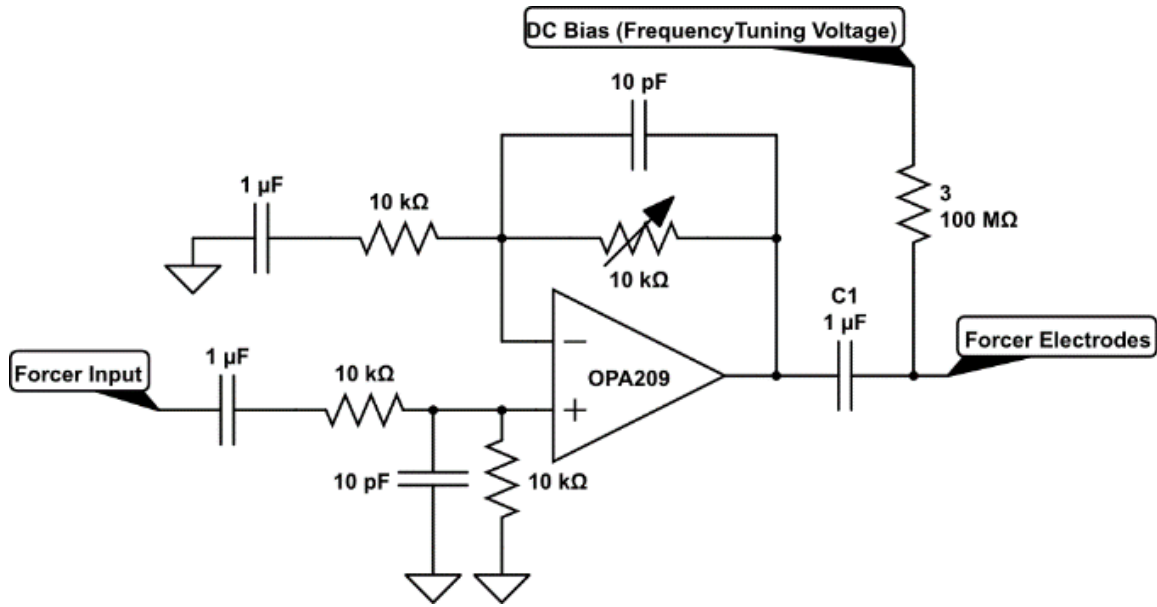


Figure 33: Forcer Channel Buffer Design

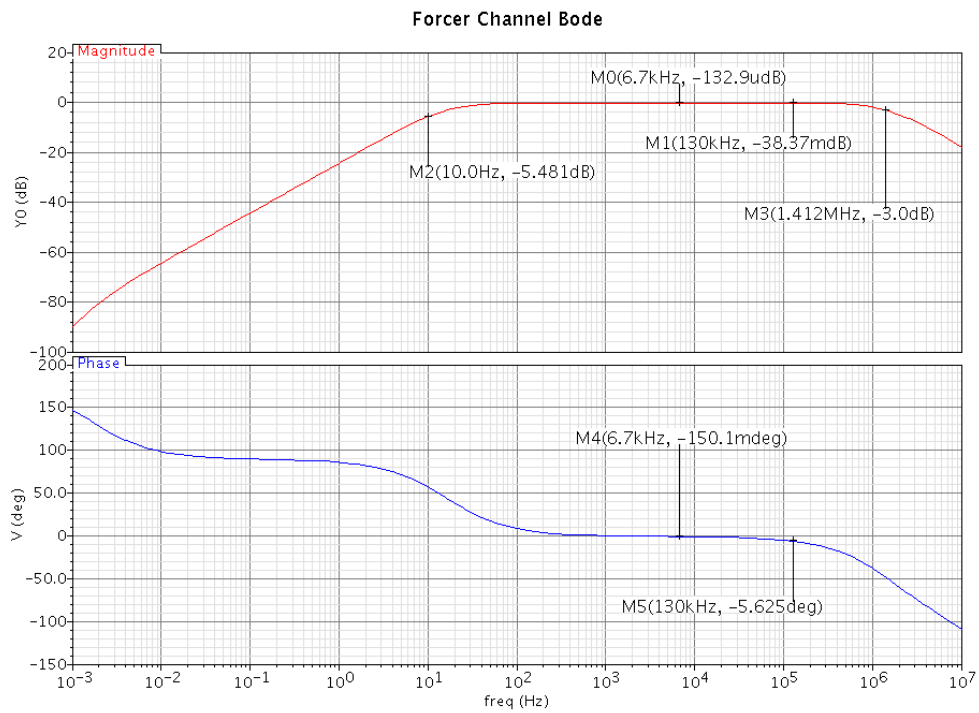
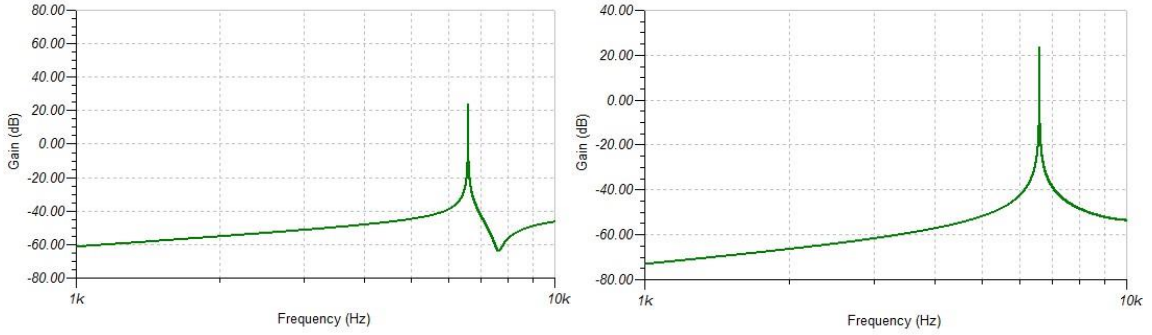


Figure 34: Forcer channel frequency response simulation

### 2.3.3 Feed-through Cancellation Channels

Feed-through is caused, as discussed in section 2.1.5, by capacitive coupling between the electrode bonding pads and the substrate. It can cause a large feed-forward

path across the resonator if not properly compensated. The feed-through not only causes the noise floor to rise but also induces an anti-resonance peak in the frequency response as shown in the simulation of Figure 35(a).



(a)

(b)

**Figure 35: Simulation of (a) frequency response with the feed-through cancellation mismatched by 10% (b) frequency response with feedthrough cancellation Perfectly Matched**

In order to compensate for the feed-through capacitance of the  $\mu$ HSR the feed-through cancellation circuit shown in Figure 36 was implemented. The circuit consists of an inverting voltage amplifier in series with a capacitor with a capacitance on the order of the feed-through capacitor. The gain of the amplifier is then tuned until the current through the feed-through cancellation capacitor is the same as that of the current through the feed-through capacitance but  $180^\circ$  out of phase so that the two currents cancel when mixed at the pickoff electrode as shown in Equation 32.

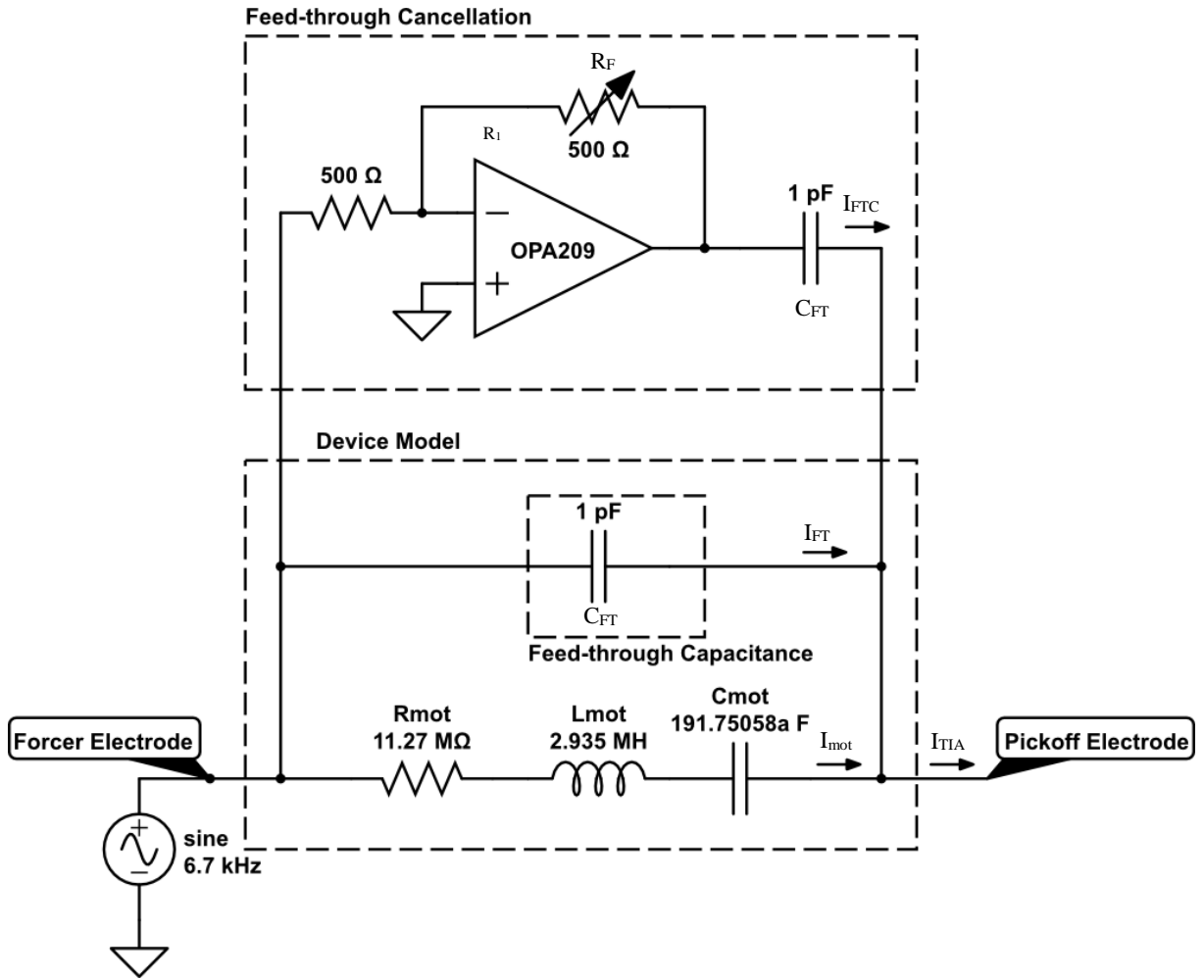


Figure 36: Feed-through cancellation Design

$$I_{TIA} = I_{mot} + I_{FT} + I_{FTC} = \frac{V_{Forcer}}{R_{mot}} + s(C_{FT} - \frac{R_F}{R_1} C_{FTC})V_{Forcer}$$

$$\frac{R_F}{R_1} = \frac{C_{FT}}{C_{FTC}} \rightarrow I_{TIA} = \frac{V_{Forcer}}{R_{mot}}$$

Equation 32: Feed-through cancellation Circuit Operating Principle

There are four instances of the feed-through cancellation circuit that cancel the feed-through from each drive channel to each sense channel. The current configuration only drives one of the two modes and hence only the feed-through cancellation circuits for that mode are required. The feed-through cancellation circuit from the drive forcer to the drive pick-off and from the drive forcer to the sense pick-off are both required. Both

feed-through cancellation circuits effect the feed-through levels at both the sense and drive pick-offs and must be tuned together to ensure the lowest feed-through level at both pick-offs.

### **2.3.4 Quadrature and Tuning Voltage Amplifiers**

The quadrature voltages are DC voltages applied to the  $\mu$ HSR in order to align the two  $m=2$  modes and reduce the quadrature component of the sense mode motional current. The tuning voltages are applied to the  $\mu$ HSR in order to tune the frequency of each mode. Both are used to match the two  $m=2$  modes through electrostatic spring softening as described in sections 1.4.4 and 1.4.5.

The two quadrature voltages are applied to the  $-22.5^\circ$  electrodes and  $+22.5^\circ$  electrodes so that each of the 2 voltages is applied to 4 electrodes that are separated by  $90^\circ$  around the circumference of the electrode configuration. These quadrature control voltages are also known as closed loop quadrature control voltages since they can be used to implement a control loop to control the quadrature output.

The amplifiers that generate the quadrature control voltages are configured to generate both voltages from a single input ranging from 0v to 3.3v. The amplifiers have a bipolar output of  $\pm 50$ v with  $V_{Q2}$ , also known as “Closed loop Quadrature +”, having a non-inverting output and  $V_{Q1}$ , also known as “Closed loop Quadrature -”, having an inverted output. This configuration can be easily reconfigured to accommodate a different input voltage range, a bipolar input, a differential input, or two separate single-ended input voltages.

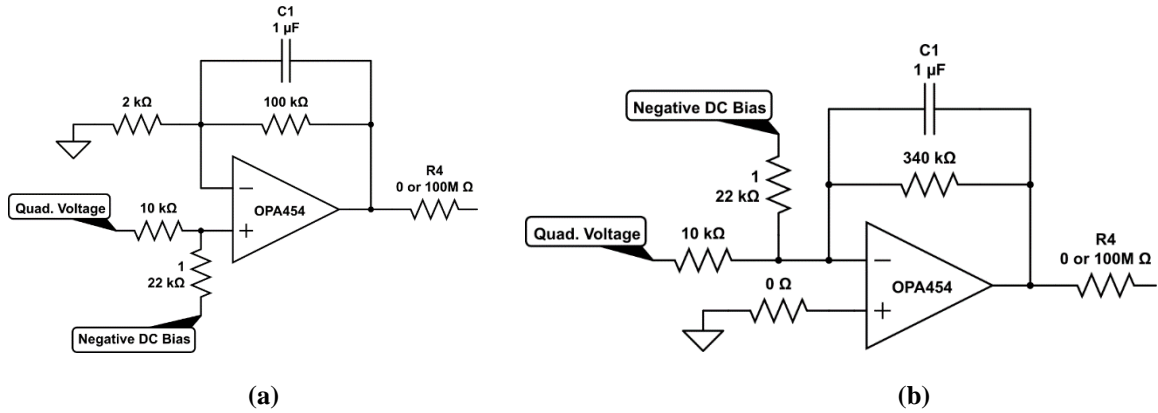


**Figure 37: Quadrature amplifiers (a) non-inverting configuration (b) Inverting Configuration**

The two tuning voltages are applied to the drive and sense mode electrodes. The first tuning voltage,  $V_{T1}$ , also known as “open loop quadrature +”, is applied to the drive electrodes also known as the “antinodal” electrodes since they are aligned with the antinodes of the drive mode in rate mode operation. The second tuning voltage,  $V_{T2}$ , also known as “open loop quadrature -”, is applied to the sense electrodes also known as the “nodal” electrodes since they align with the nodes of the drive mode.

The amplifiers for the tuning voltages are also designed to accommodate a single unipolar 0-3.3v input voltage to generate a differential bipolar output of  $\pm 50$ v. The amplifier for the first tuning voltage,  $V_{T1}$ , is a non-inverting configuration identical to the non-inverting amplifier used for the quadrature voltage while  $V_{T2}$  uses the same inverting configuration used for the quadrature voltages. However in order to prevent feed-through from the forcer electrode of each mode to the pickoff electrode of each mode, each tuning voltage has two instances of the same amplifier. One instance sets the DC bias on the forcer electrodes and the other instance sets the DC bias on the pick-off electrodes. Hence a total of 4 amplifiers are needed for the tuning voltages with half of them inverting and the other half non-inverting. The tuning voltages are coupled to the forcer and pickoff electrodes through a large (100M $\Omega$ ) resistor to set the DC bias without causing much attenuation of the forcer and pick-off signals. However, given that the

current corner frequency of the high pass filter is approximately 1.6 mHz, this resistance can be relaxed to reduce the settling time of the bias.

### 2.3.5 On-board Vacuum Chamber and Chassis

One of the largest sources of damping in a capacitively transduced resonator operated at atmospheric pressure is air damping. By reducing the operating pressure of the resonator, the air damping can be reduced to negligible levels. The effect of different chamber pressures on the quality factor of a  $\mu$ HSR is shown in Figure 38. The effects of air dampening become negligible at operating pressures below 1mTorr. Hence the device must be operated under high vacuum using a vacuum chamber and a turbo vacuum pump.

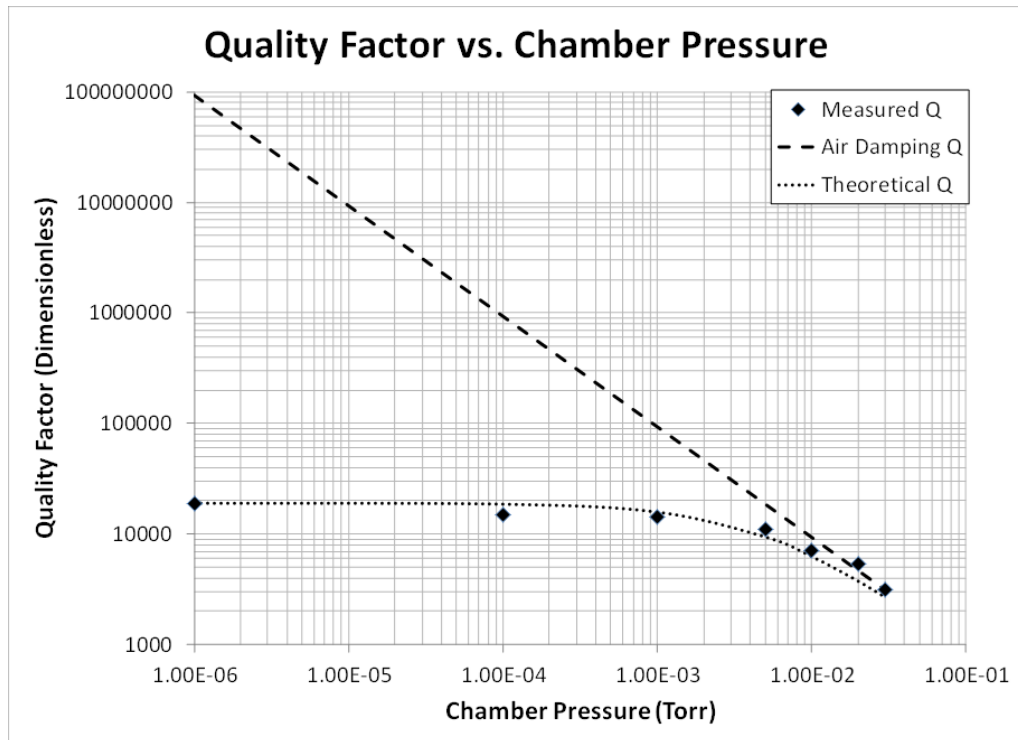
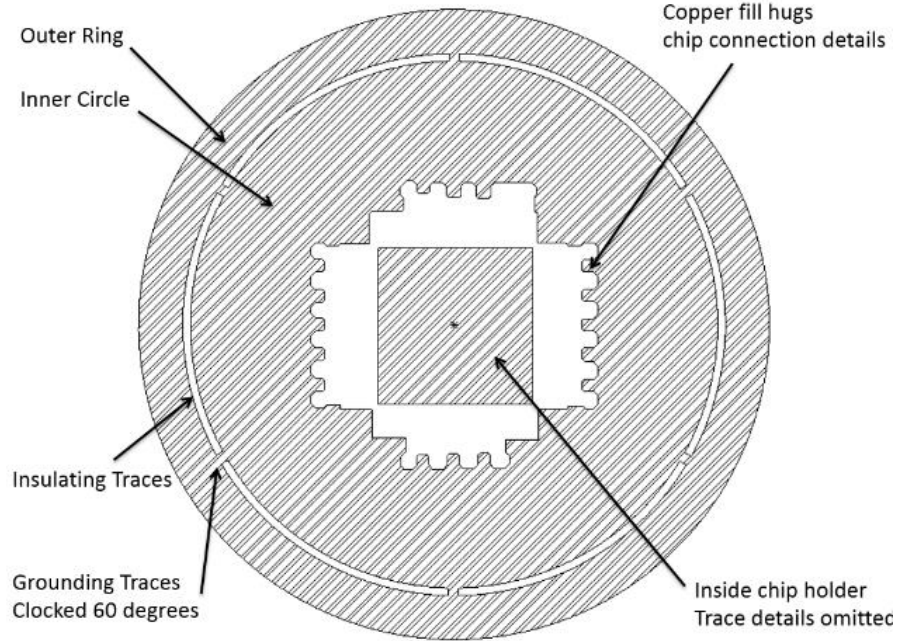


Figure 38: The effect of vacuum chamber pressure on quality factor

The analog front end is designed to accommodate an on-board vacuum chamber that encloses the device under test (DUT) and hold sub-mTorr pressure levels. A copper ring on the analog front end has been designed to mate with the on-board vacuum chamber as shown in Figure 39.



**Figure 39: Analog front-end copper ring to accommodate an on-board vacuum chamber**

The on-board vacuum chamber, shown in Figure 40, is a copper chamber designed to mate with the analog front-end's copper ring. The chamber has a ¼" copper pipe welded to it that mates with a vacuum pump through an Ultra-torr-316 adapter [69] and a vacuum pipe with a 40mm ISO-KF flange as shown on the left in Figure 40. The chamber is sealed using a gasket ring between the analog front-end and the chamber. The gasket and the chamber are held in place with a mounting bracket that attaches to the same mounting holes that attach the analog front-end to the chassis.

The chassis provides support for both the analog front-end and the vacuum chamber. The base is 5" by 8" to be compatible with the PALADIN evaluation system and is made from aluminum with #4-40 mounting holes for the board stand-offs and sides. The front side that provides mechanical support for the on-board vacuum chamber, is made from brass and has 6 sets of mounting holes spaced a ½" apart to adjust the height of the analog front-end and provide flexibility in the height of the interface boards mounted below the analog front-end.

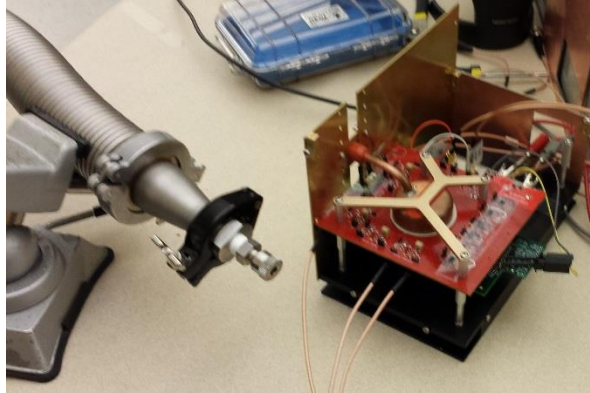


Figure 40: On-board vacuum chamber configuration

### 2.3.6 Analog Front-end Interfaces

The analog front-end interface consists of 2 40-pin male connectors with 0.5mil spacing attached to the bottom side of the board. The connector pin-out is given in Figure 41. The board is powered by  $\pm 8\text{v}$  supplies with decoupling capacitors on the board. The device also has power and ground connections for the high voltage power-supplies as shown in the schematic in Appendix B. **Error! Reference source not found.** The Polarization voltage input, labeled BIAS\_N200V in the schematic, has an RLC low pass filter implemented with through-hole components to filter out any noise.

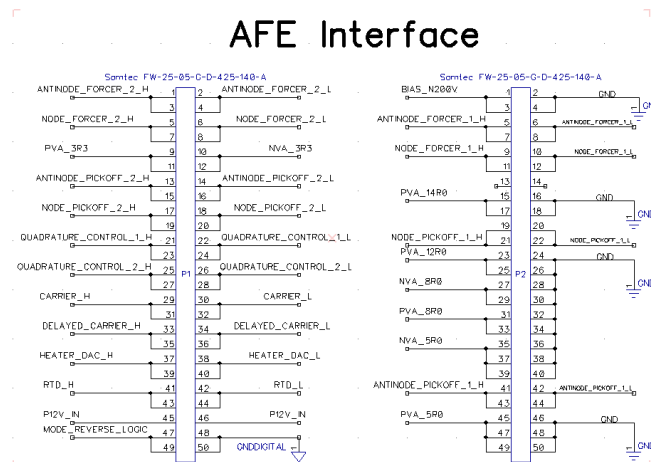


Figure 41: Analog front end interface pin-out

### 2.3.7 Analog Front-end Implementation

The analog front-end was implemented on a PCB using discrete components. The implementation is shown in Figure 42. A high-quality PCB with a larger than normal thickness was used to support the on-board vacuum chamber. The unpopulated section on the right of the board is for the high-voltage generators to be used for independent operation of the device during future demonstrations. DC power supplies were used in place of the high-voltage generators during initial testing.

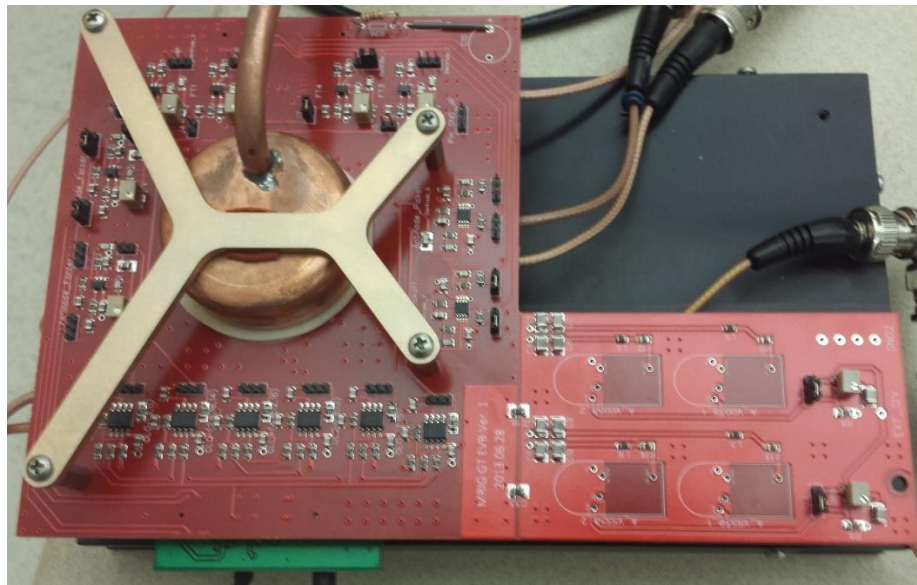


Figure 42: AFE implementation with attached adapter board for early  $\mu$ HSR testing

## 2.4 Closed Loop Analog Back End

### 2.4.1 System Design

The closed loop interface forms an oscillator around the drive loop in order to lock into the drive frequency of the device. This enables the drive signal to track the resonant frequency over variations caused by changes in temperature and other environmental variables. The closed loop interface also implements automatic level control to control the drive amplitude. The sense channel uses a traditional amplitude modulated (AM) readout architecture to generate the rate output.

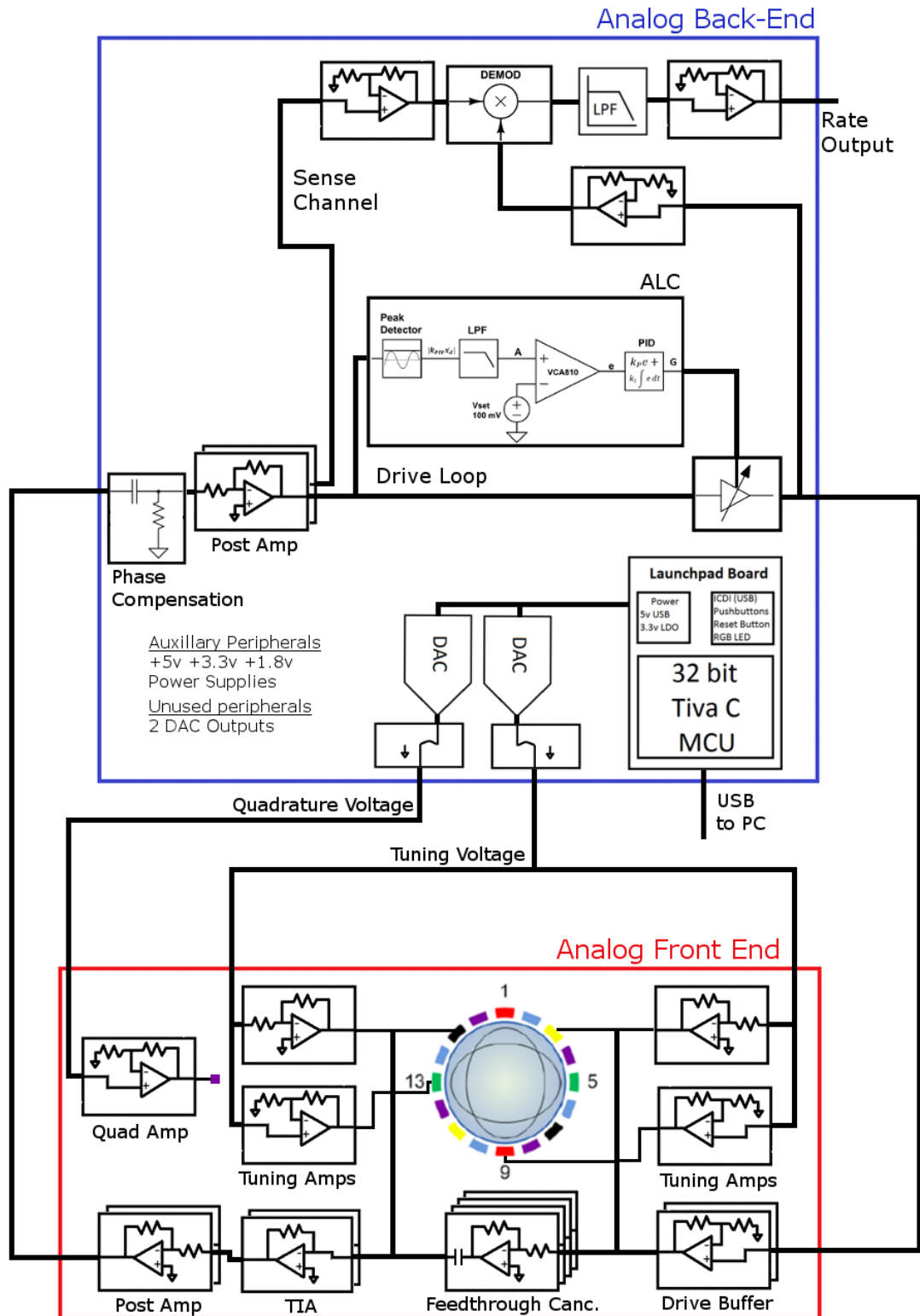


Figure 43: Analog Rate Interface Block Diagram

## 2.4.2 Drive Loop Design

### Drive Loop Post-amplifiers

In order to increase the gain through the drive loop, two post-amplifiers were added to supplement the gain from the single post-amp on the analog front end. The first post-amp includes the option to form a phase shifter that can be used to compensate for phase shift added by any of the low-pass filters in the drive loop. The second post amp includes the option to change the phase through the drive channel to either  $0^\circ$  or  $180^\circ$ . The design of the post-amp is shown in Figure 44. The ADA4898 was selected for its low-noise and wide-bandwidth with the specifications shown in Table 6.

The Drive loop also contains a voltage control amplifier and attenuator, the VCA810. The VCA810 [70] has a gain control voltage,  $V_c$  that is linear in dB from -40dB at 0v to +40dB at -2v. The gain in the post-amp is selected so that in steady-state the control voltage is biased at -0.35v for an attenuation of 26dB. This bias point was selected so that the voltage being sampled by the ALC has a large enough amplitude ( $V_{REG} \approx 100\text{mV}$ ) while also keeping plenty of margin for the ALC to adjust the gain in the drive loop. A benefit of biasing the control voltage at -0.35v is that the gain error of the VCA810 is minimized at around -0.35 dB as shown in the typical gain error plot given in Figure 45.

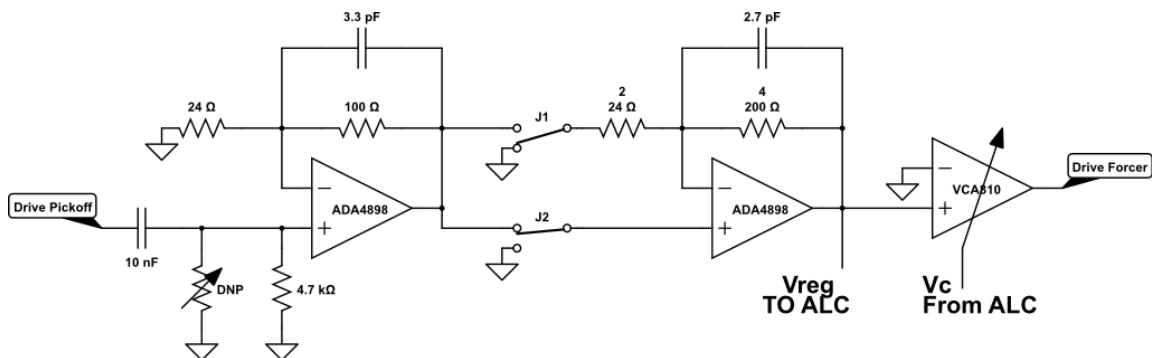
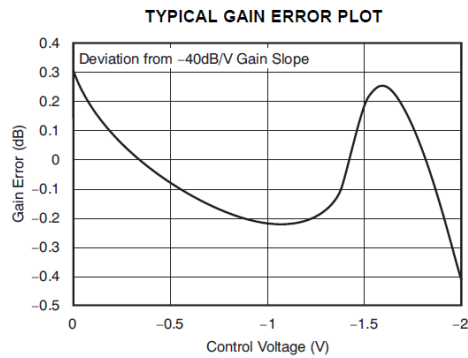


Figure 44: Second drive post-amp with optional phase shifter

**Table 6: ADA4898 Key Specifications**

<b>ADA4898</b>	
<b>GBW</b>	65 MHz
<b>Input Bias Current</b>	0.1 $\mu$ A
<b>Voltage Noise</b>	0.9 nV/ $\sqrt$ Hz
<b>Quiescent Current</b>	8.0 mA/ch



**Figure 45: VCA810 typical Gain Error Plot**

The oscillator loop was simulated at the nominal  $V_c$  bias point of -0.35v. The frequency response of the post-amplifiers (red) and the total response including a macromodel of the VCA810 (green) was simulated in Spice and is shown in Figure 46. The total gain and phase response at the resonant frequency is given in Equation 33.

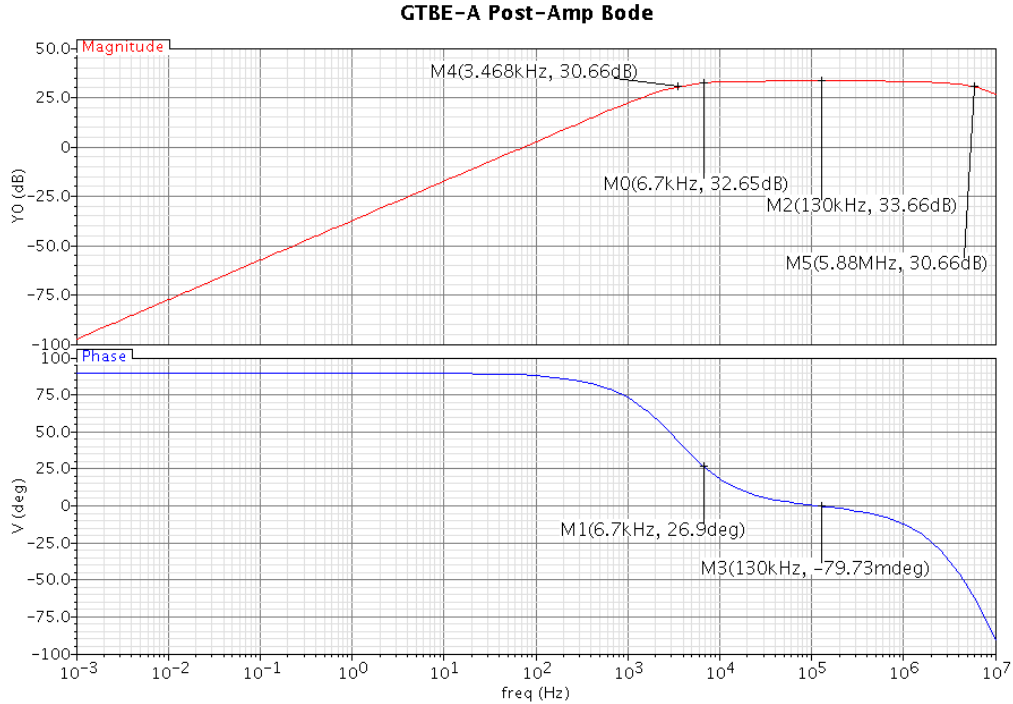


**Figure 46: Simulated post-amp frequency response**

$$\left\| \frac{V_F(j\omega_{res})}{V_{P2H}(j\omega_{res})} \right\| = 13dB \quad \text{and} \quad \angle \frac{V_F(j\omega_{res})}{V_{P2H}(j\omega_{res})} = 26.7^\circ$$

**Equation 33: Simulated post-amp gain and phase at the resonant frequency of 6.7kHz**

## Drive loop feed-through filters

The feed-through cancellation circuit on the AFE does a good job of cancelling the feed-through of the device close to the resonant frequency of the  $\mu$ HSR. However at slightly higher frequencies the feed-through level starts to increase significantly due to a feed-through phase response that isn't flat over frequency. If these frequencies are not attenuated, the feed-through levels can actually increase the loop gain at these frequencies above 0dB and cause the device to oscillate at a frequency far from the 6.7 kHz resonant frequency of the device. In order to avoid this problem, a second order Sallen-Key low pass filter was added with a corner frequency at 28.625 kHz. The design of this filter is shown in Figure 47.

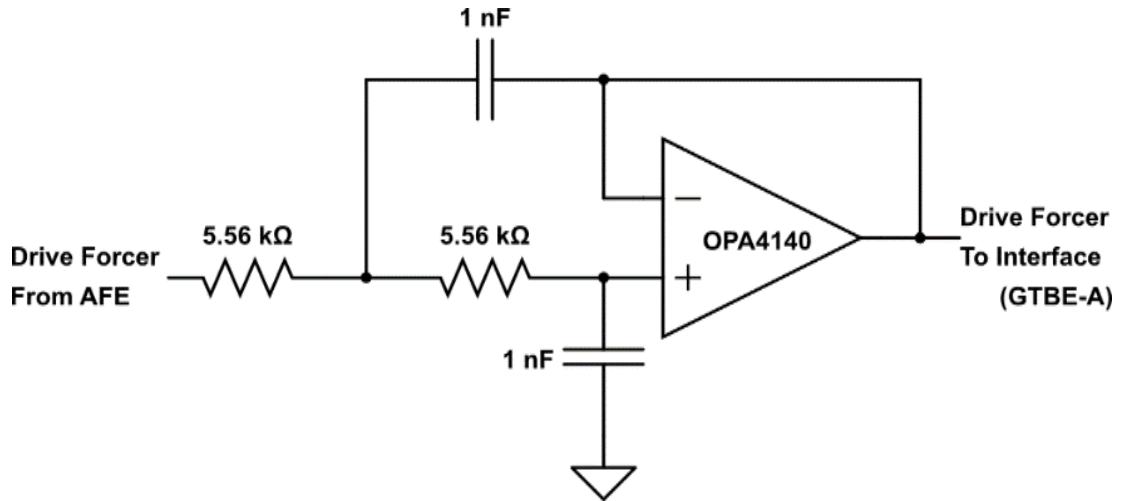


**Figure 47: Drive loop feed-through filter design**

The simulation results for the filter design shown in Figure 48 give a phase shift of  $-26.65^\circ$  and a magnitude of  $-0.48$  dB.

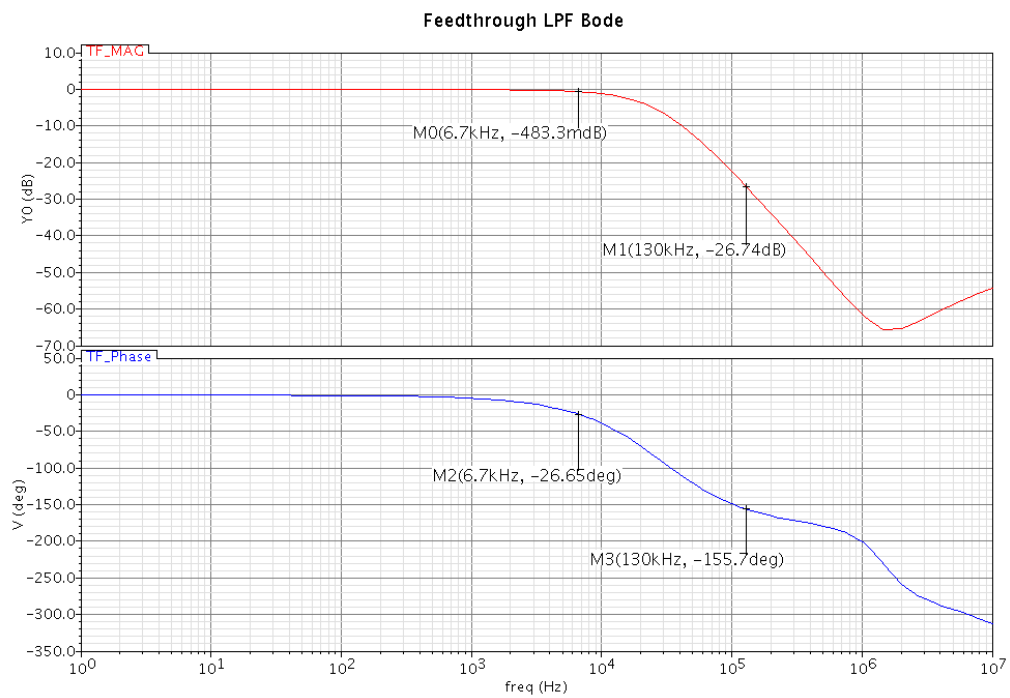


**Figure 48: Gain and Phase of Feed-through LPF Simulation**

## Oscillator Loop

In order for the drive loop to oscillate the gain and phase around the loop must meet the necessary Barkhausen criteria [71] as given in Equation 34. In order for an oscillation to be sustained the gain of the loop transfer function must be 1 and the phase around the loop must be  $360^\circ$ . As shown in Figure 49, the expected gain and phase around the loop meets this criteria.

$$\|Loop\ Gain\| = 1 \quad \text{and} \quad \angle Loop\ Gain = 360^\circ$$

Equation 34: Barkhausen Criteria for oscillation

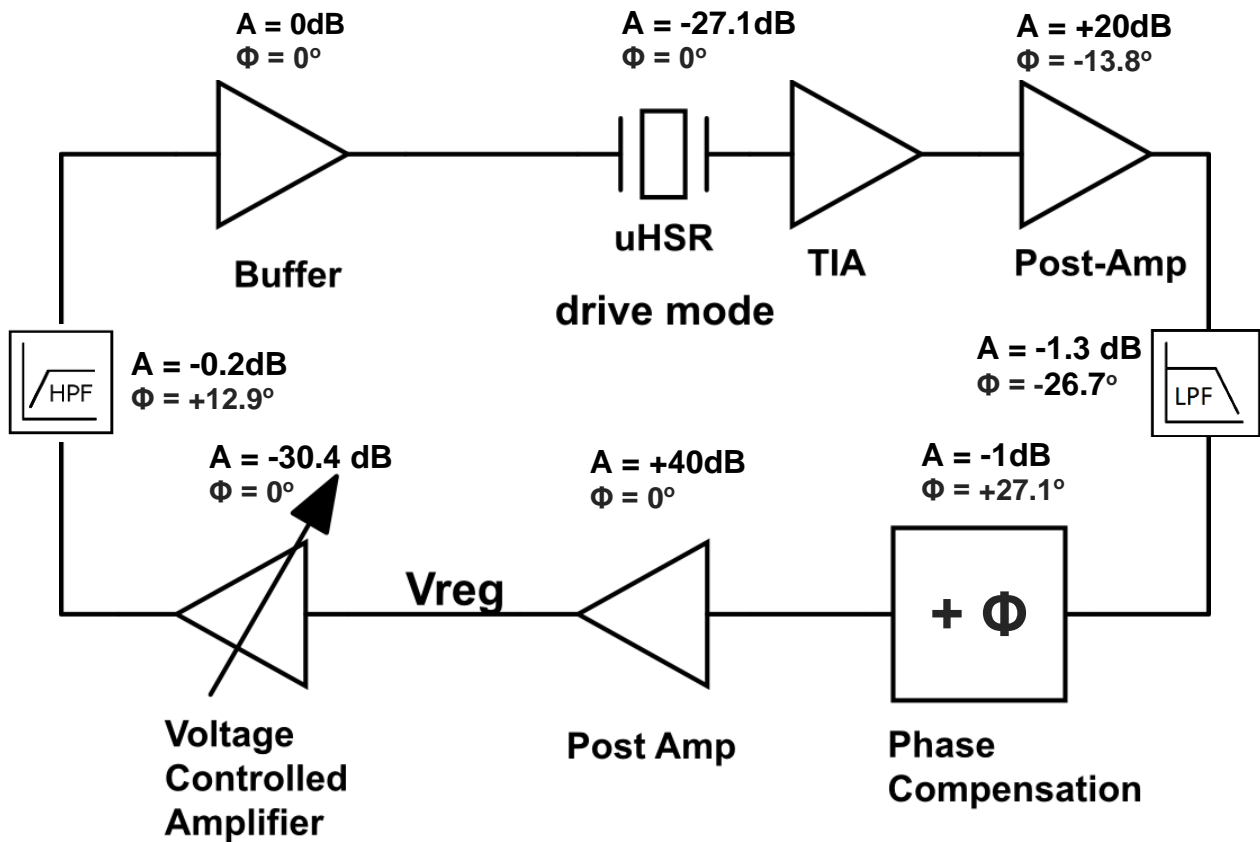
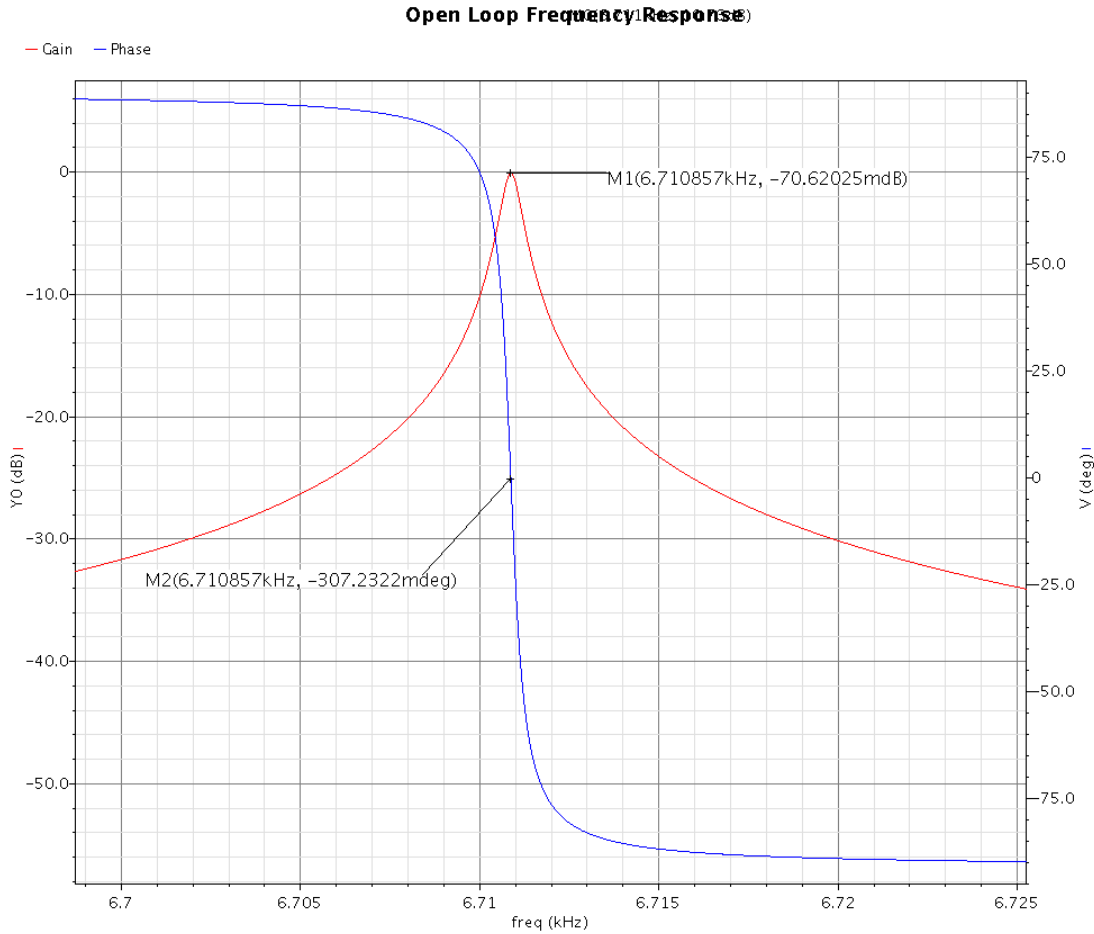


Figure 49: Expected drive loop gain and phase at  $f_{res} = 6.7\text{kHz}$

In order to insure the loop gain and phase were correct an open-loop simulation of the complete drive loop was performed. The ALC loop was first opened and the control of the voltage controlled amplifier was set to  $-230\text{mV}$  to make the loop gain  $0\text{dB}$ . The

loop was then opened at the input of the analog back-end, right before the phase compensation. The frequency response of the open-loop response, shown in Figure 50, confirms that the Barkhausen criteria are met for the drive oscillator.



**Figure 50: Open-loop frequency response**

### 2.4.3 Automatic Level Control Design

The automatic Level control consists of a peak detector that samples the amplitude of the drive signal at  $V_{reg}$ . A difference amplifier with a variable gain is then used to generate an error signal by taking the difference between the amplitude of  $V_{reg}$  and the amplitude set point. The error signal is then amplified by a PI controller and level shifted by -1v to match the -2v to 0v control voltage range of the voltage controlled amplifier in the drive loop. The complete drive loop with the automatic level control was

simulated to estimate the correct PI gains and to get a measure of the stability of the ALC control loop. The complete design of the ALC is shown in Figure 51

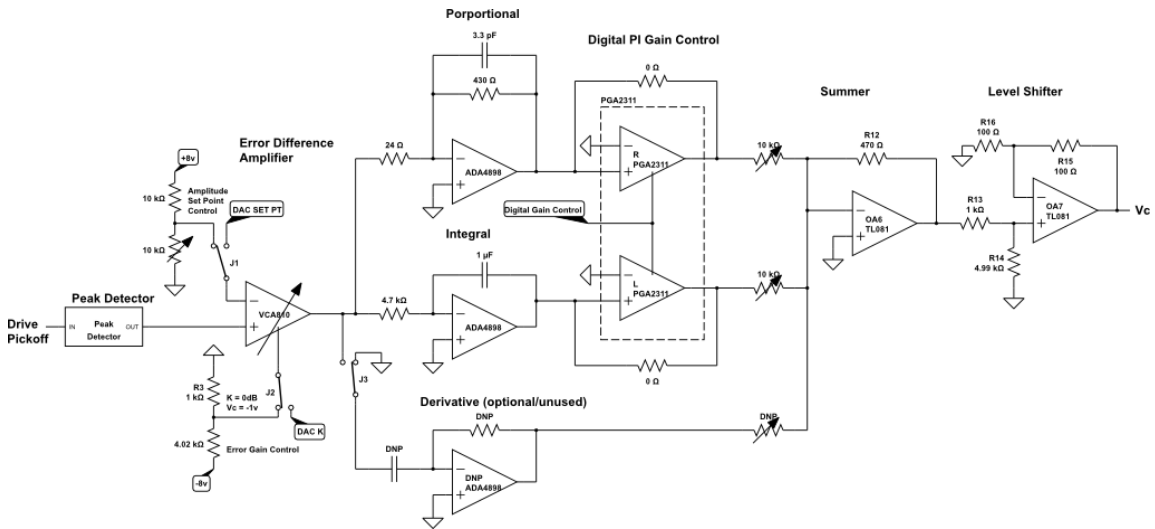


**Figure 51: Automatic Level Control (ALC) Design**

### ***Peak Detector***

The peak detector was designed to be flexible in its configuration with the three possible configurations shown in Figure 52. The first design in Figure 52 (a) is the most basic precision peak detector which was used in this work. The second and third designs reduce the leakage from the  $V_{peak}$  node. The peak detector has a time constant at the  $V_{peak}$  node and then a filter to filter out ripple due to the drooping between peaks. The output of the peak detector is connected to the positive input of a VCA810 variable gain amplifier being used as the error amplifier. The input of the VCA810 must be driven by a low impedance source, hence the resistor on the output filter is chosen to be as small as possible.

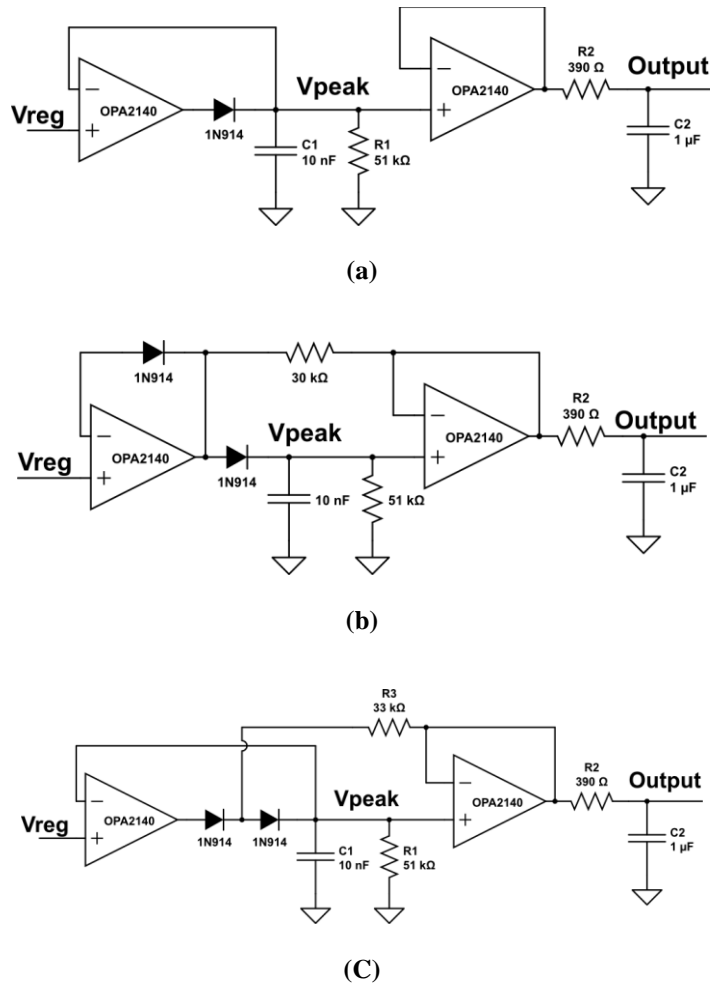


**Figure 52: Possible configurations of the flexible peak detector design. (a) Basic peak detector used in this design, (b) and (c) reduce the leakage from the Vpeak node which is useful for long time constants**

The transient characteristics of the peak detector were simulated to demonstrate the functionality of the design. All configurations were shown to be functional in simulation, however only the configuration in Figure 52a, the configuration used for testing will be presented. The simulated transient response of that design, shown in Figure 53, verifies the functionality of the design.

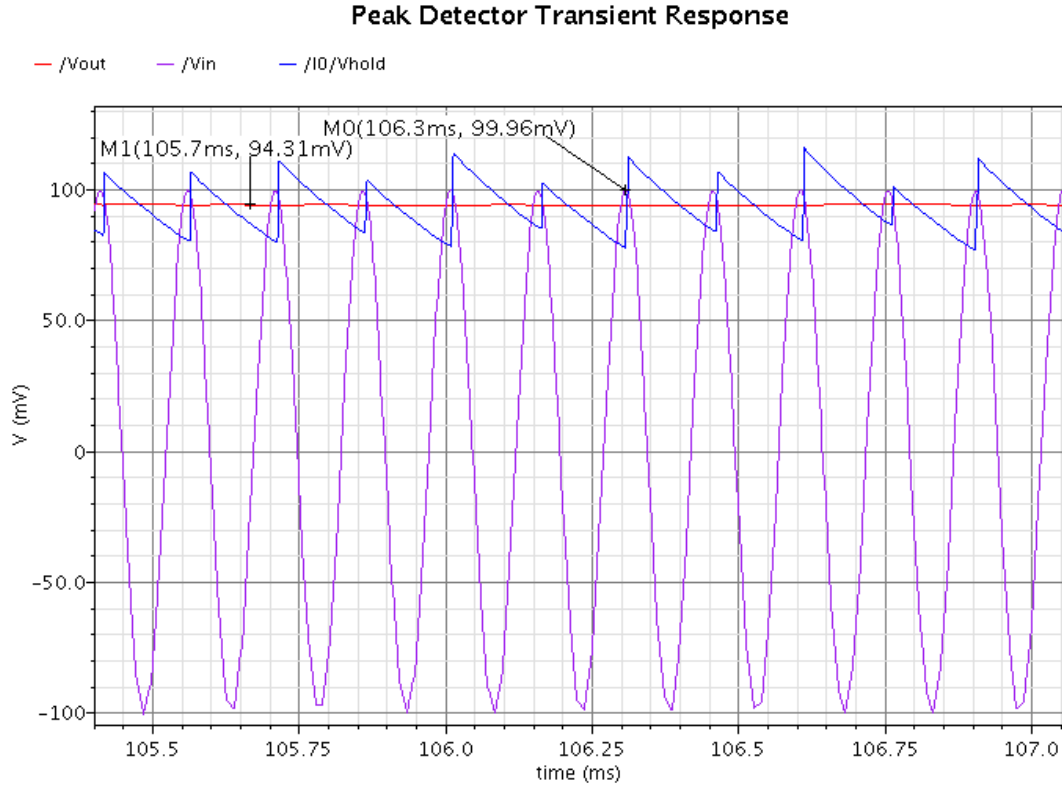


**Figure 53: Peak detector transient simulation showing the input waveform in purple, the holding capacitor voltage with ripple in blue and the smoothed output after the LPF.**

### ***PI Controller***

The PI controller consists of an amplifier, an integrator, and an optional differentiator. The three gains are then summed using a summer with potentiometers for tuning each of them. The differentiator was included for flexibility. As shown in Equation 16, the ALC is stable if  $\lambda k_p > k_I$ . Hence, referring to the Figure 51, we have  $k_I$  and  $k_p$  as given in Equation 35 and the ALC stability criteria as given in Equation 36.

$$k_I = \left( \frac{1}{R_I C_I} \right) \left( \frac{R_{FS}}{R_{IP}} \right) = \frac{100k \text{ rad}}{R_{IP} \text{ s}} \quad k_p = \left( \frac{R_{FP}}{R_{Pin}} \right) \left( \frac{R_{FS}}{R_{PP}} \right) = \frac{4.7k}{R_{PP}}$$

$$\lambda = \frac{1}{R_{LPF} C_{LPF}} = \frac{1}{(386\Omega)(1\mu F)} \frac{\text{rad}}{\text{s}} = 551.2 \frac{\text{rad}}{\text{s}}$$

**Equation 35: PI controller gains**

$$\lambda k_P > k_I \rightarrow \frac{259.07k\Omega}{R_{PP}} > \frac{100k\Omega}{R_{IP}}$$

**Equation 36: ALC stability criteria**

### ***Level Shift***

A basic level shifter, shown in Figure 54, was implemented to shift the control voltage by -1v to the center of the -2v to 0v input range of the voltage controlled amplifier. It uses a voltage divider followed by an amplifier to compensate for the attenuation.

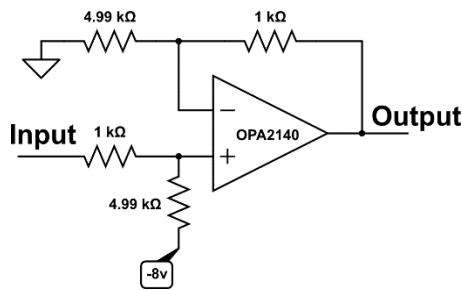


**Figure 54: ALC level shifter**

### ***Drive Loop and Automatic Level Control Simulation***

The ALC was simulated with the resonator drive mode modeled by the RLC model derived in section 2.2.6. The schematic of the test bench is shown in Figure 55. Transient simulations of the device were ran to verify the design of the drive loop oscillator with the drive forcer node shown in light blue. The gains of the drive loop and the steady state bias of the voltage controlled amplifier were later adjusted to reduce the drive forcer voltage to around 5 mV in order to keep the device operating linearly as shown during device characterization. A step response was then applied in a transient simulation to test the stability of the ALC and, as shown in Figure 57, the drive forcer's amplitude in light blue shows a correctly damped transition in the amplitude after the step input.

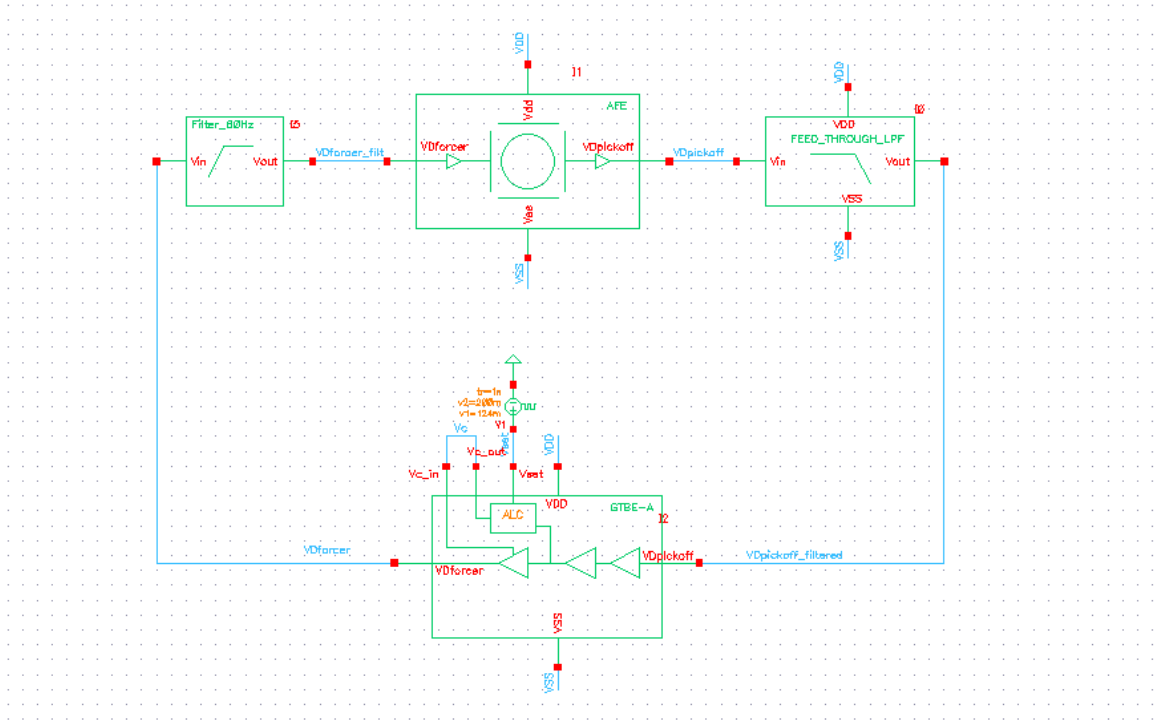


**Figure 55: Automatic Level Control and Drive loop oscillator simulation Test Bench**

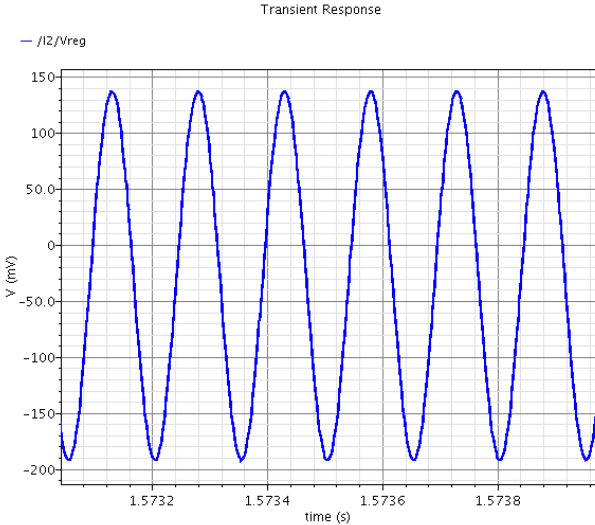


**Figure 56: Transient Simulation to verify the design of the drive loop oscillator. The light blue signal is the drive forcer signal.**

## Vreg Step Response Simulation

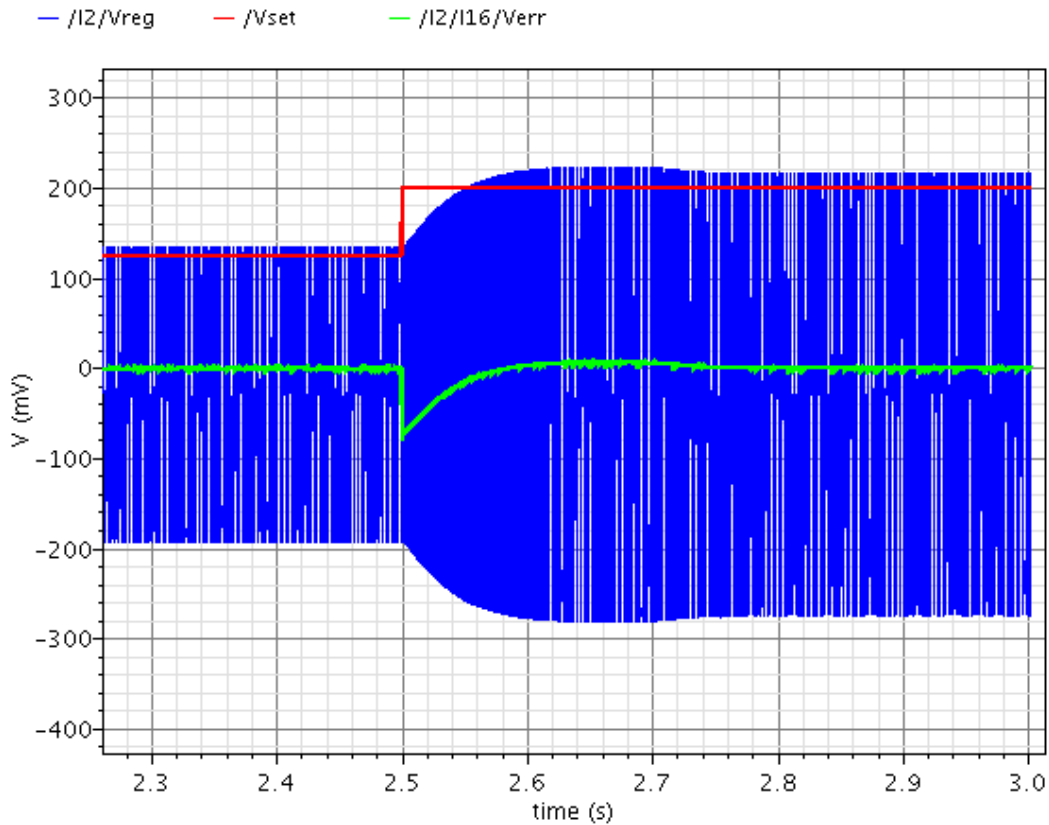


**Figure 57:** Transient simulation showing the step response of the ALC as the set point, the red step signal, was stepped from the normal operating point of 124mV to 200mV. The blue signal is the regulated drive voltage, VREG. The green signal is the ALC error voltage.

### 2.4.4 Sense Channel Design

The sense channel generates a voltage linearly proportional to the rate of rotation of the  $\mu$ HRG. The sense pickoff voltage has two main components. The first is the amplitude modulated rate output signal that is ideally in phase with the drive forcer voltage. The second is the quadrature component that is generated due to anisotropic fabrication imperfections in the  $\mu$ HSR.

The sense channel design, shown in Figure 58, demodulates the rate output using an analog multiplier. The drive forcer and sense pickoff signals are both amplified to appropriate signal levels ( $\sim 1$ v) for the analog multiplier. The output of the multiplier is

then passed through a low-pass filter to separate the rate output signal down at baseband from the component of the multiplier at twice the frequency of the carrier.

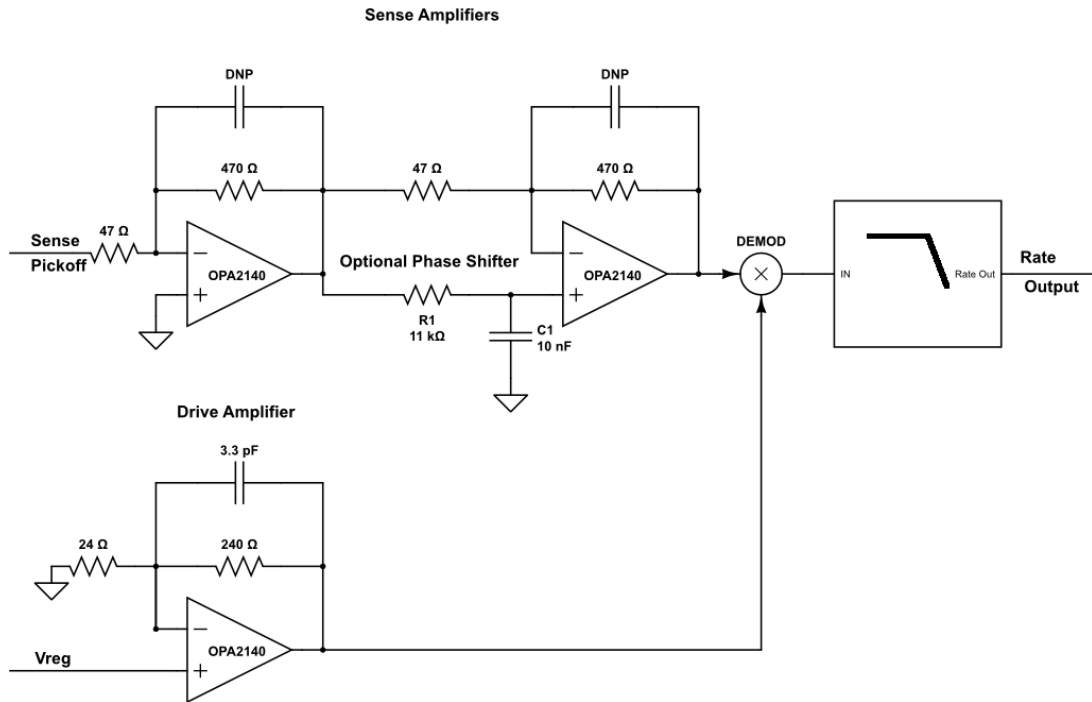


Figure 58: Sense channel design

### Sense Channel Scale Factor Estimation

Finite element analysis (FEA) simulations have been used to estimate the sensitivity of the  $\mu\text{HSR}$ , giving  $400\text{pA}/^\circ/\text{s}$  at a shell polarization voltage of  $40\text{v}$ , a drive voltage of  $30\text{mV}$ , a quality factor of  $10\text{k}$ , and utilizing a single sense and a single drive electrode. [50] However to make a fair comparison with the measured results presented in Chapter 3, the sensitivity must be scaled to account for the difference in the bias conditions, the measured quality factor and the number of electrodes used for the drive forcer and the sense pick-off. Hence, by scaling the sensitivity as shown in Equation 37, a scale factor estimate of  $4.96\text{pA}/^\circ/\text{s}$  is calculated.

$$\begin{aligned}
S_{sim\ scaled} &= S_{sim} \left( \frac{Q_{s,test}}{Q_{s,sim}} \right) \left( \frac{N_{d,test}}{N_{d,sim}} \right) \left( \frac{N_{s,test}}{N_{s,sim}} \right) \left( \frac{V_{ps,test}}{V_{ps,sim}} \right) \left( \frac{V_{pd,test}}{V_{pd,sim}} \right) \left( \frac{V_{d,test}}{V_{d,sim}} \right) \\
&= \left( 400 \frac{pA}{\circ/S} \right) \left( \frac{8.5k}{10k} \right) \left( \frac{2}{1} \right) \left( \frac{2}{1} \right) \left( \frac{14v + 3.5v}{40v} \right) \left( \frac{14v - 12v}{40v} \right) \left( \frac{5mv}{30mv} \right) \\
S_{sim\ scaled} &= 4.96 \frac{pA}{\circ/S}
\end{aligned}$$

**Equation 37: Scaled Sensitivity estimate**

The sense channel gain from the sense pickoff to the rate output is  $7G\Omega$  as shown in Equation 38. The estimated scale factor of  $34.7mV/\circ/s$  is then calculated as shown in

$$A_{sense} = A_{R,TIA} A_{PA1} A_{\phi-shift} A_{PA2} A_{rate} * V_{drive} = (500k\Omega)(10)^4(1.4) = 7G\Omega$$

**Equation 38: Sense channel gain**

$$SF_{est} = A_{sense} S_{sim\ scaled} = 7G\Omega * 4.96 \frac{pA}{\circ/S} = 34.7mV/\circ/s$$

**Equation 39: Scale factor estimate**

## Sense Channel Drive Amplifier

The gain of the sense channel amplifier is set so that the amplitude of the drive voltage is approximately 1v peak going into the analog multiplier, which is close to the maximum input swing it can accept. Its phase shift is minimized as you can see in the simulated frequency response shown in Figure 59.

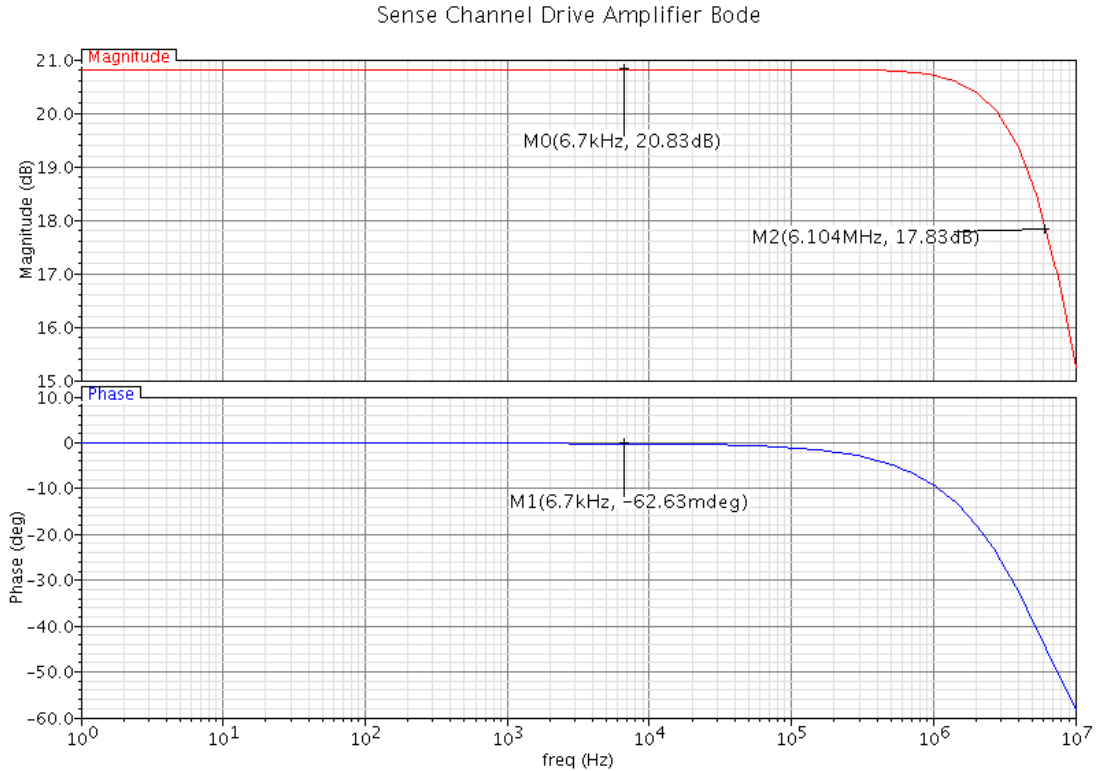


**Figure 59: Frequency response of the sense channel drive amplifier**

## Sense Pickoff Post-amplifier and Phase Shifter

Similar to the gain of the sense channel drive amplifier the gain of the sense pickoff post-amplifier is also set to give approximately 1v peak at the input of the analog multiplier. The phase response of the pickoff amplifier is set so that the phase shifter compensates for the  $-13.08^\circ$  of phase shift introduced by the pickoff channel on the AFE. The phase shift is introduced using the phase shifter. The frequency response of the pickoff amplifier is shown in Figure 60.

$$\frac{V_o(s)}{V_i(s)} = \frac{\left(1 - s \frac{R_F}{R_I}\right)}{1 + sRC} = -\frac{R_F}{R_I} \frac{\left(s - \frac{R_I}{R_F} \frac{1}{RC}\right)}{\left(s - \left(-\frac{1}{RC}\right)\right)}$$

**Equation 40:Phase shifter transfer function**

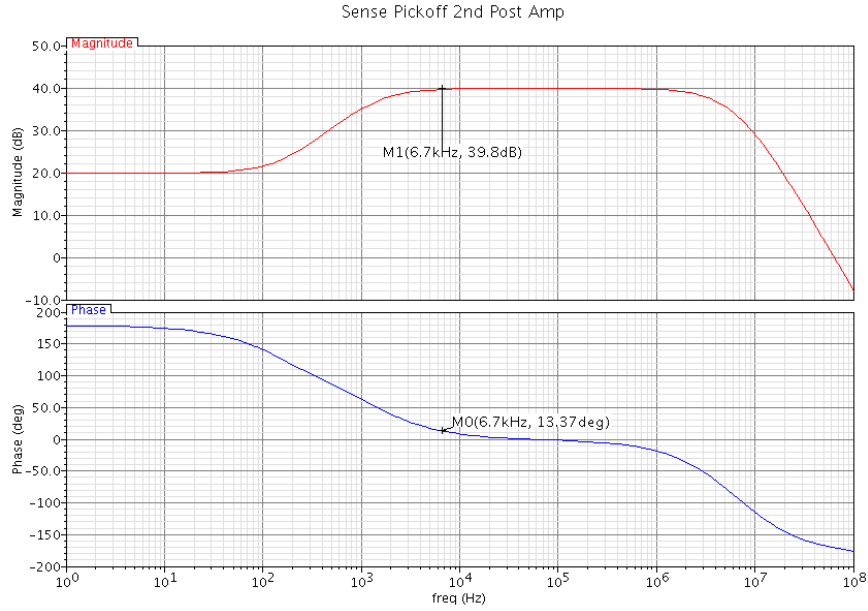


**Figure 60: Frequency response of the sense pickoff amplifier with phase compensation**

## Demodulator

The AD835 [72] was used as the analog multiplier to demodulate the sense pickoff with respect to the drive forcer voltage. The AD835 was selected due to its high multiplication accuracy and stable operation. The configuration of the multiplier is shown in Figure 61. The gain of the multiplier was set to 1 using the external resistor network as detailed in Equation 41.

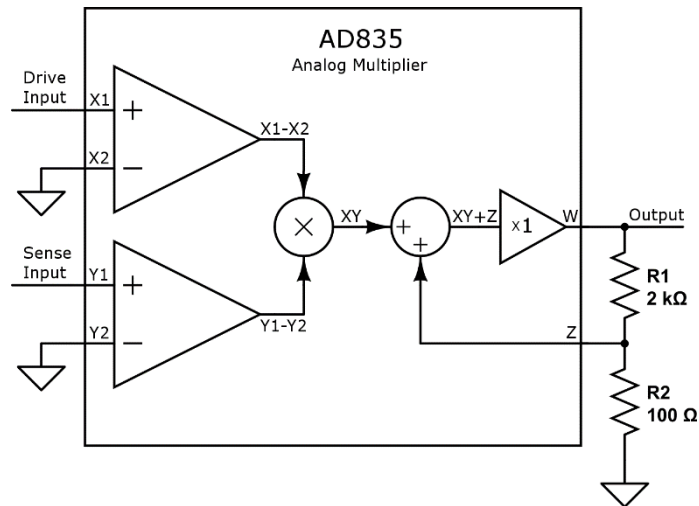


**Figure 61: AD835 analog multiplier configuration**

$$W = \frac{XY}{1.05} + Z = \frac{XY}{1.05 \left(1 + \frac{R_2}{R_1}\right)} = XY$$

Equation 41: Demodulator Transfer Function

## Low-pass Filter and Rate Amplifier

A low-pass filter is used to filter the component at twice the frequency of the carrier in order to extract the baseband rate signal. The filter is a 2<sup>nd</sup>-order Sallen-Key filter with a cutoff frequency of 1Hz, well above the 0.8Hz bandwidth of the device. After the low-pass filter a gain stage of 20dB is then used to amplify the rate output voltage. The design of the filter and rate amplifier is shown in Figure 62. Its frequency response is shown in Figure 63.

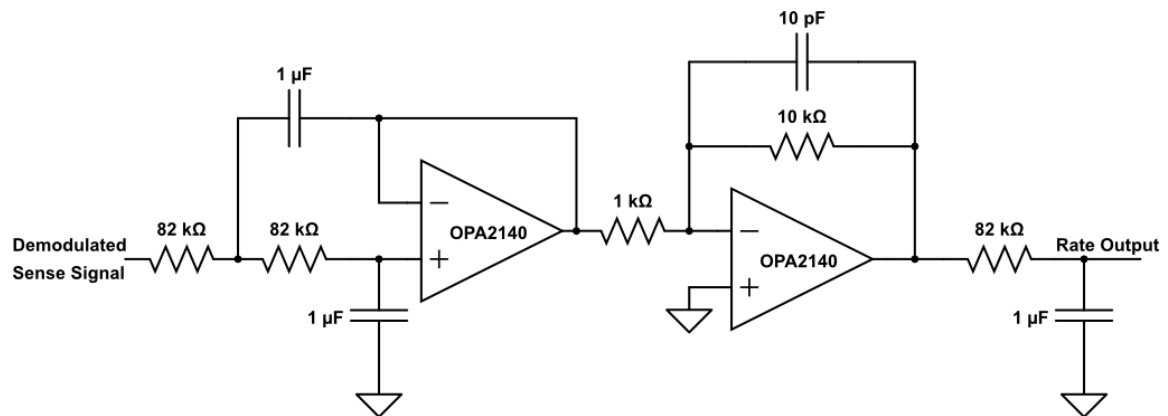


Figure 62: Sense channel 2nd order LPF

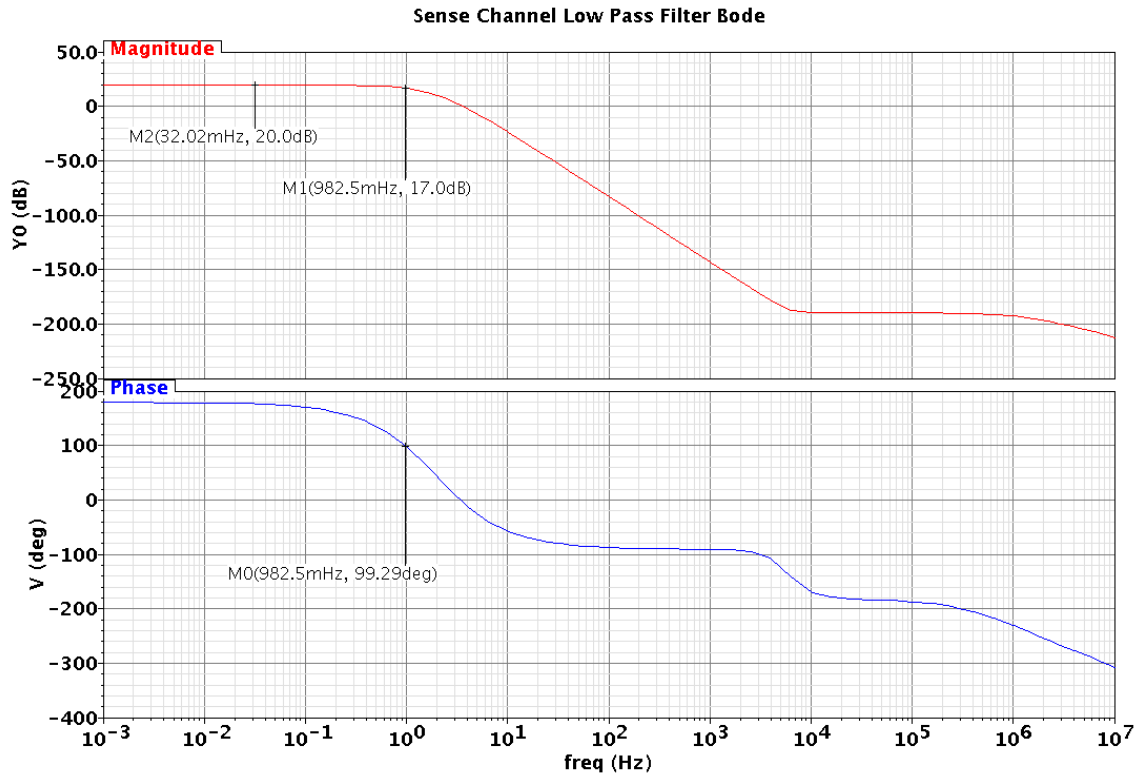


Figure 63: Frequency response of the sense channel low pass filter

## Sense Channel Simulation

The sense channel was simulated by using a Verilog-A model for the demodulator. The model was used to confirm that the multiplicands of the demodulator,  $V_{REG}$  and the amplified sense pick-off, were in phase and have a maximum amplitude of 1.5V, the maximum input voltage of the AD835, as shown in Figure 64.

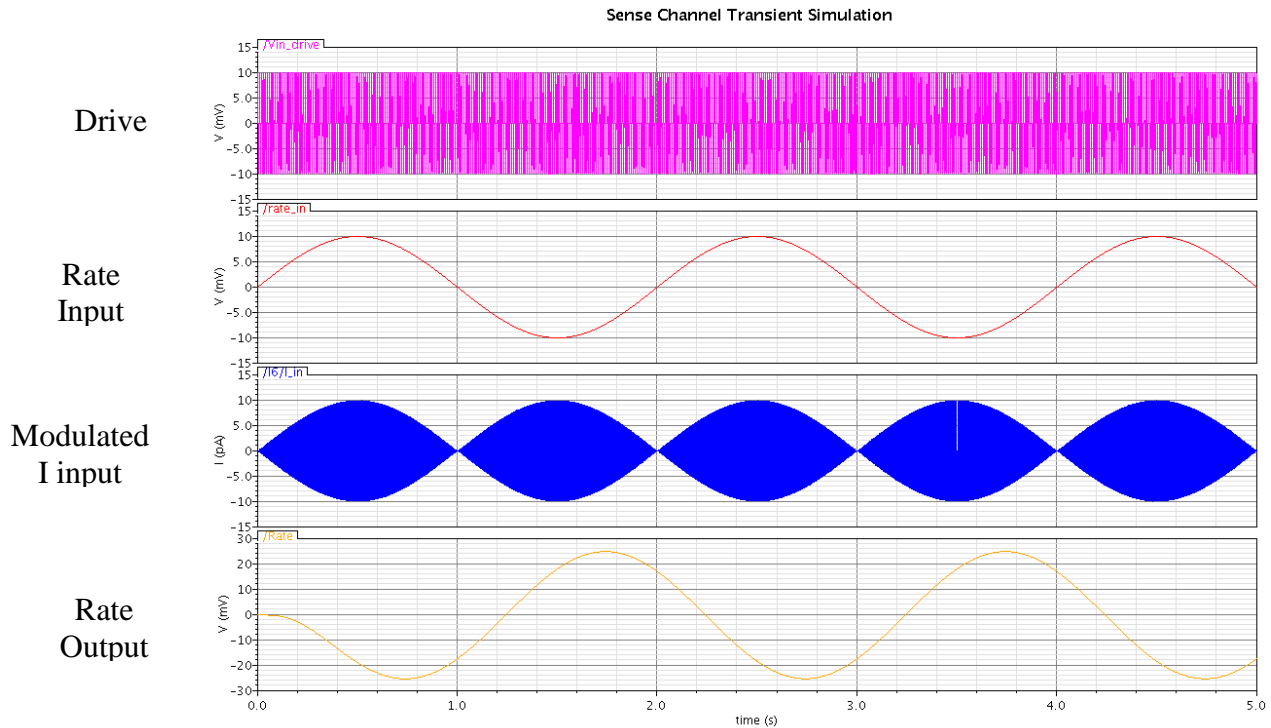


Figure 64: Sense Channel Transient Simulation

## 2.4.5 Digital ALC, Quadrature and Frequency Tuning System

The back-end contains 8 digital to analog converter (DAC) output voltages. Four outputs are used to apply each of the quadrature and frequency tuning voltages that match the modes. Two outputs are used to tune the ALC with one to control the amplitude set point of  $V_{REG}$  and the other to set the difference amplifier gain. The last two outputs remain unused and are attached to test points. The digital control system also includes the option of controlling the ALC PI gains digitally using a digitally controlled amplifier.

The eight DAC outputs are implemented using two 4 channel 16-bit AD5754 [73] DACs from Analog Devices. The two DACs are daisy chained and controlled by a single serial peripheral interface (SPI) connection. They are operated as bipolar  $\pm 8\text{v}$  outputs. A Texas Instruments PGA2311 [74] was used as a digitally controlled amplifier for controlling the ALC PI gains.



## Chapter 3

### Gyroscope Performance Characterization

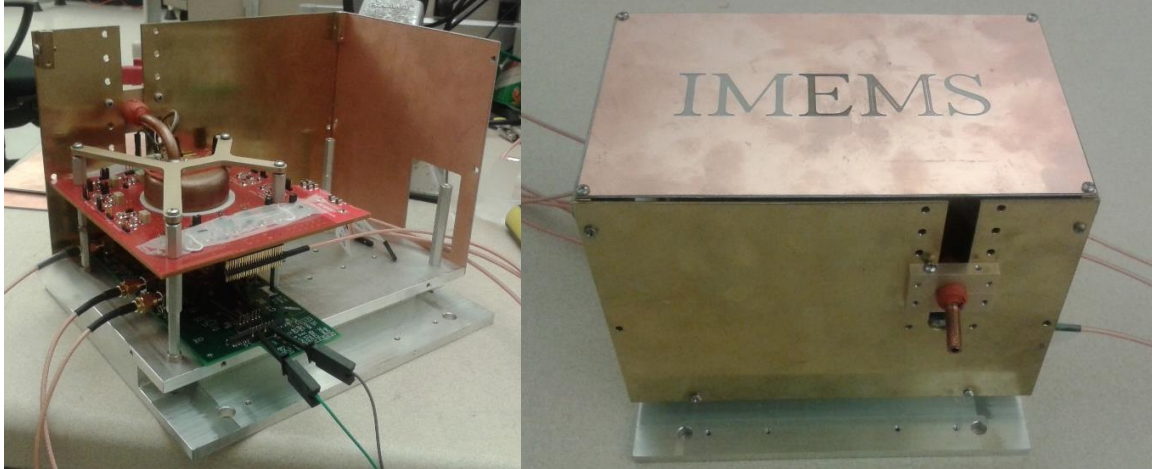
The gyroscope was characterized using an Ideal Aerosmith 1291BR rate table with 0.01% rotation rate accuracy. The characterization setup is shown in Figure 66 and Figure 67. The AFE and analog back-end were separated in order to make tuning and characterization of the analog front-end easier during testing. The total power consumption is 2.2W, drawing approx. 138mA at 16v ( $\pm 8v$ ). The AFE including the on-board vacuum chamber is mounted in the chassis with a break-out board below it as shown in Figure 67 (a). The exterior of the chassis is shown in Figure 67 (b). The data is then processed using the gyroChar custom MATLAB toolbox described in Appendix H. A summary of the gyroscope characterization is given in Table 7.

**Table 7: Comparison of calculated and measured parameters**

<b>Characterization Results</b>		
Parameter	Calculated	Measured
$f_{RES}$ (Hz)	6.7108k	6.7108k
$f_{LOCK}$ (Hz)	6.7108k	6.7108k
AM Sensitivity (pA/ $^{\circ}$ /s)	4.96	1.21
AM Scale Factor (mV/ $^{\circ}$ /s)	34.7	8.57
FM Scale Factor (mV(mHz)/ $^{\circ}$ /s)		1.46
ENE $\Omega$ ( $^{\circ}$ /hr)	1.271	
MNE $\Omega$ ( $^{\circ}$ /hr)	13.14	
TNE $\Omega$ ( $^{\circ}$ /hr)	13.2	2040
ARW (o/vhr)	0.22	34
Bias Instability ( $^{\circ}$ /hr)		330

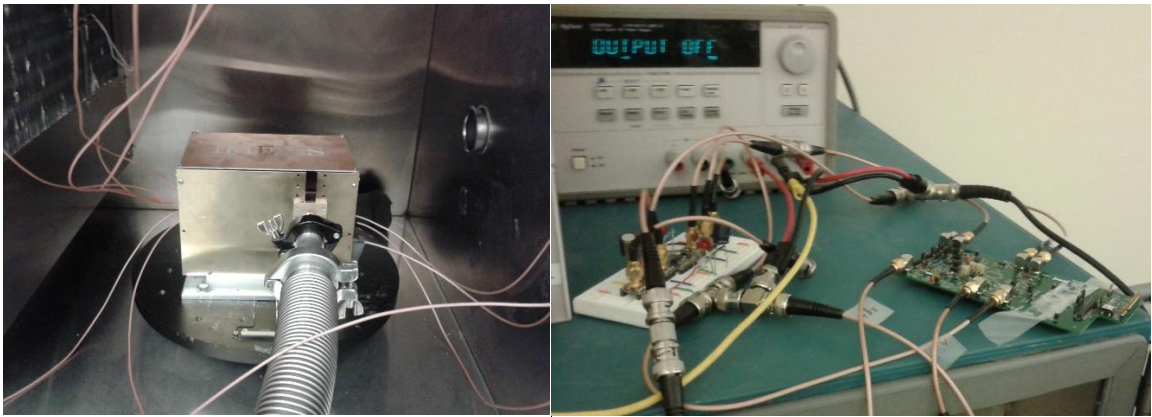


**Figure 66: Gyroscope Characterization Setup**



(a)

(b)



(c)

(d)

**Figure 67: Assembled Gyroscope Characterization Platform showing (a) and (b) the AFE mounted in the chassis with the signal breakout board attached (c) The platform mounted on the rate table, and (d) The Analog back-end board (right) and drive loop feed-through filter (left)**

### ***3.1 Drive Loop Characterization***

The frequency of the drive loop is determined by the loop phase of the drive oscillator. The drive oscillator will lock to the frequency where the loop phase is  $0^\circ$ . Therefore in order to lock to the resonant frequency, the loop phase at the resonant frequency must be  $0^\circ$ . The resonant frequency is measured at  $V_{reg}$ , the highest amplitude drive loop signal, using an Agilent 53181A frequency counter and Agilent 35670A dynamic signal analyzer. The dynamic signal analyzer is setup to take the FFT of  $V_{REG}$ .

The frequency counter and dynamic signal analyzer both give a drive frequency of 6.7108kHz. The spectrum of the drive loop is shown in Figure 68. The measured resonant frequency of the  $\mu$ HSR and the AFE is matched to the drive frequency of 6.7108kHz as shown in the AFE frequency response in Figure 69. The regulation of the drive voltage by the ALC under rotation is demonstrated in Figure 70. The envelope of the drive signal remains constant even as energy is transferred from the drive mode to the sense mode under rotation.

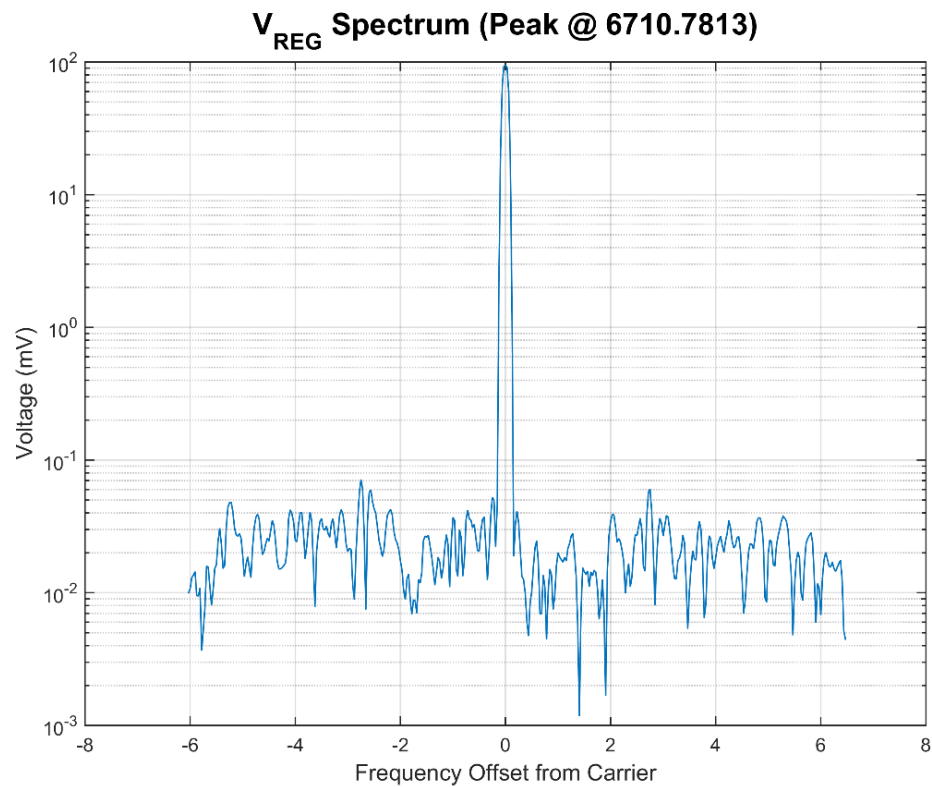


**Figure 68: Spectrum of drive loop V<sub>REG</sub>**

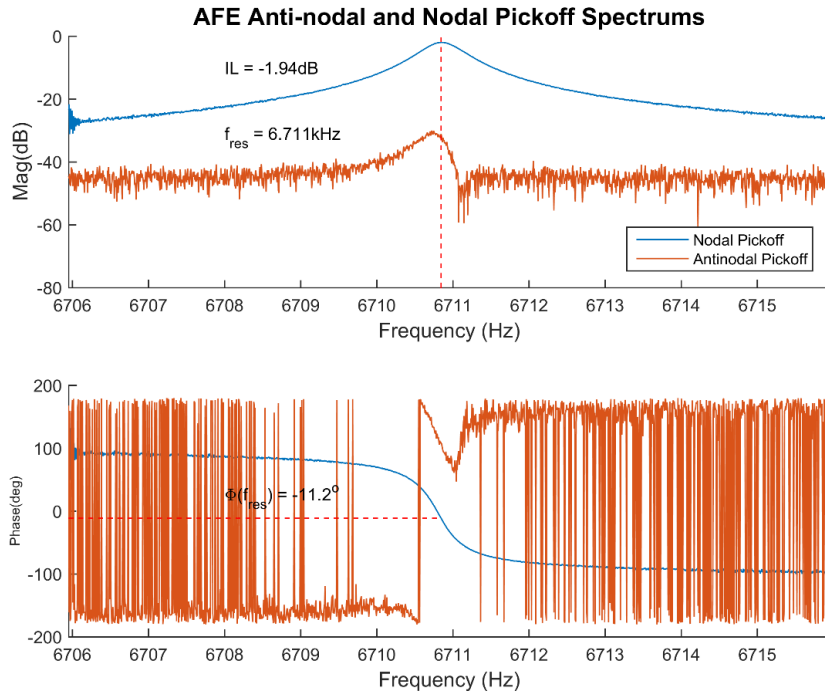


**Figure 69: Frequency response of the AFE including the  $\mu\text{HSR}$ .**

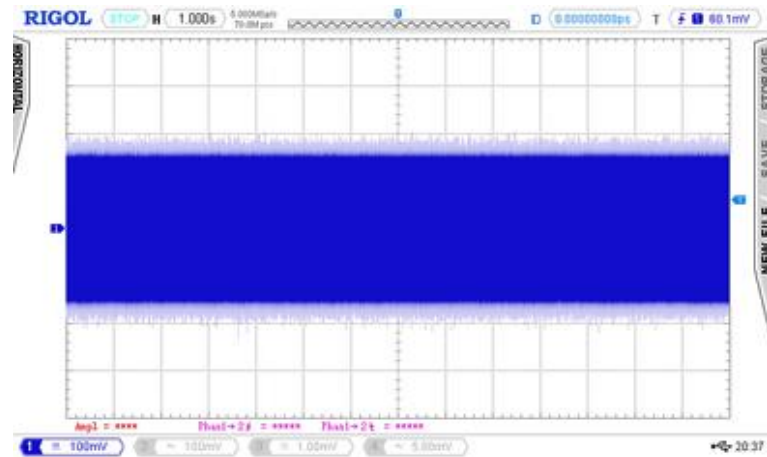


**Figure 70: Regulated drive voltage with the DUT under rotation ( $V_{REG}$ ) (1 sec/div, 100mV/div)**

As the rotation rate increases beyond the dynamic range of the  $\mu\text{HRG}$ , the modes begin to split and the drive frequency increases with increasing rotation rate. The frequency should increase linearly with rotation rate and hence this shift can be used to measure the rotation rate outside of the bandwidth of the AM  $\mu\text{HRG}$  interface by measuring this FM signal. By monitoring the FM rate output the system can detect when

it is operating outside the range of the AM interface and hence the dynamic range of the interface is extended by using an AM/FM interface instead of a purely AM interface.

This frequency shift can be measured by using the drive voltage,  $V_{REG}$ , as the reference to a phase locked loop. (PLL) The VCO center frequency of the PLL is set to the ZRO frequency of the drive loop. The frequency shift can then be measured by monitoring the control voltage of the VCO, which then also becomes the FM rate output.

A PLL for measuring the frequency shift was implemented using a Zurich Instruments HF2LI lock-in amplifier. The VCO control voltage, with a VCO gain of 1V/Hz, was then output to an Agilent DSO6014A oscilloscope. A sinusoidal rotation at 2Hz was then applied to the  $\mu$ HRG and the FM rate output was saved to a comma separated value (csv) file for each input rate and then processed using the same scale factor analysis tool, gyroChar\_ScaleFactor, used for plotting the AM scale factor. This gives the FM rate response shown in Figure 71 and the transient FM rate response to 100.531 °/s shown in Figure 72. The FM scale factor shows a linear response with a 1.46 mHz/°/s scale factor. The dynamic range measured is limited by the required vacuum connection.

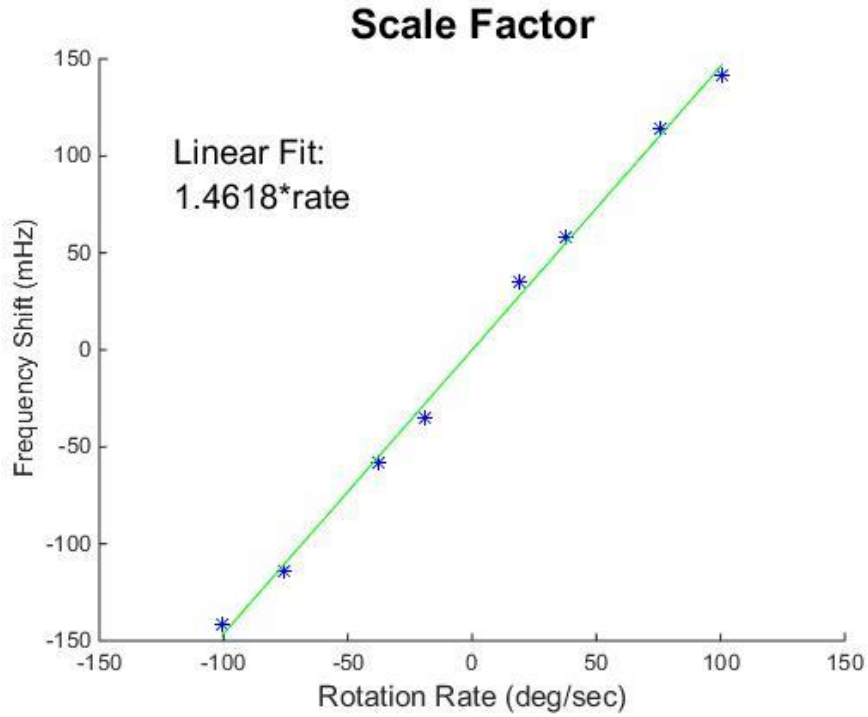


**Figure 71: FM rate response scale factor**

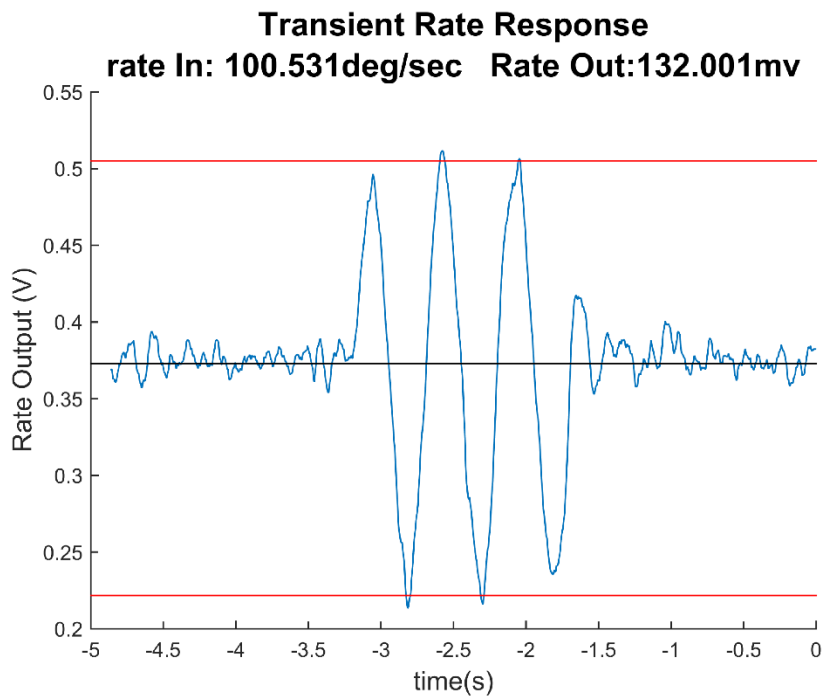


**Figure 72: FM transient rate response to a 100.531 %/s rotation rate.**

## 3.2 Scale Factor Characterization

### 3.2.1 AM readout scale factor

The scale factor was characterized by measuring the transient rate response at several different rates. An example rate response is shown in Figure 73 for a rate input of approx. 15 %/sec. The gyroscope was rotated at a frequency of 0.15 Hz, well within the 0.3Hz bandwidth of the  $\mu$ HSR.

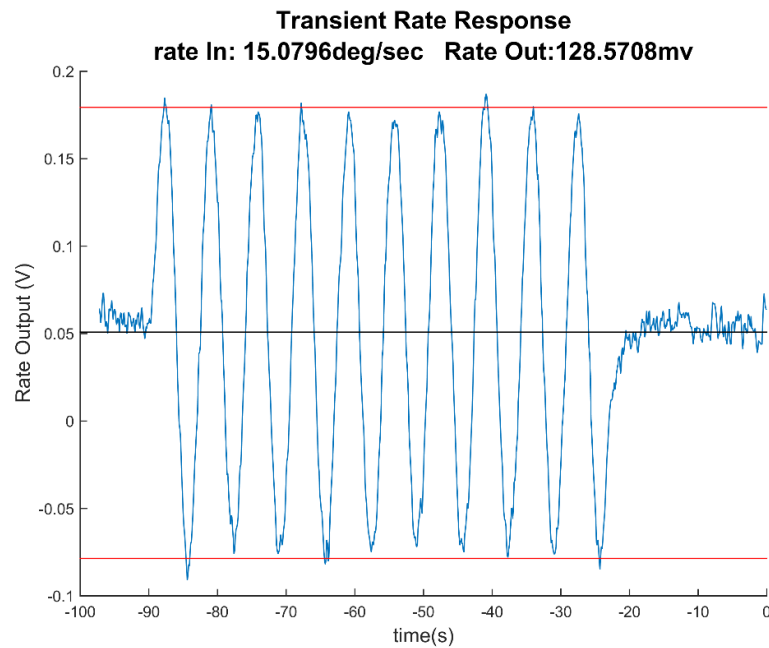


**Figure 73: Rate Response for a rate input of 25 %/sec**

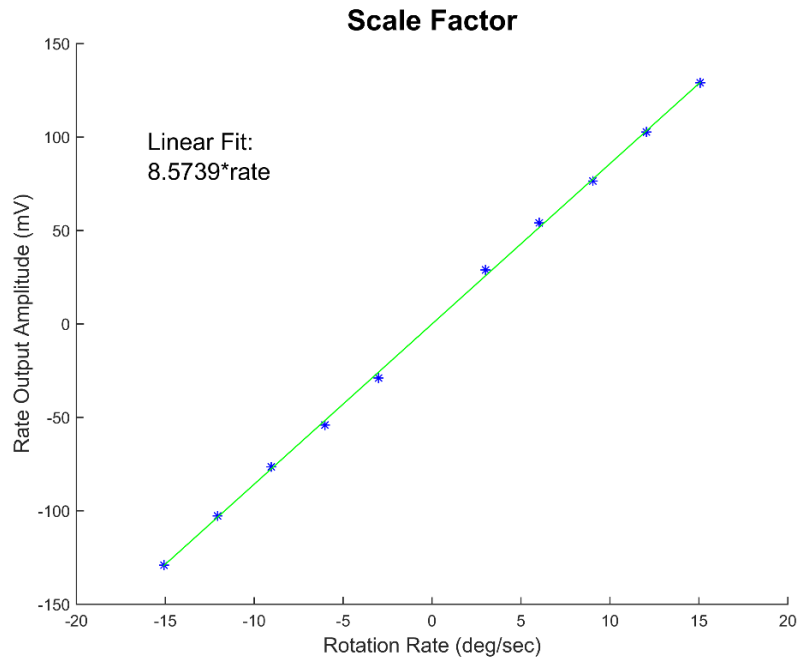


**Figure 74: Rate Response showing a scale factor of 8.57 mV/°/s**

### 3.2.2 AM/FM hybrid Readout with expanded dynamic range

The AM and FM readout methods described previously can be used together to extend the dynamic range of the  $\mu$ HRG as shown in Figure 75. The high Q and low frequency of the  $\mu$ HSR cause it to have a narrow bandwidth. This narrow bandwidth constrains the dynamic range of the synchronous AM readout channel to low rotation rates. At rates outside the bandwidth of the  $\mu$ HSR, the FM readout provides a linear rate response as demonstrated in section 3.1.

The final rate output could be generated using a simple logic block. The FM rate output could be compared to a threshold and then the comparator output could be used to select the correct rate output using a switch. When the rate signal is within the bandwidth of the device, the AM rate output would be used with its better scale factor and lower noise. However, if the rotation rate exceeds the bandwidth of the  $\mu$ HSR, then the FM rate output would be used. Figure 76 shows the extension of the dynamic range

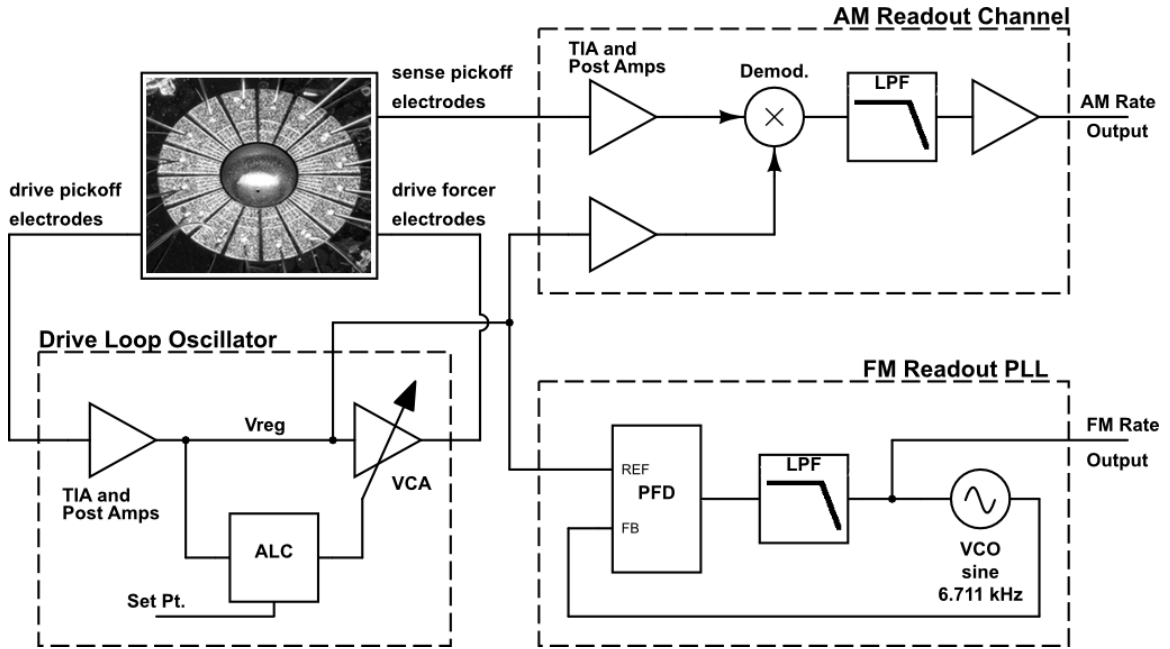


Figure 75: Hybrid AM/FM  $\mu$ HRG Block Diagram

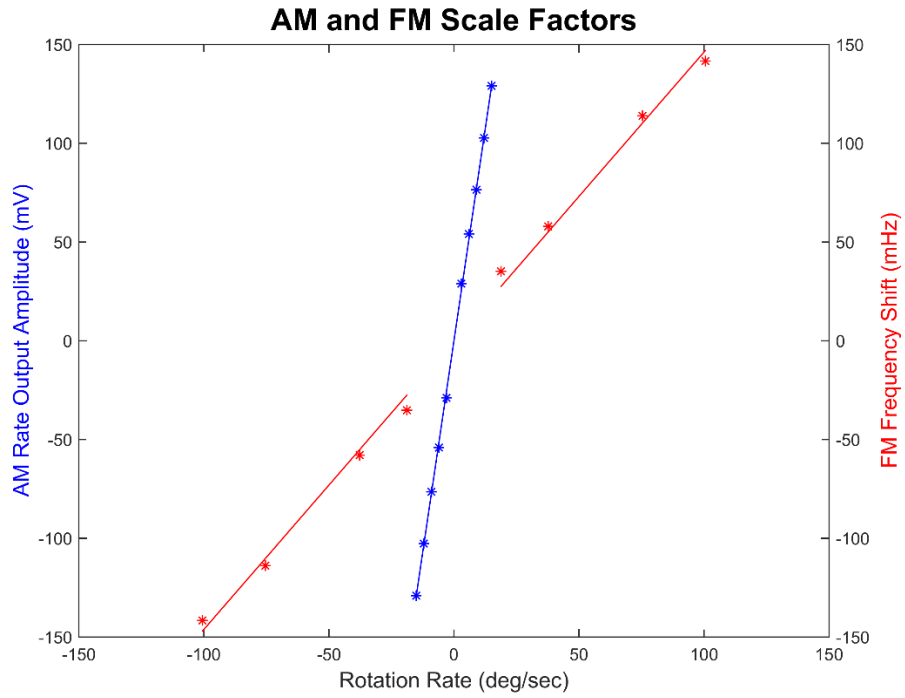
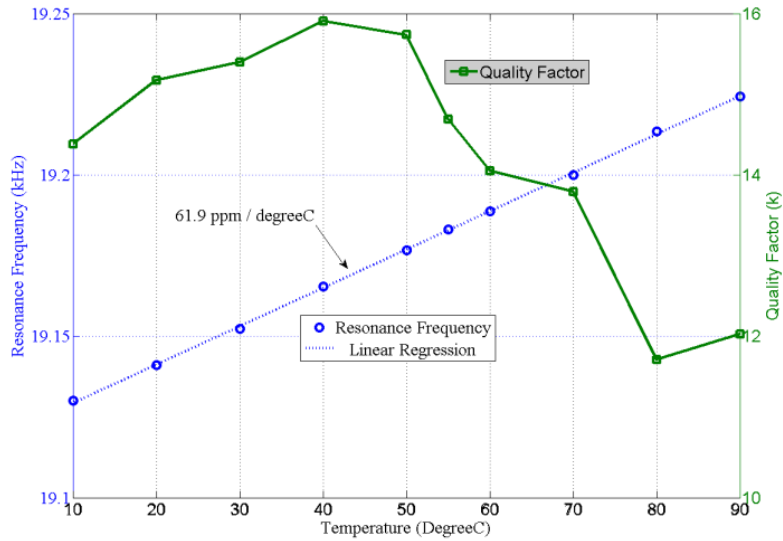


Figure 76: AM (blue) and FM (red) Rotation Rate Responses showing scale factors of 8.57 mV/o/s and 1.46 mHz/o/s, respectively

However, the FM scale factor of just 0.217ppm/°/s, the TCF is 61.9 ppm/°C, and the quality factor varies with frequency, as shown in Figure 77. Hence, to ensure an accurate FM rate output, the TCF must be compensated. One method of compensating the TCF may be to use a second adjacent device on the same substrate as the VCO in the FM read out PLL.



**Figure 77: TCF and quality factor temperature dependence**

### 3.3 Noise Characterization

The noise performance of the gyroscope was measured while the gyroscope was at rest by sampling the zero rate output using a Zurich Instruments H2FLI lock-in amplifier at 900Hz. The Allan variance is shown in Figure 78. The bias instability is 329.75 °/hr. at an averaging period of 72.74s. The angle random walk is  $34^\circ / \sqrt{hr}$ . Further improvements in the resonator quality factor and the noise of the drive loop will help improve the noise performance of the gyroscope. It is also believed that the current noise measurements may be effected by the vibration of the vacuum pump, though the vibration sensitivity of the  $\mu$ HRG hasn't been characterized.

# Allan Deviation

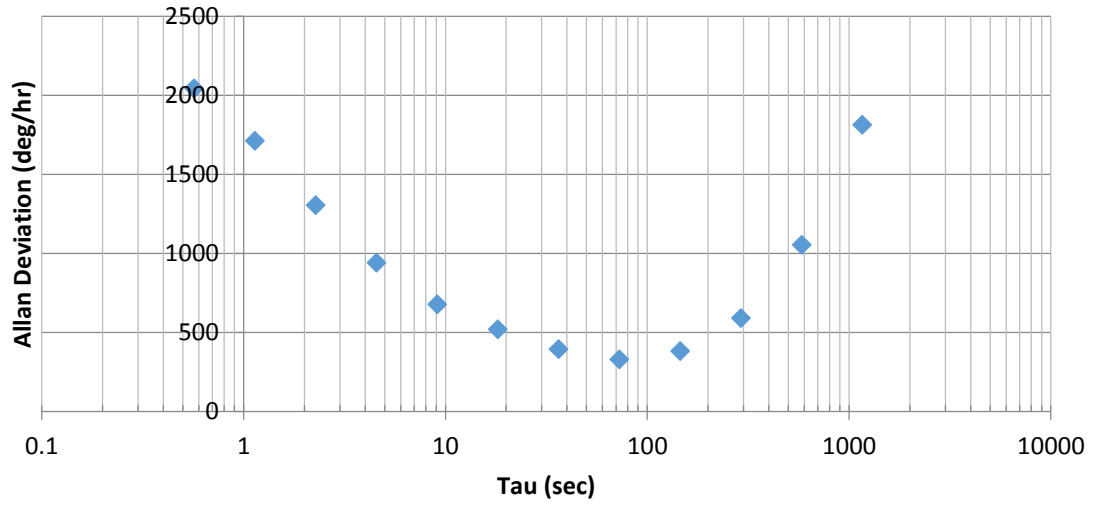


Figure 78: Allan Variance (deviation)

# Chapter 4

## Conclusion and Future Work

### *4.1 Conclusion*

The  $\mu$ HRG has the potential to become a gyroscope with the high performance of traditional macro-scale gyroscopes along with the small cost, size, weight and power-consumption of existing MEMS solutions. The  $\mu$ HSR has already accomplished the size, weight, and cost goals with a batch fabricated resonator that is just 1.2mm in diameter with a total area including the electrodes of 7 mm<sup>2</sup>. While the performance still hasn't reached the level of the macro-scale HRG, there is still room for improvement and further development of the quality factor and interface system.

The  $\mu$ HRG rate interface was developed to turn the micro-hemispherical shell resonator into a rate gyroscope. First the  $\mu$ HSR had to be characterized and modeled. Then the control and readout electronics were developed. This included the drive oscillator, the balancing and quadrature compensation methods, and sense channel for the synchronous demodulation of the rate signal from the drive carrier. The system was implemented using two separate boards, the analog front-end (AFE) contains the direct analog interface to the  $\mu$ HSR and the back-end contains the signal processing.

The resulting gyroscope was then characterized. First, the drive loop was characterized to ensure that the oscillator was locking into the resonant frequency of the  $\mu$ HSR and the ALC was regulating the velocity well. Next, the performance of the rate output was characterized. A scale factor of 8.57mV/°/s was measured at a frequency of 0.15Hz. The noise performance of the rate output was then measured and the Allan variance was plotted and analyzed. The Allan Variance plot gave a bias instability of 330 °/hr and an angle random walk (ARW) of  $34^\circ/\sqrt{hr}$ . While these initial results are far from inertial grade, they have demonstrated the functionality of the system, with further

performance improvements expected. Further development of the resonator and the interface will not only improve the rate performance but also enable rate integrating operation.

## ***4.2 Contributions and lessons***

### **4.2.1 Rate Mode Readout and Control Interface**

The read-out and control interface that turned the  $\mu$ HSR into a working  $\mu$ HRG was developed. It implements a closed drive loop that locks into the resonant frequency of the  $\mu$ HSR and regulates the drive mode amplitude. It also includes a synchronous readout channel for measuring the rate of rotation and separating the rate response from the quadrature output. The system also includes control of the electrostatic quadrature and frequency tuning voltages which tune and bias the  $\mu$ HSR in order to enable the capacitive interface and match the modes. This AM interface had been characterized and can act as the basis for additional experiments and for the design of new interface architectures.

### **4.2.2 Non-linearity**

The non-linearity of the  $\mu$ HSR is significantly larger than initially predicted in simulation as shown in section 2.1.4. This non-linearity was first characterized and then the drive loop gain and drive amplitude set point were adjusted to account for the non-linearity. It was found that to ensure linearity the drive forcer voltage had to be less than 10mV.

The drive loop had to be reconfigured so that the magnitude of the voltage regulated by the ALC voltage is large enough for proper operation of the peak detector, while still keeping the oscillator from doffing. Hence, the drive pick-off amplification was increased. The VCA810 variable gain amplifier's operating point was then selected so that it was operated as a variable attenuator to avoid non-linearity.

### **4.2.3 Feed-through Cancellation**

The feed-through level of the device is more complicated than a simple capacitive feed-through model. While the feed-through level at low frequencies is attenuated significantly by the current feed-through cancellation circuit, at higher frequencies the feed-through levels begin to increase significantly at frequencies within the bandwidth of the feed-through cancellation circuit. As discussed in section 2.4.2, a feed-through filter was implemented in the drive loop to ensure that the drive oscillator locked to the resonant frequency.

It is also interesting to note that the feed-through cancellation circuit from the drive forcer to the sense pick-off reduces the feed-through level at the drive pick-off. While the current feed-through model, discussed in section 2.1.5, begins to capture some of these affects, further work on modelling the feed-through of the  $\mu$ HSR needs to be conducted.

### **4.2.4 On-board Vacuum Chamber**

An onboard vacuum chamber and support chassis was developed to provide a vacuum to the  $\mu$ HSR and enable high quality factors that aren't limited by air or squeezed film damping. The support chassis not only provides mechanical support for the on-board vacuum chamber but also provides a flexible platform for supporting the interface and control electronics.

## ***4.3 Future Work Summary***

The next stage of the interface development will consist of a redevelopment of the interface to support whole angle and rate mode while improving the methods used for characterization of both the resonator and the interface. First, a new mixed-signal board design will need to be developed to enable implementation of advanced DSP methods needed to control a rate integrating interface. Next, a discrete rate-integrating gyroscope

will need to be implemented to demonstrate the system. It will then culminate with the design of a mixed signal ASIC for the control and read-out of the  $\mu$ HRG in whole angle mode and force feedback rate mode.

#### ***4.4 Next stage goals***

There are five main goals for the next stage of development:

- Develop a whole angle mode gyroscope interface.
- Develop a mixed signal ASIC for the control and readout of whole angle and rate mode gyroscopes.
- Develop the embedded instrumentation to effectively evaluate different interface architectures and resonators.
- Develop noise models for prediction of Allan variance performance.
- Improve the performance of the  $\mu$ HRG to its full potential.

#### ***4.5 New interface Architecture***

A digital back-end will need to be developed for the control of the device. This method will allow support for both whole-angle and rate-integrating operation. The rate interface can be implemented in DSP. The drive loop will utilize a software-defined phase locked loop and the sense channel can be realized in both an open-loop configuration with digital demodulation and in a closed-loop force feedback configuration for larger bandwidth.

#### ***4.6 Quadrature and Frequency Tuning Control***

##### **4.6.1 Automatic mode matching**

Currently the  $\mu$ HRG is mode-matched by tuning the two independent quadrature control voltages and the two independent frequency tuning voltages. A method for automatically matching the two modes should be implemented. First the AFE should be configured so that the 2 frequency control voltages are no longer independent but instead form a single differential voltage controlled by a single input so that  $V_{T1} = -V_{T2}$ . An

open-loop frequency control system could be implemented either in analog or digital using the open loop control equations. The AFE would also need to be configured to accept the appropriate input signal range. A similar method would also need to be applied to the quadrature control voltages to form an open-loop quadrature control system.

#### **4.6.2 Closed Loop Quadrature Control**

Further improvements in the mode matching and the quadrature control system could be implemented using a closed loop quadrature control system. The quadrature level could be sensed by demodulating the quadrature component of the pick-off signal. This signal could then be regulated using a controller to control the DC bias of the  $\pm 22.5^\circ$  quadrature electrodes. This would need to be implemented in order to implement whole angle mode.

#### ***4.7 Improved Instrumentation***

- A gyroscope test and evaluation system for efficient measurement of both resonator and gyroscope parameters similar to the URAT [40, 75, 76] should be implemented for efficient and cost effective evaluation of the  $\mu$ HRG. GnuRadio and MATLAB can be used for the interface to the device and the post-processing of the data. This system should be directly integrated with the interface.
- A probe card system for probing the die should be implemented to eliminate wire-bonding the device during early stages of testing the device. A rotating or polygon holder covering the different possible orientations of the device would be necessary to keep the device pads aligned with the probe card. This would allow devices to be tested more efficiently in general and enable new types of tests on a larger number of devices.

- An improved vacuum connection method that provides vacuum while allowing the device to rotate at higher dynamic ranges needs to be implemented. Using a longer and more flexible hose would be a good start. A rotary union and an improved chassis could also provide higher dynamic ranges. Ultimately, however, the device needs to be vacuum packaged to go to high dynamic ranges and reduce environmental impacts.

#### ***4.8 Improved Device and System Modelling***

- The substrate feed-through model for the device feed-through needs to be refined.
- A detailed model of the  $\mu$ HRG needs to be created in Simulink and Matlab. This would be useful for testing control and readout algorithms. The Simulink model of tuning fork gyros developed by Sharma [53] can serve as a starting point for a Simulink model of the  $\mu$ HRG. The model would then need to be compared to measured results and incorporate noise models. [77]
- The Simulink model can be used as part of a model-based development (MBD) process where the control algorithms can be simulated and then the control firmware can be directly generated from the model.

#### ***4.9 Mixed Signal ASIC***

One of the major goals of the next step of the interface should be to develop a mixed signal application specific integrated circuit (ASIC) for the control and read-out of the  $\mu$ HRG. Demonstration of the world's first ASIC for whole-angle operation would be a major accomplishment. It would allow further reduction of the C+SWaP and improved performance.

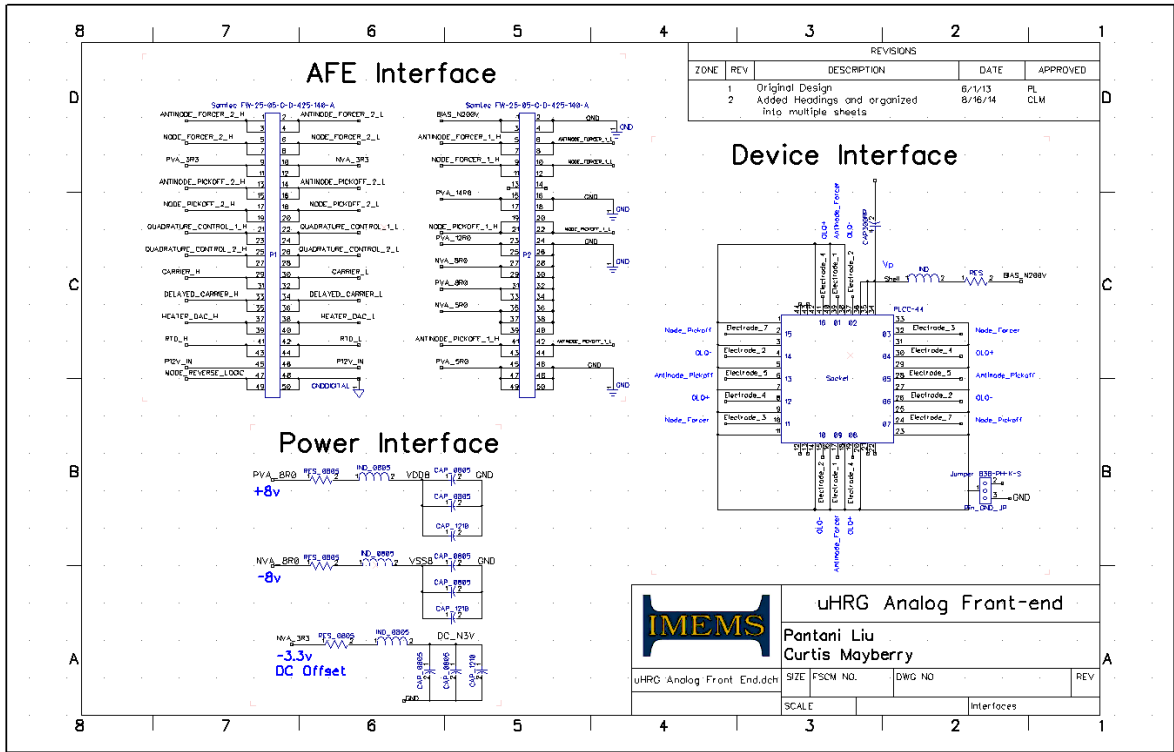
#### **4.10 Resonator Design Feedback**

In future revisions of the  $\mu$ HSR the design of the shell and the electrodes could be optimized to enhance the performance of the system by considering the characterization data and the interface architecture.

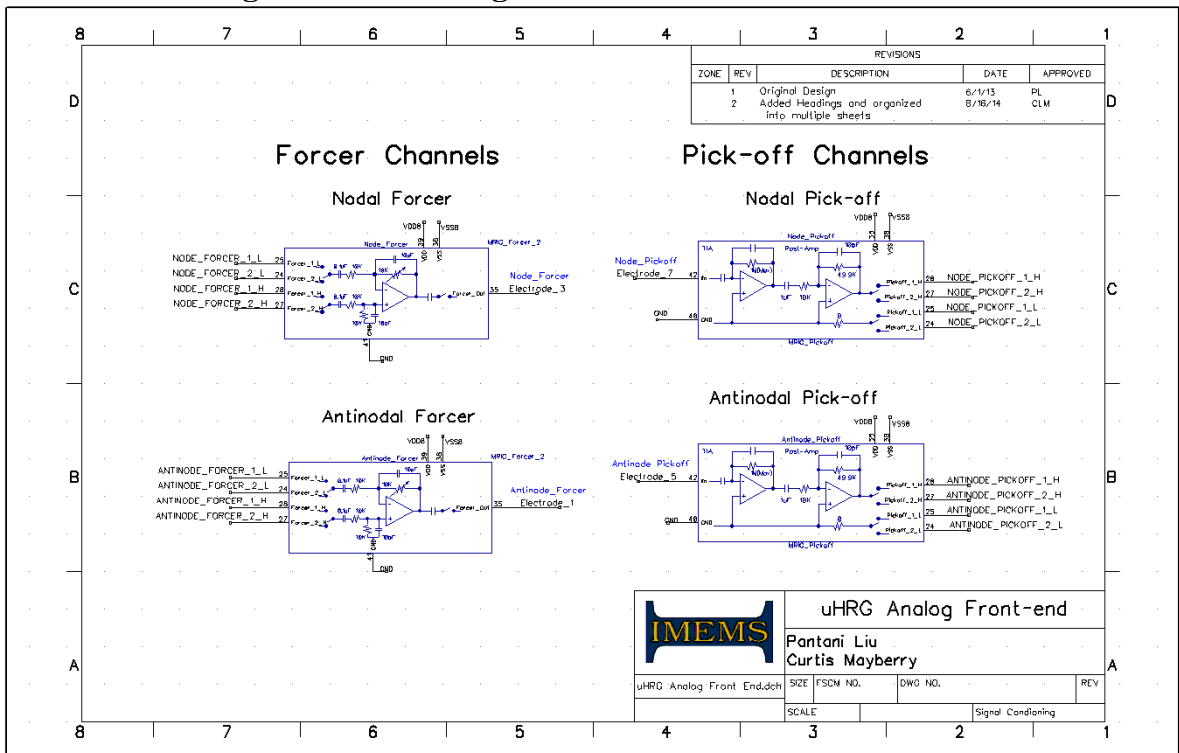
- The gap size could change depending on the function of the electrode. For example, the drive forcer electrodes could have a large gap size to avoid driving the device into non-linearity; while the quadrature and frequency tuning electrodes could keep the current gap size to ensure that the device is still able to be mode matched.
- A center electrode could be implemented to provide a mechanism for amplitude control in whole angle operation.

# Appendix A: Analog Front-end Schematic

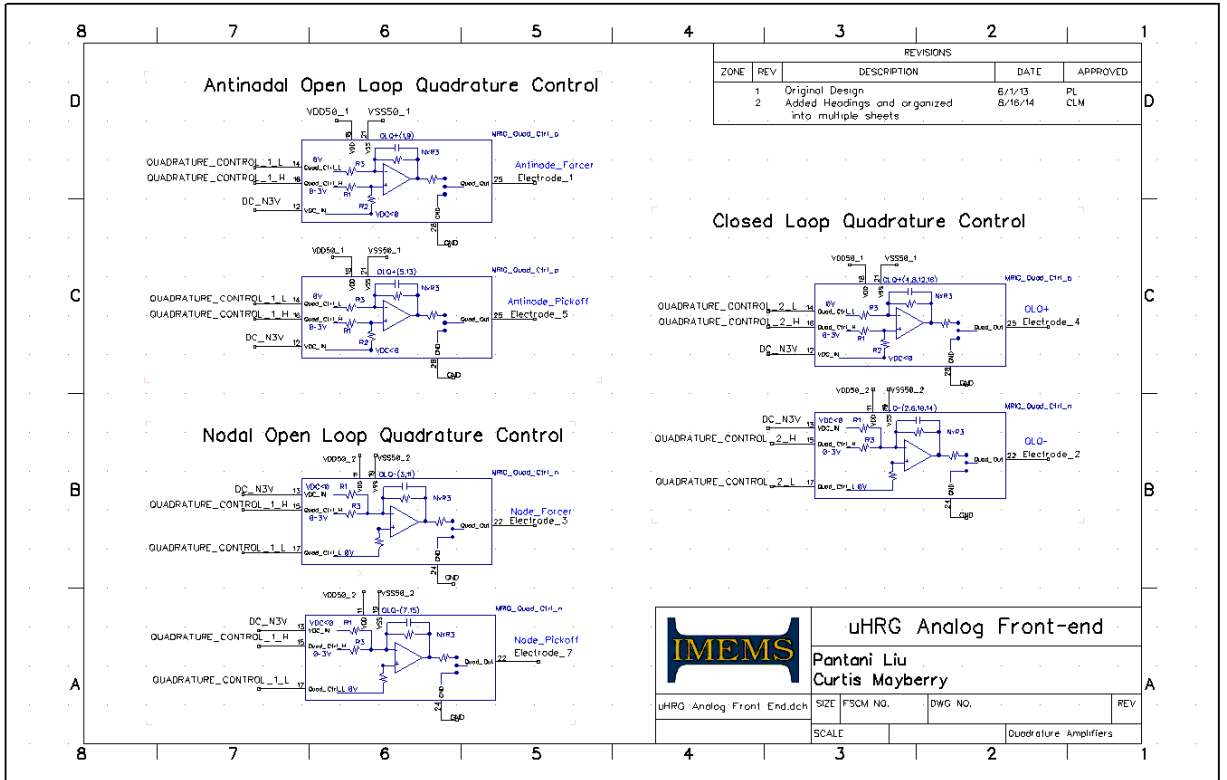
## A.1. Interfaces



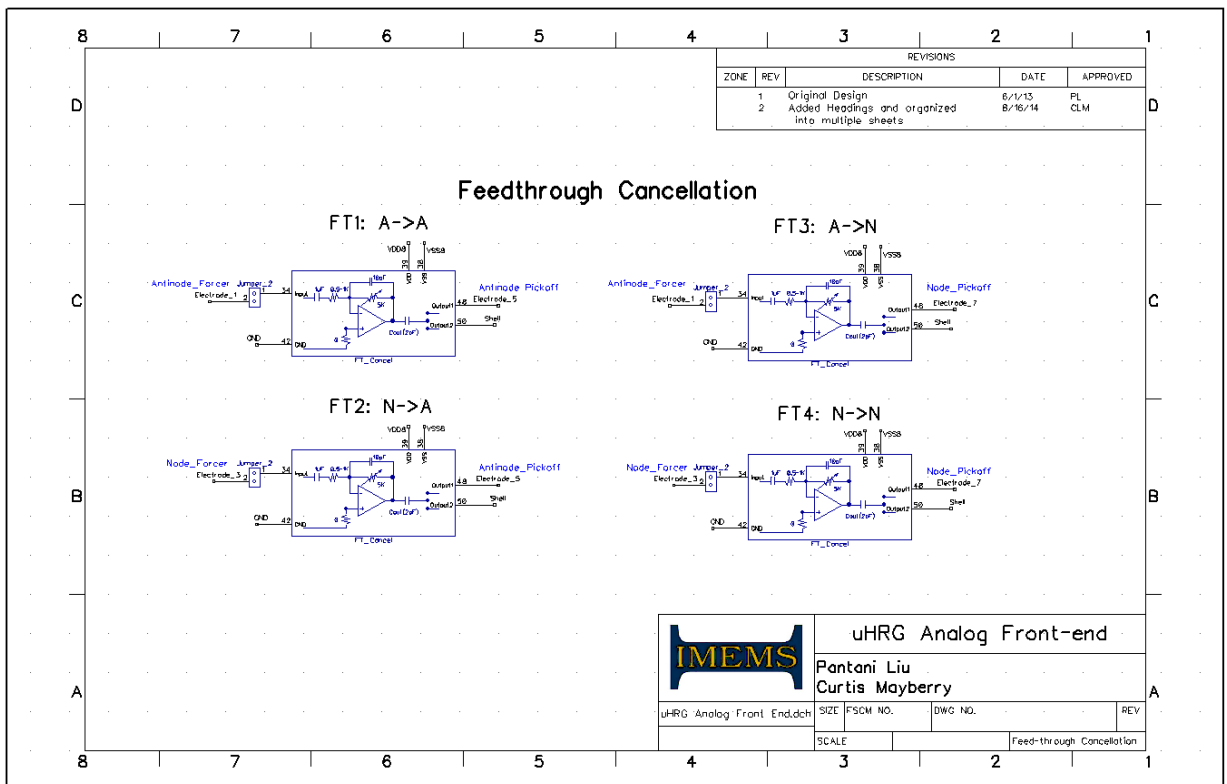
## A.2. Signal Conditioning



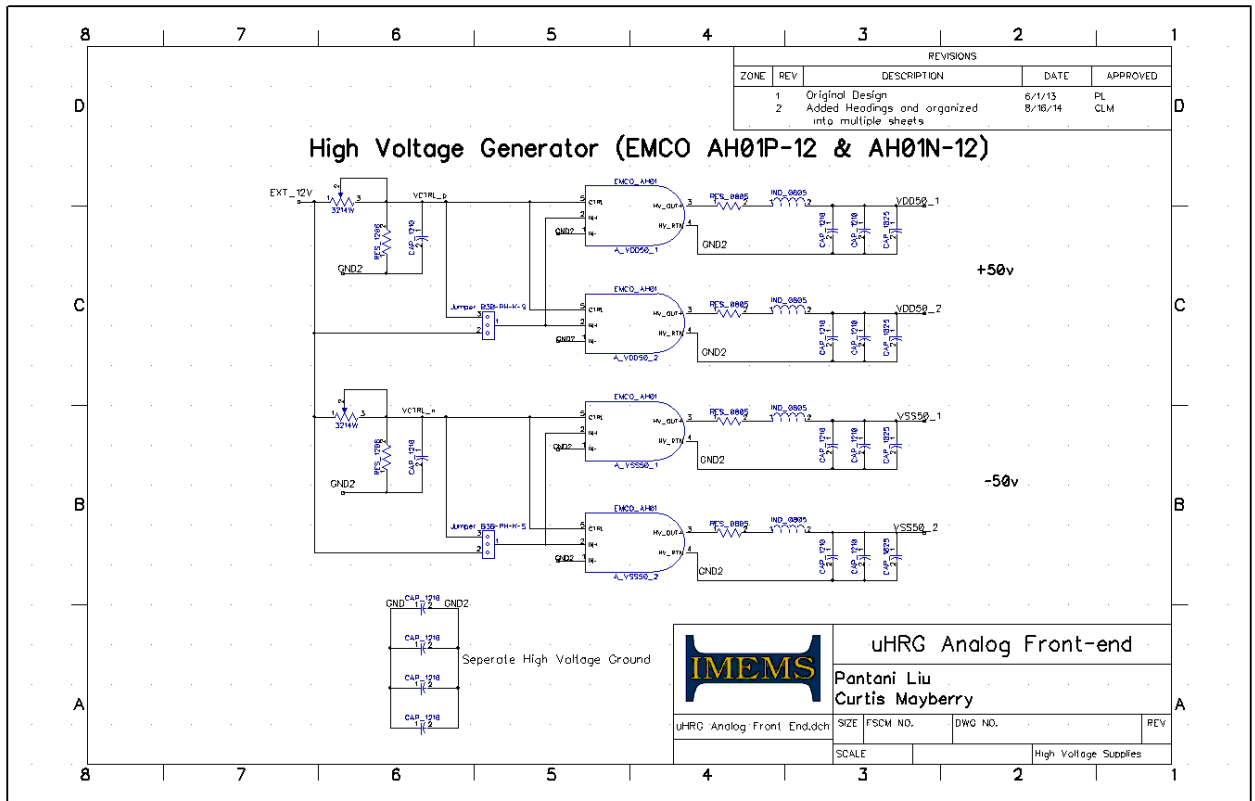
### A.3. Quadrature Amplifiers



### A.4. Feedthrough Cancellation

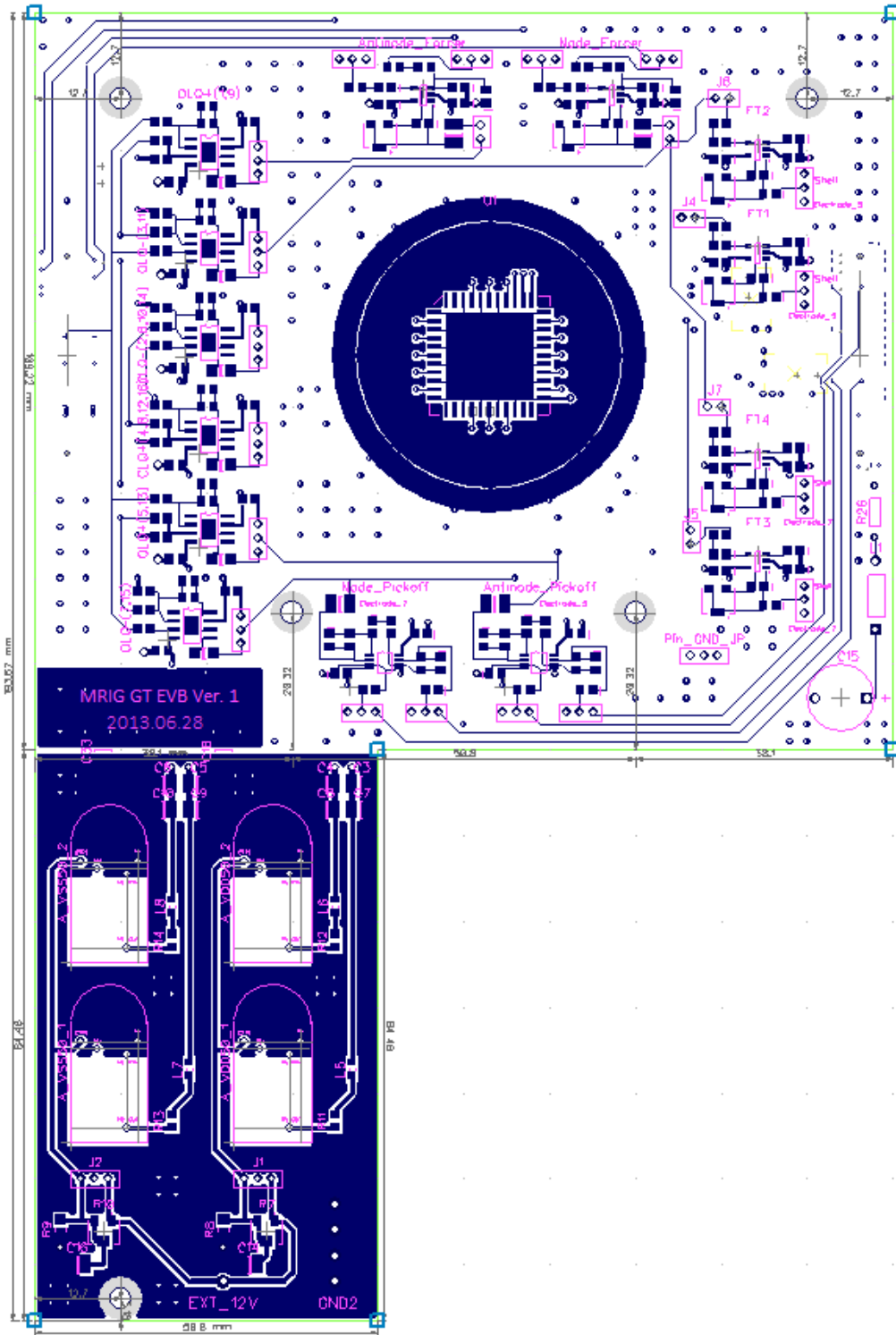


# A.5. High Voltage Supplies

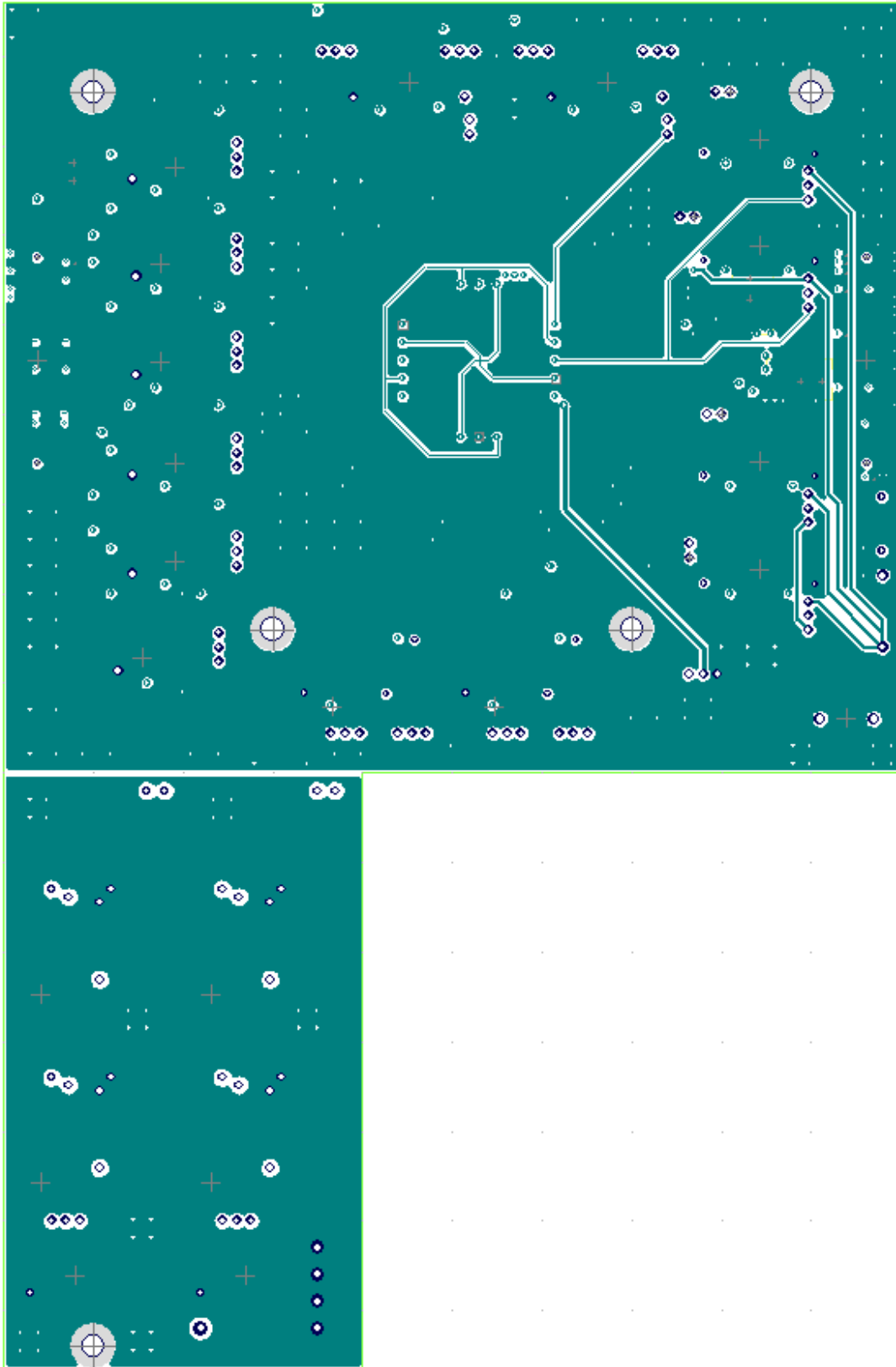


# Appendix B: Analog Front-end Layout

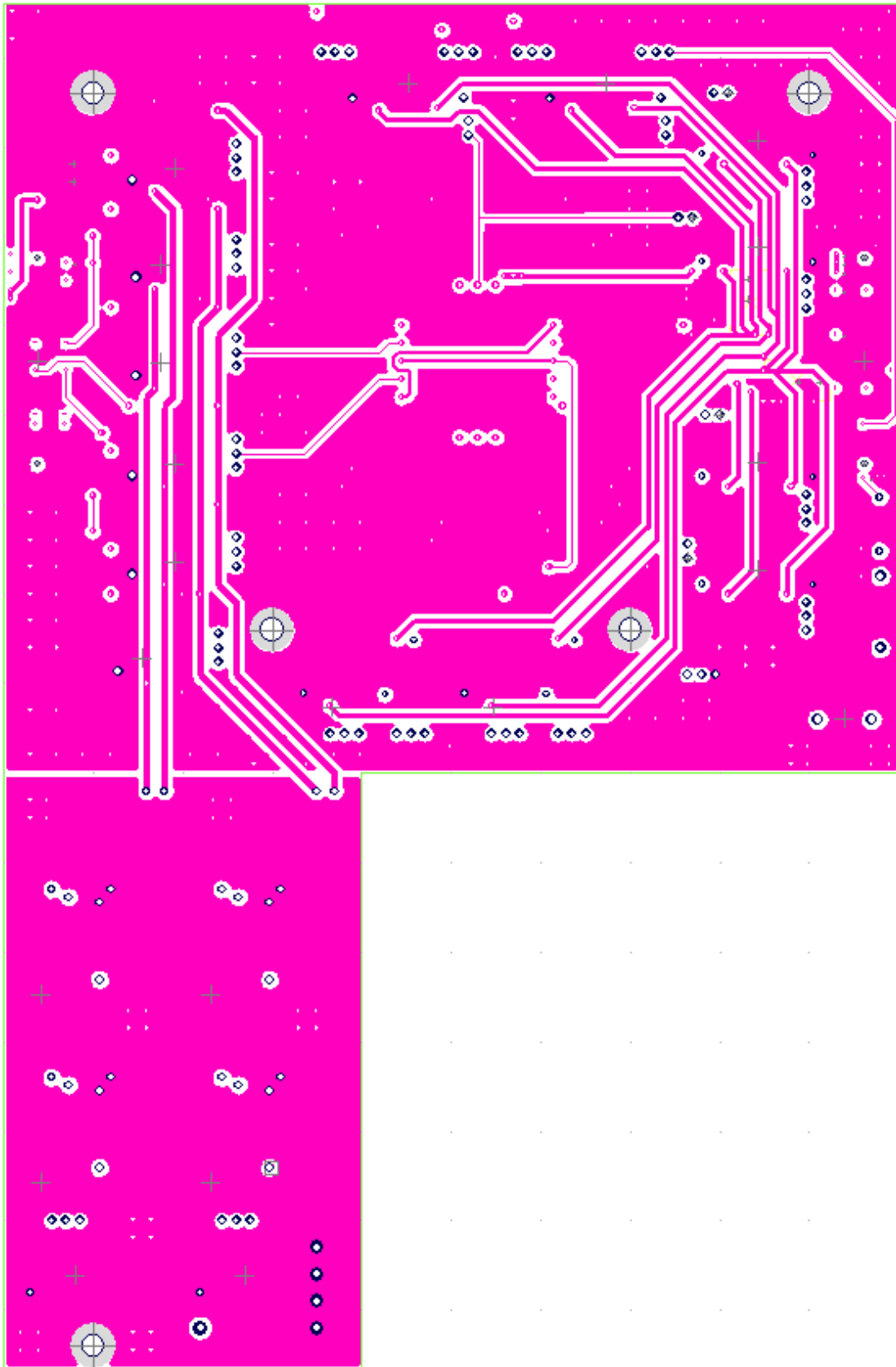
## B.1. Top Layer Layout



## B.2. Inner Layer 1 Layout

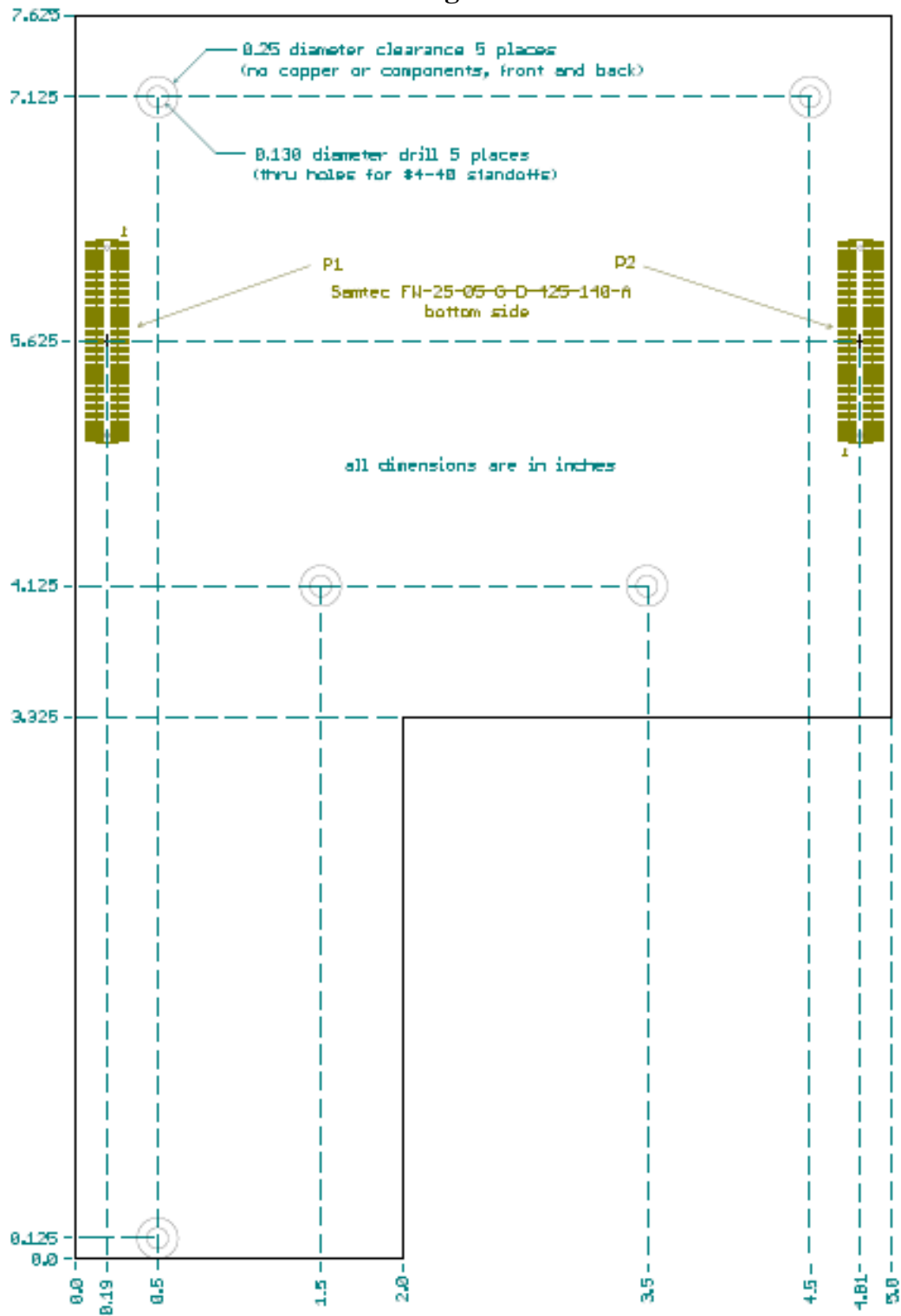


### B.3. Inner Layer 2 Layout





## B.5. Mechanical Drawing



## B.6. Analog Front-end Bill of Materials

MRIG Analog Front End Bill of Materials										
Index	# of boards to be assembled:		8		Board Reference	Minimum Quantity Required	Quantity to be Purchased	Distributor	Distributor Part Number	Description
	Quantity per Board	Value	Package							
1	6	OPA454	850 PowerPAD	OLQ+(1,9), OLQ+(5,13), OLQ-(3,11), OLQ-(7,15), CLQ+(4,8,12,16), CLQ-(2,6,10,14)	48	100	DigiKey	296-22997-5-ND	IC OPAMP GP 2.5MHZ SGL 850PWRPAD	
2	2	OPA2140	8-MSOP	Antinode_Pickoff, Node_Pickoff	16	25	DigiKey	296-27862-1-ND	IC OPAMP J-FET R-R 11MHz 8VSSOP	
3	6	OPA209	SOT23-5	Antinode_Forcere, Node_Forcere, FT1, FT2, FT3, FT4	48	100	DigiKey	296-28152-1-ND	IC OPAMP GP RR0 18MHz SOT23-5	
4	6	951102-8622-AR	2-pos thru hole	Antinode_Forcere, Node_Forcere, J4, J5, J6, J7	48	65	DigiKey	3M9321-ND	CONN HEADER 2POS 2MM VERT T/H	
5	21	951103-8622-AR	3-pos thru hole	J1, J2, Pin_GND JP, OLQ+(1,9), OLQ+(5,13), OLQ-(3,11), OLQ-(7,15), OLQ+(4,8,12,16), OLQ-(2,6,10,14), Antinode_Forcere(2 pieces), Node_Forcere(2 pieces), Antinode_Pickoff(2 pieces), Node_Pickoff(2 pieces), FT1, FT2, FT3, FT4	168	215	DigiKey	3M9322-ND	CONN HEADER 3POS 2MM VERT T/H	
6	11	60@100MHz	L_0805	C17, C18, C32, C33, L2, L3, L4, L5, L6, L7, L8	88	120	DigiKey	A102077CT-ND	FERRITE CHIP 60 OHM 850MA 0805	
7	12	0	R_0805	Antinode_Pickoff(2 pieces), Node_Pickoff(2 pieces), FT1, FT2, FT3, FT4, OLQ-(3,11), OLQ-(7,15), CLQ+(4,8,12,16), CLQ-(2,6,10,14)	96	200	DigiKey	541-0.0TBCT-ND	RES 0.0 OHM .33W JUMP 0805 SMD	
8	4	2K	R_0805	OLQ+(1,9), OLQ+(5,13), CLQ+(4,8,12,16), CLQ-(2,6,10,14)	32	44	DigiKey	RHM22.0KAECT-ND	RES 2K OHM .4W 1% 0805 SMD	
9	6	100K	R_0805	OLQ+(1,9), OLQ+(5,13), CLQ+(4,8,12,16), CLQ-(2,6,10,14), Antinode_Pickoff, Node_Pickoff	48	66	DigiKey	RHM100KAECT-ND	RES 100K OHM .4W 1% 0805 SMD	
10	16	10K	R_0805	R8, R9, Antinode_Forcere(3 pieces), Node_Forcere(3 pieces), Antinode_Pickoff, Node_Pickoff, OLQ+(1,9), OLQ+(5,13), OLQ-(3,11), OLQ-(7,15), CLQ+(4,8,12,16), CLQ-(2,6,10,14)	128	170	DigiKey	RHM10.0KAECT-ND	RES 10K OHM .4W 1% 0805 SMD	
11	6	22K	R_0805	OLQ+(1,9), OLQ+(5,13), OLQ-(3,11), OLQ-(7,15), CLQ+(4,8,12,16), CLQ-(2,6,10,14)	48	65	DigiKey	RHM22.0KCHCT-ND	RES 22K OHM 1/BW 1% 0805 SMD	
12	2	340K	R_0805	OLQ-(3,11), OLQ-(7,15)	16	50	DigiKey	311-340KCRCT-ND	RES 340K OHM 1/BW 1% 0805 SMD	
13	4	100M	R_0805	OLQ+(1,9), OLQ+(5,13), OLQ-(3,11), OLQ-(7,15)	32	50	DigiKey	RHM22.0KCHCT-ND	RES 100M OHM 1/BW 5% 0805	
14	2	499K	R_0805	Antinode_Pickoff, Node_Pickoff	16	25	DigiKey	311-499KCRCT-ND	RES 499K OHM 1/BW 1% 0805 SMD	
15	4	499	R_0805	FT1, FT2, FT3, FT4	32	50	DigiKey	P499CCT-ND	RES 499 OHM 1/BW 1% 0805 SMD	
16	7	10	R_0805	R1, R2, R3, R11, R12, R13, R14	56	77	DigiKey	RHM10.0BLCT-ND	RES 10 OHM 1/BW 1% 0805 SMD	
17	2	20K	3214W SMD	Antinode_Forcere, Node_Forcere	16	25	DigiKey	3214W-20KECT-ND	TRIMMER 20K OHM 0.25W SMD	
18	4	5K	3214W SMD	FT1, FT2, FT3, FT4	32	44	DigiKey	3214W-50KECT-ND	TRIMMER 5K OHM 0.25W SMD	
19	2	100K	3214W SMD	R7, R10	16	22	DigiKey	3214W-10KECT-ND	TRIMMER 100K OHM 0.25W SMD	
20	6	10p	C_NPO_0805	Antinode_Forcere(2 pieces), Node_Forcere(2 pieces), Antinode_Pickoff, Node_Pickoff	48	66	DigiKey	478-5779-1-ND	CAP CER 10PF 100V 1% NPO 0805	
21	4	2p	C_NPO_0805	FT1, FT2, FT3, FT4	32	44	DigiKey	478-6216-1-ND	CAP CER 2PF 100V NPO 0805	
22	13	10u	C_1210	C1 to C10, C13, C14, C16	104	140	DigiKey	445-7004-1-ND	CAP CER 10UF 50V 10% X75 1210	
23	6	100p	C_NPO_0805	Antinode_Pickoff, Node_Pickoff, FT1, FT2, FT3, FT4	48	100	DigiKey	478-3732-1-ND	CAP CER 100PF 100V 1% NPO 0805	
24	54	1u	C_0805	C11, C12, C20, C21, C24, C25, Antinode_Forcere(5 pieces), Node_Forcere(5 pieces), Antinode_Pickoff(4 pieces), Node_Pickoff(4 pieces), OLQ-(1,9)(3 pieces), OLQ+(5,13)(3 pieces), OLQ-(3,11)(3 pieces), OLQ-(7,15)(3 pieces), CLQ+(4,8,12,16)(3 pieces), CLQ-(2,6,10,14)(3 pieces), FT1(3 pieces), FT2(3 pieces), FT3(3 pieces), FT4(3 pieces)	432	550	DigiKey	445-6974-1-ND	CAP CER 1UF 100V 10% X75 0805	
25	4	4.7u	C_1210	C19, C22, C23, C26	32	44	DigiKey	445-7005-1-ND	CAP CER 4.7UF 100V 10% X75 1210	
26	1	not populated	thru hole	L1	0	0				
27	27	SPN025XCN-RC		Not on board - please procure and deliver with parts kit	216	280	DigiKey	59339-ND	CONN JUMPER SHORTING 2MM GOLD	
28	2	FW-25-05-G-D-425-140-A	50-pos surface mount board spacers	P1, P2	16	22	Samtec	FW-25-05-G-D-425-140-A	must be "-A" part with alignment pins	
29	2	EMCO AH01P-12		A_VDD50_1, A_VDD50_2	16	20	Northrop will procure	AH01P-12	+100V High Voltage Supply	
30	2	EMCO AH01N-12		A_VSS50_1, A_VSS50_2	16	20	Northrop will procure	AH01N-12	-100V High Voltage Supply	

## Appendix C: Analog Front End Errata

### AFE Errata 1: V<sub>p</sub> RLC filter capacitor C15

The capacitor, C15, on the polarization voltage RLC filter has the second pad floating. It should be connected to ground.

### AFE Errata 2: Pickoff Channel LPF Corner Frequency

The pickoff channel's feedback capacitors are too large and introduce too much phase shift at the resonance frequency (Approx. 6.7 kHz). The TIA feedback capacitor must be changed from 10pF (F<sub>c</sub> = 32 kHz) to 5pF (F<sub>c</sub> = 64 kHz) and the Post-amp feedback capacitor must be changed from 100pF (F<sub>c</sub> = 16 kHz) to 27pF. (F<sub>c</sub> = 59 kHz)

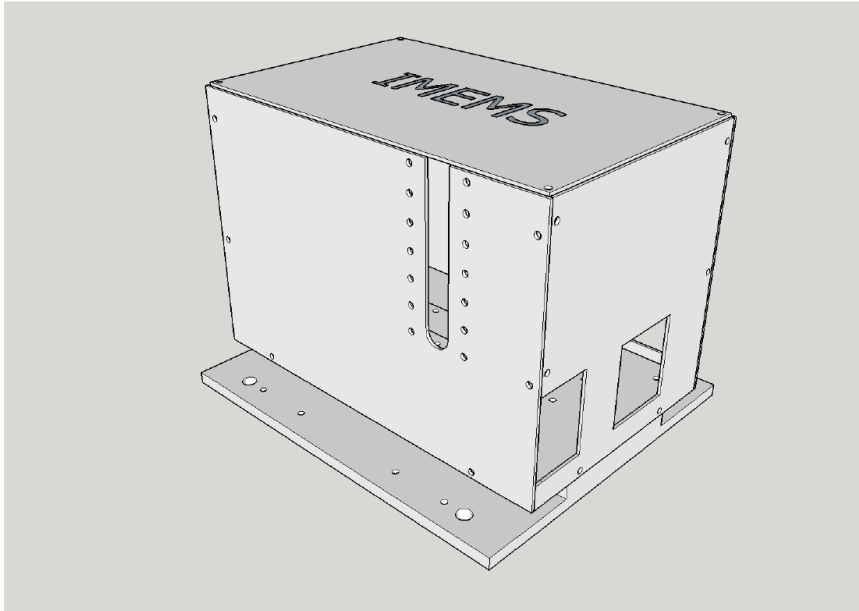
### AFE Errata 3: Chassis grounding

There should be an option to ground the chassis by placing metal grounding pads around the screw holes.

# Appendix D: On-board Vacuum Chamber

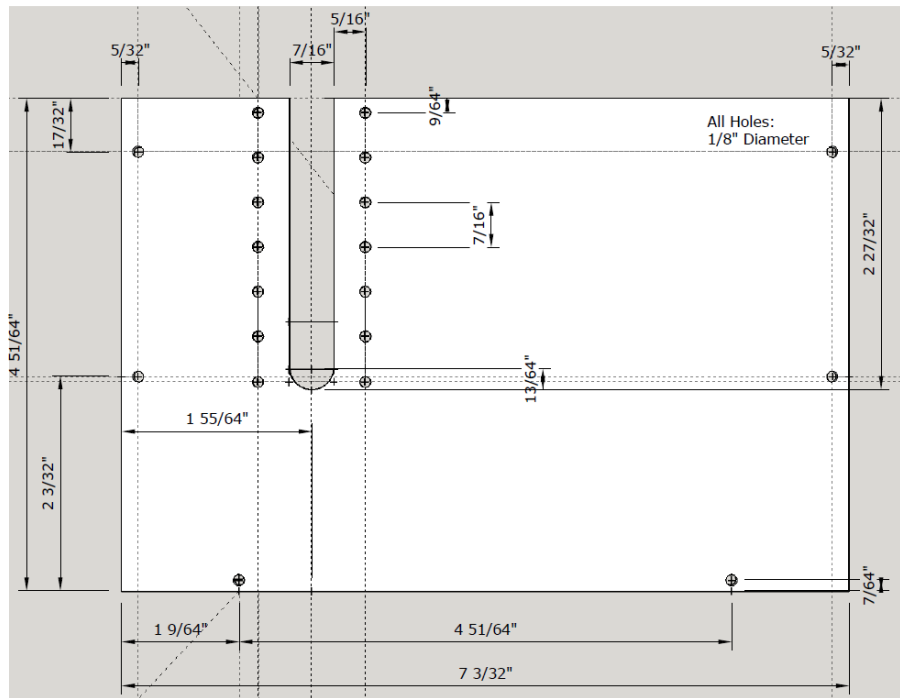
## Mechanical Drawings

### D.1. Assembled View



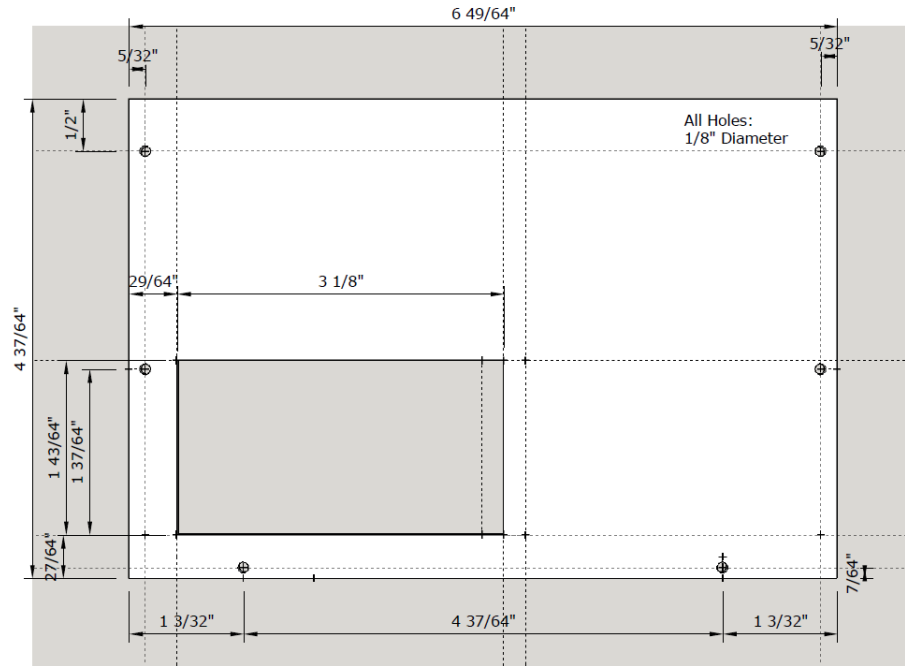
Assembled View

### D.2. Chassis Front Side View



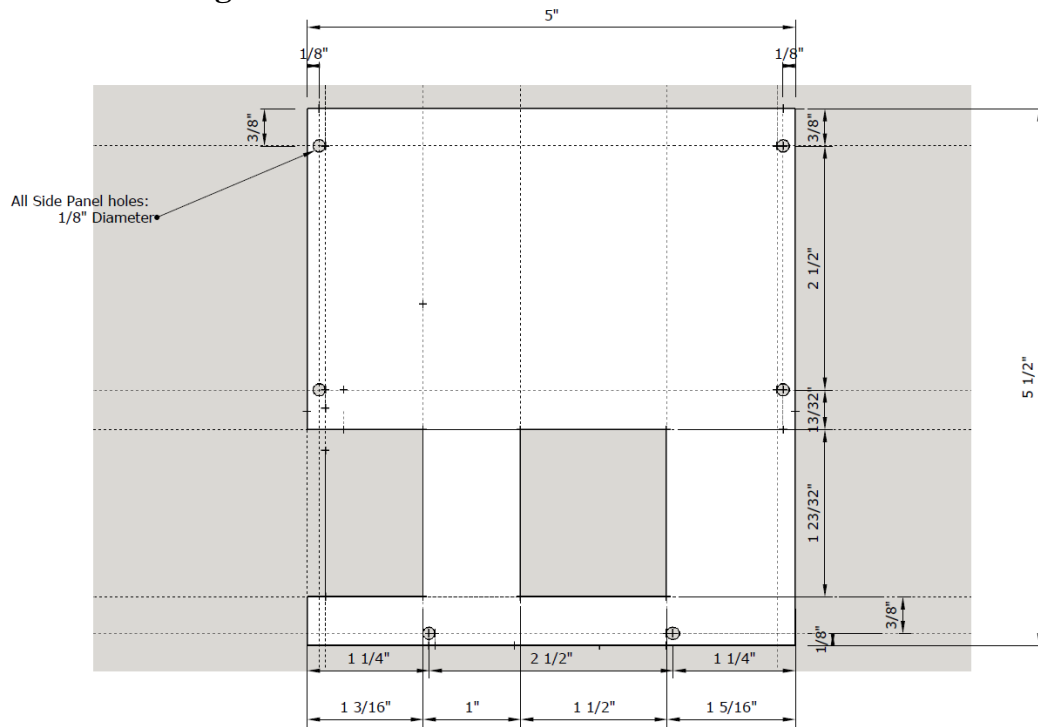
Front Panel  
Material: Brass  
Thickness:  $\frac{1}{16}$ "

### D.3. Chassis Back Side



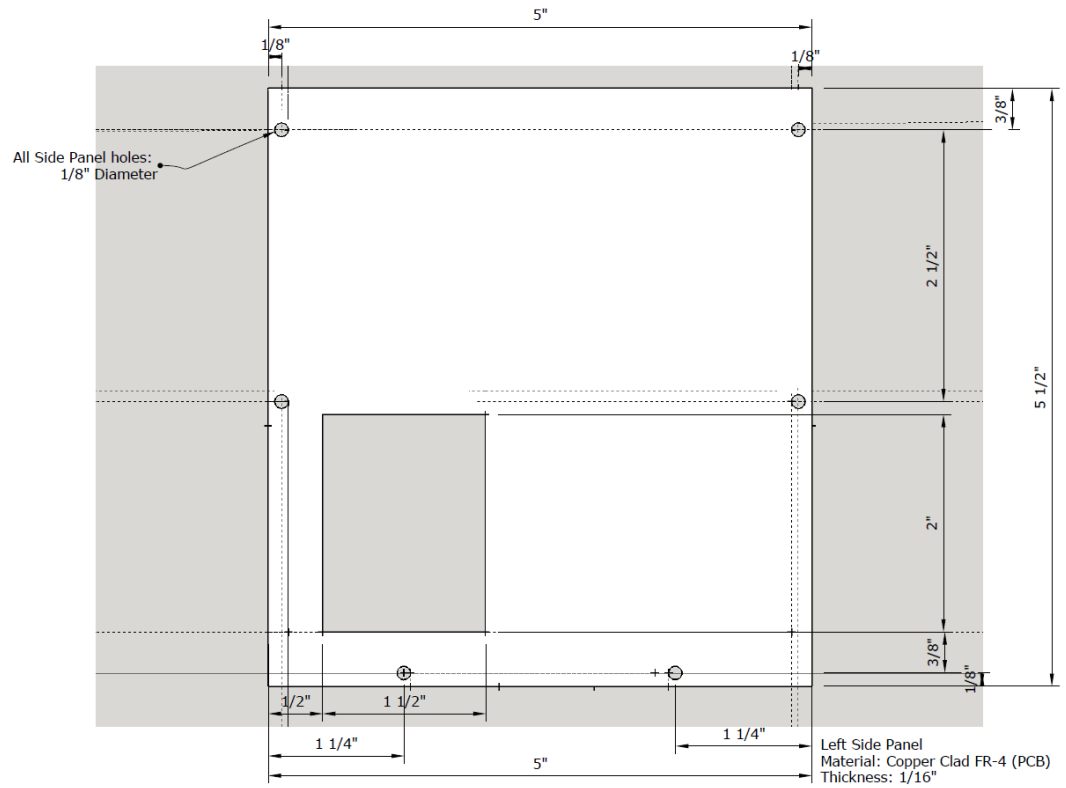
Back Panel  
Material: Copper Clad FR-4 (PCB)  
Thickness: 1/16" or 1/8"

### D.4. Right Side Panel

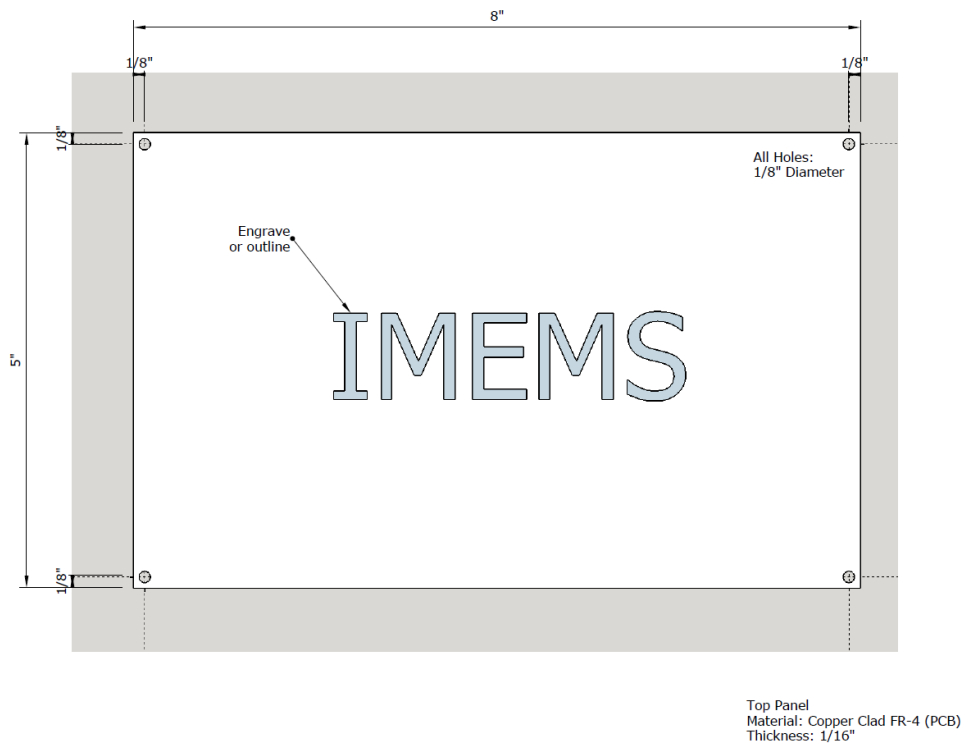


Right Side Panel  
Material: Copper Clad FR-4 (PCB)  
Thickness: 1/16"

### D.5. Left Side Panel



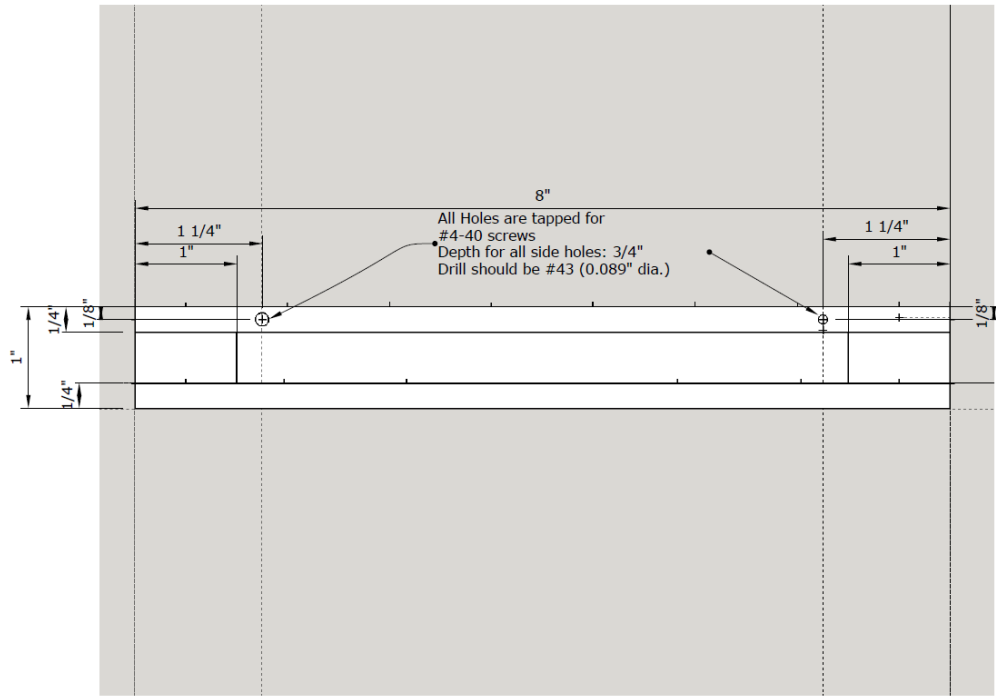
### D.6. Top Panel





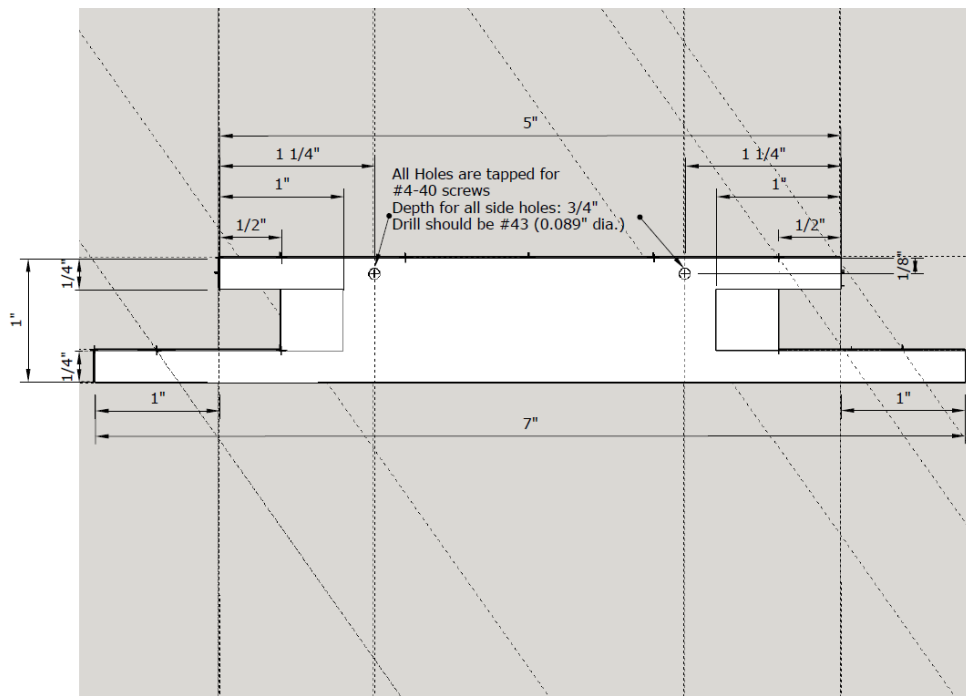


### D.11. Base Front and Back View



Base  
Right/Left Side View  
Material: Aluminum

### D.12. Base Right and Left Side View

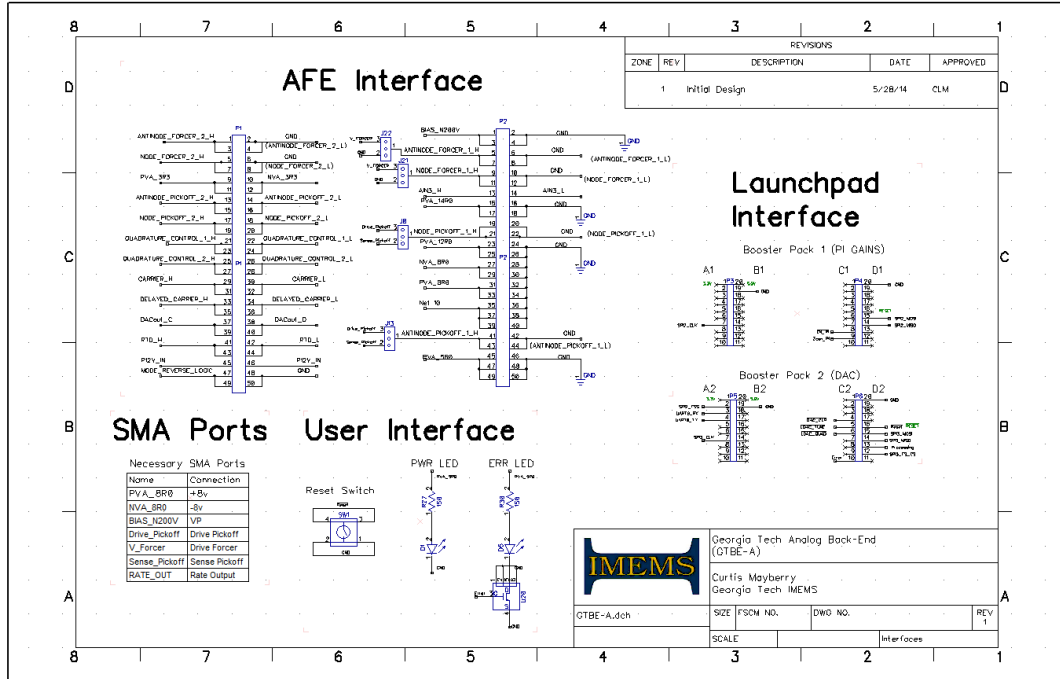


Base  
Front/Back Side View  
Material: Aluminum

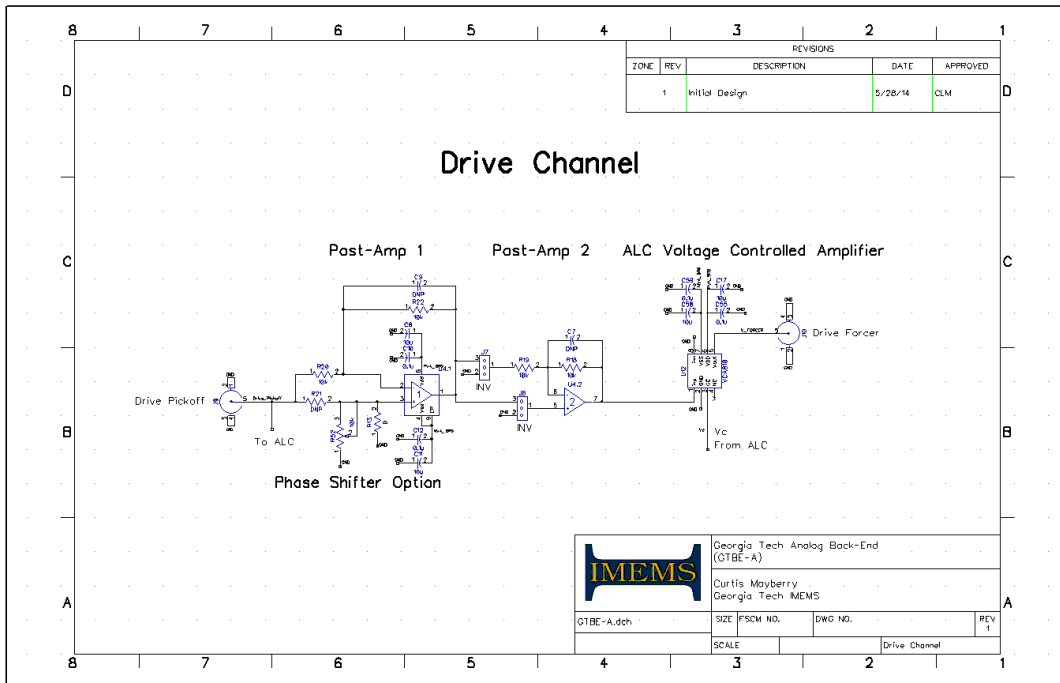
# Appendix E: Closed Loop Interface (GTBE-A)

## Schematic

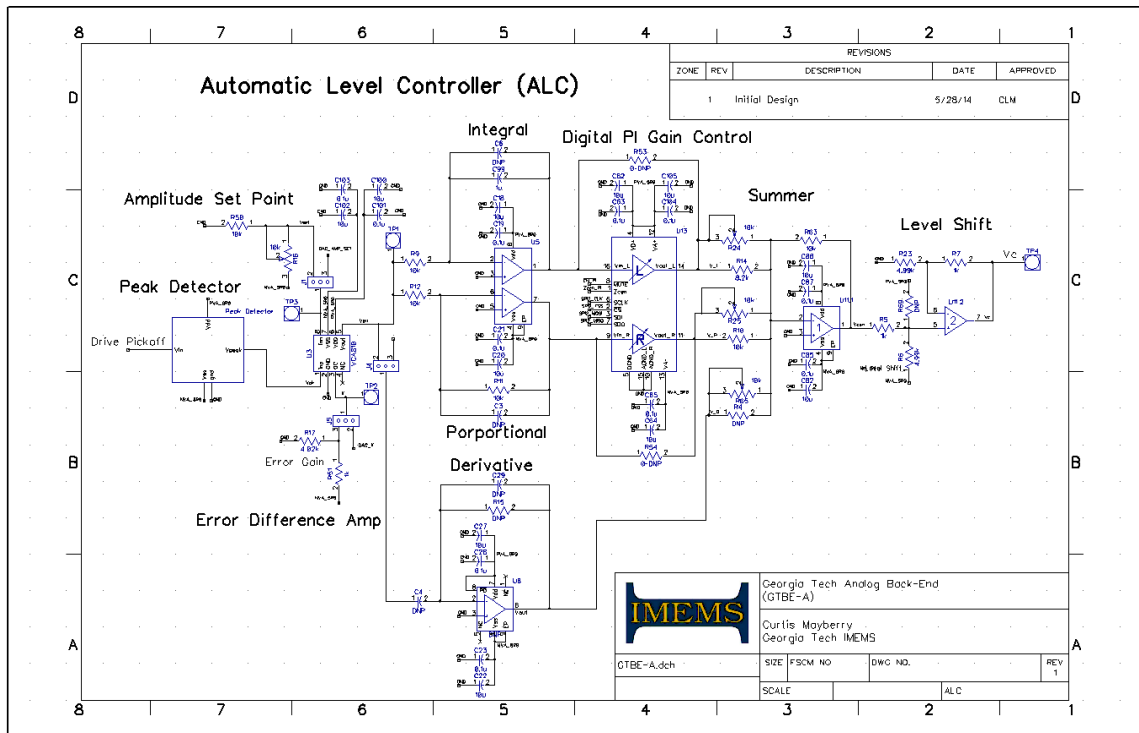
### E.1. Interfaces



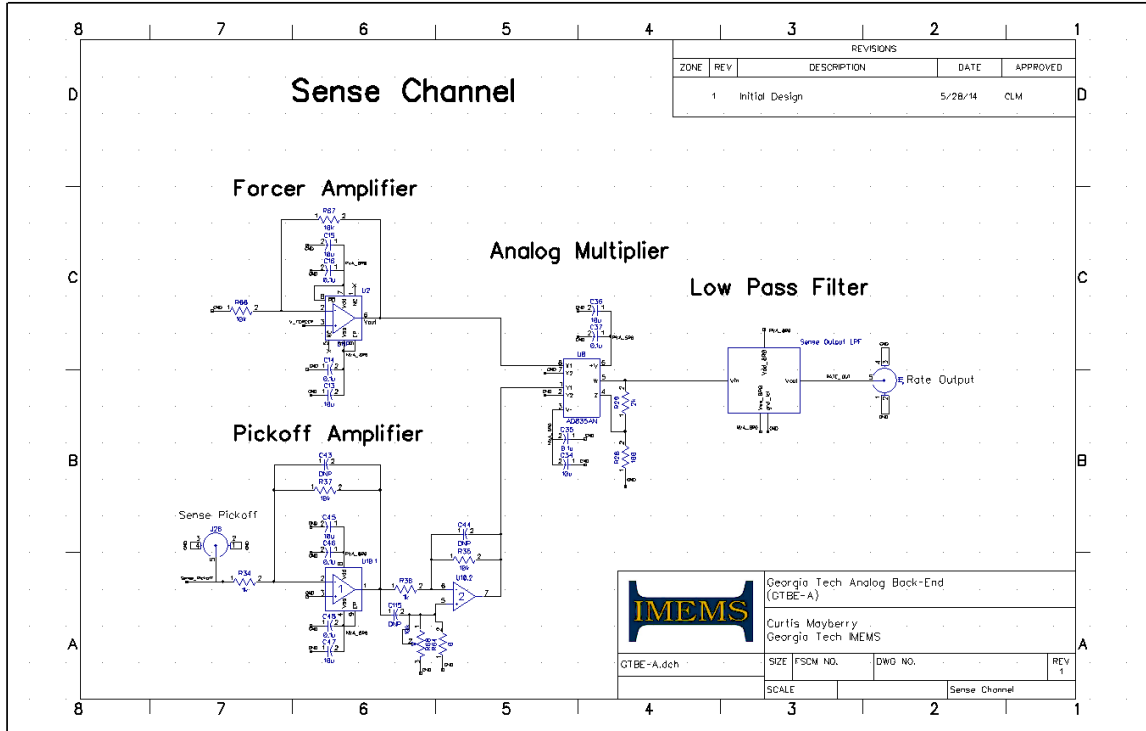
### E.2. Drive Channel



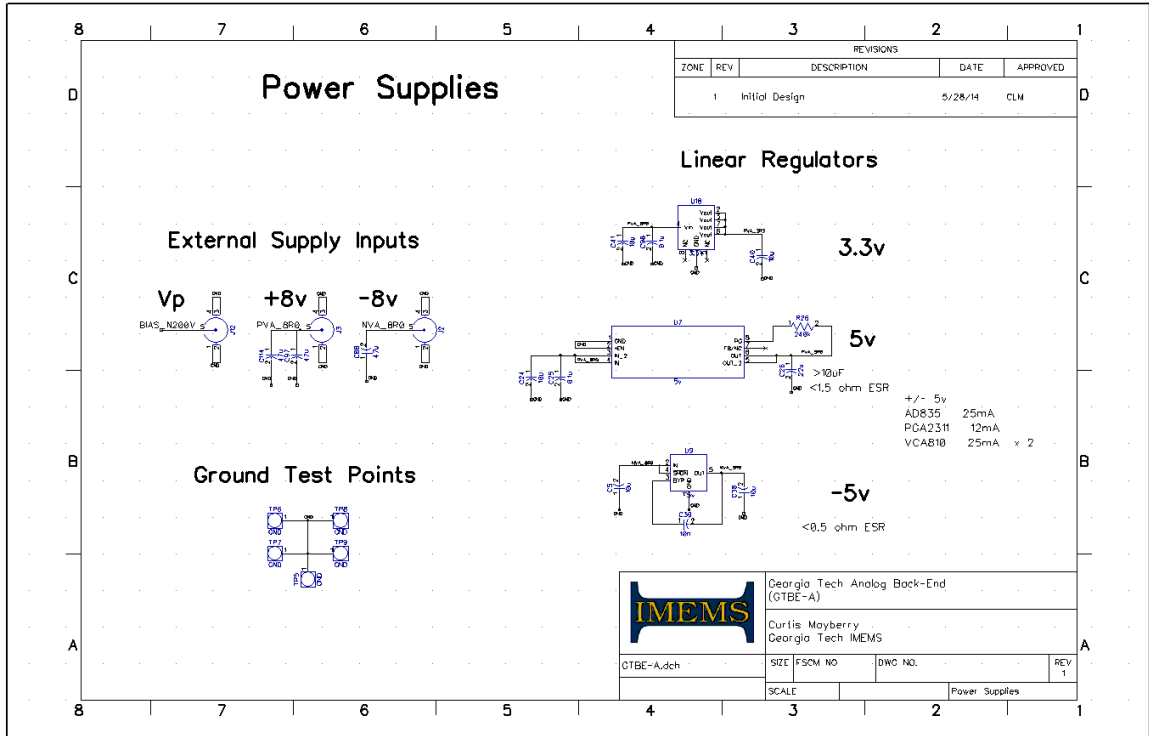
### E.3. Automatic Level Controller



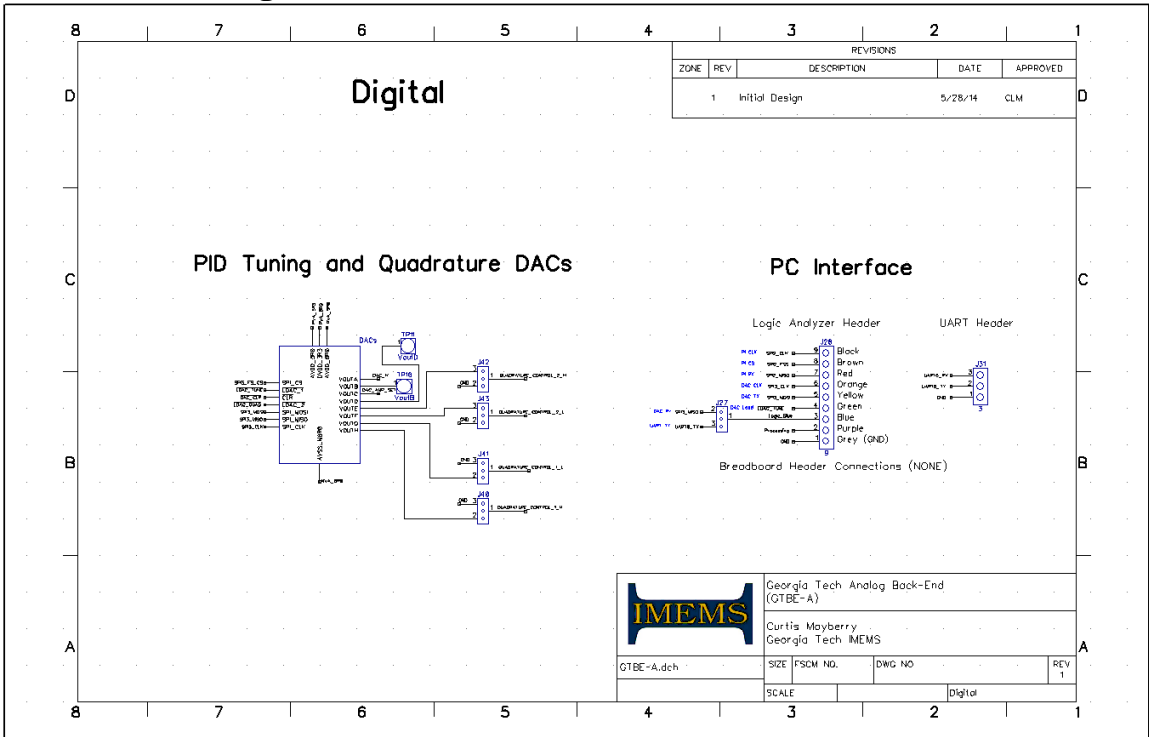
### E.4. Sense Channel



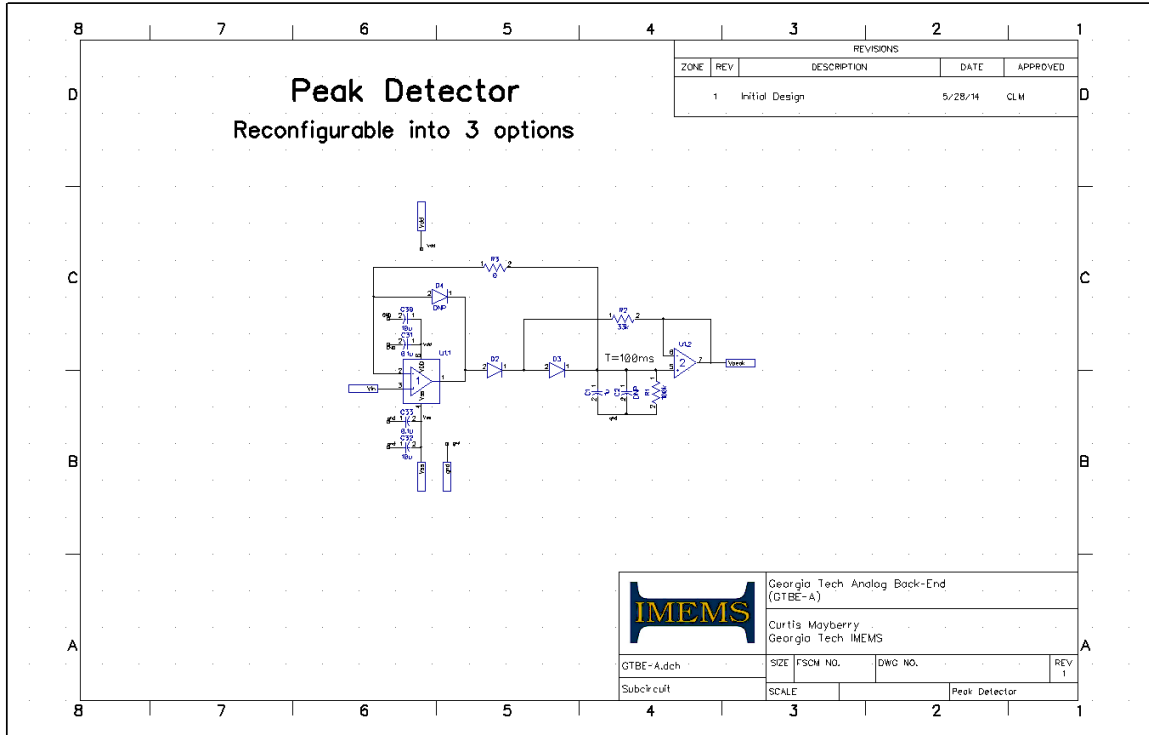
## E.5. Power Supplies



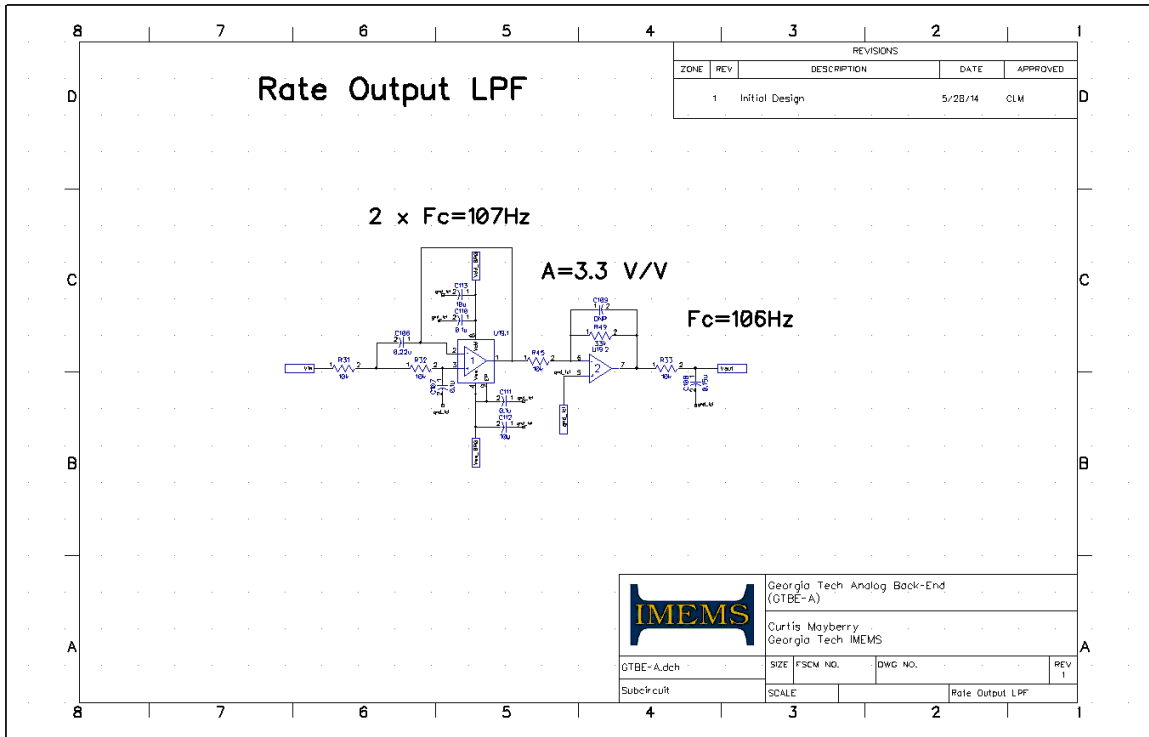
## E.6. Digital



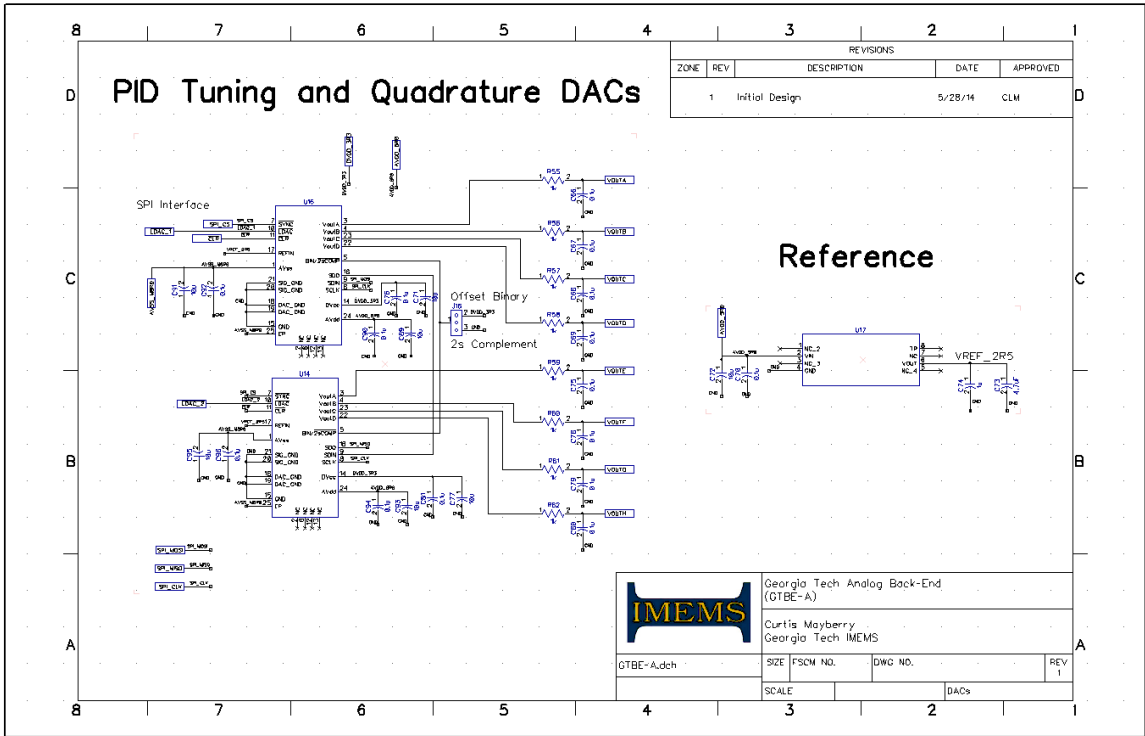
## E.7. Peak Detector



## E.8. Rate Output Low Pass Filter

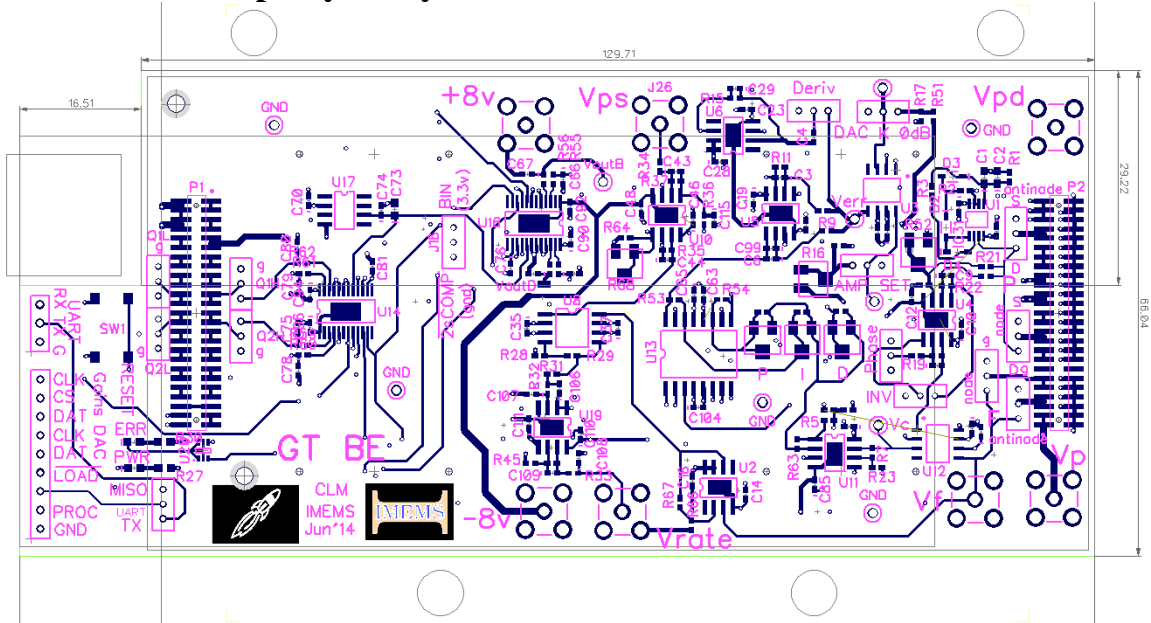


## E.9. PID Tuning and Quadrature DACs

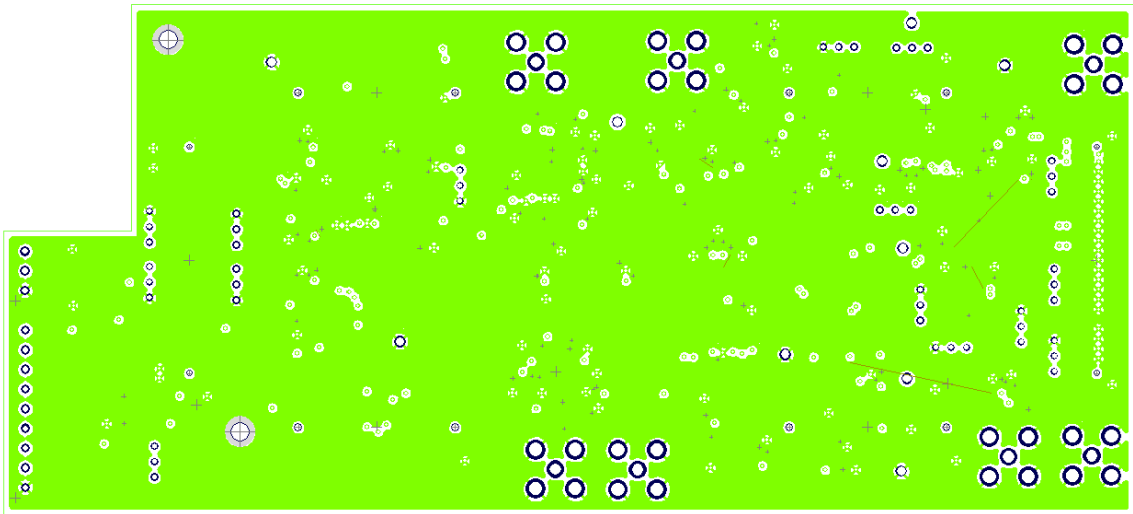


# Appendix F: Closed Loop Interface (GTBE-A) Layout

## F.1. Top Layer Layout



## F.2. Inner Layer 1 Layout



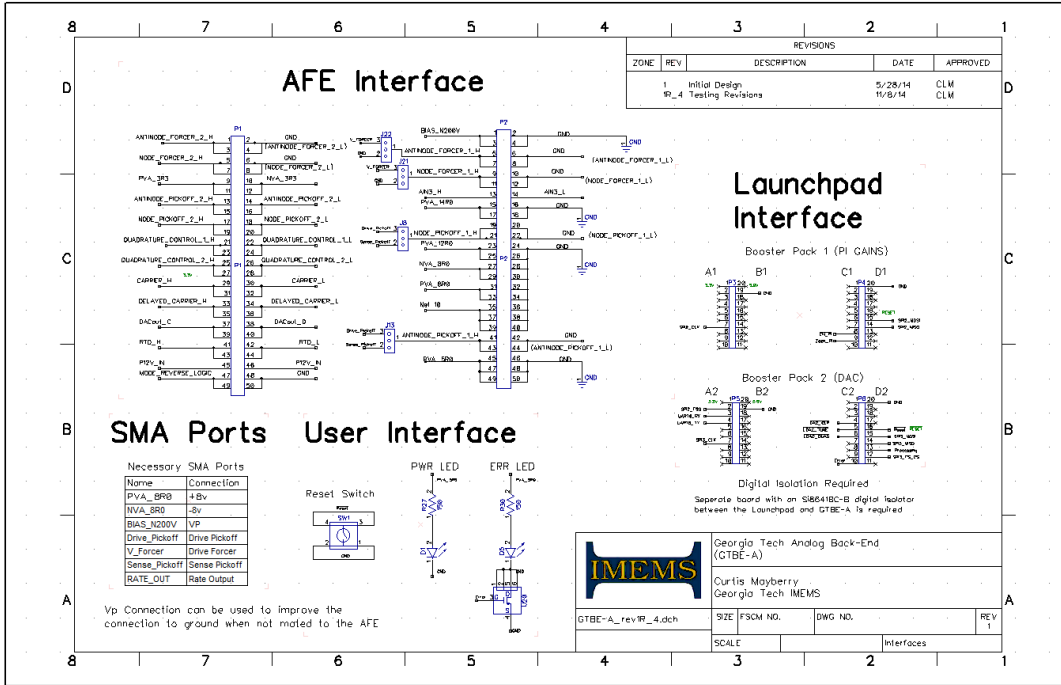




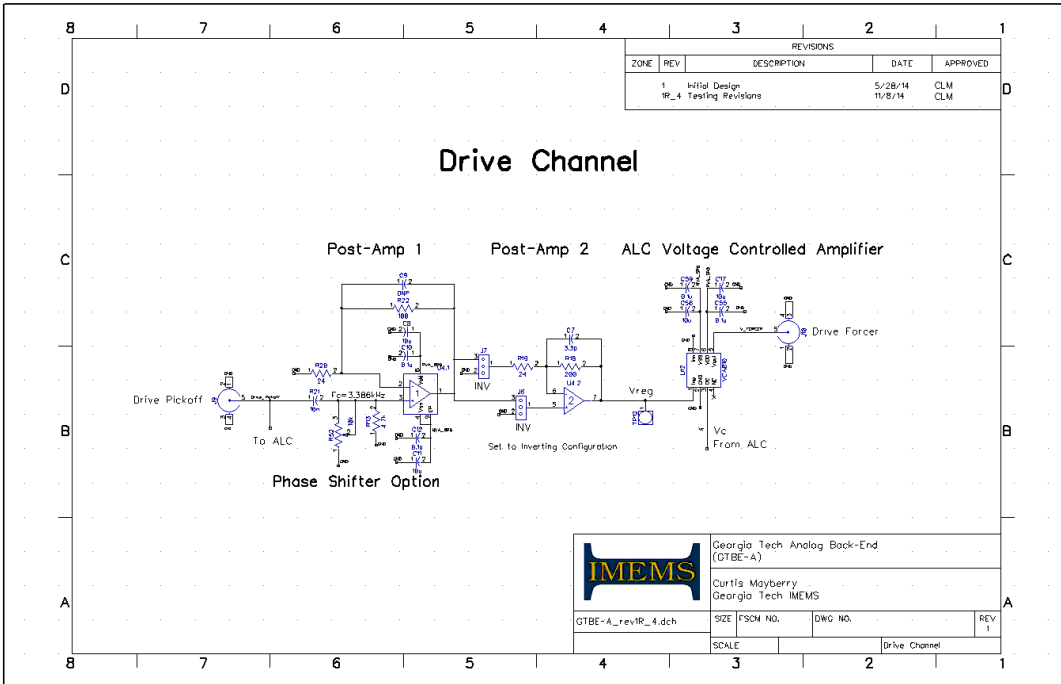
# Appendix G: Closed Loop Interface (GTBE-A)

## Revised Schematic

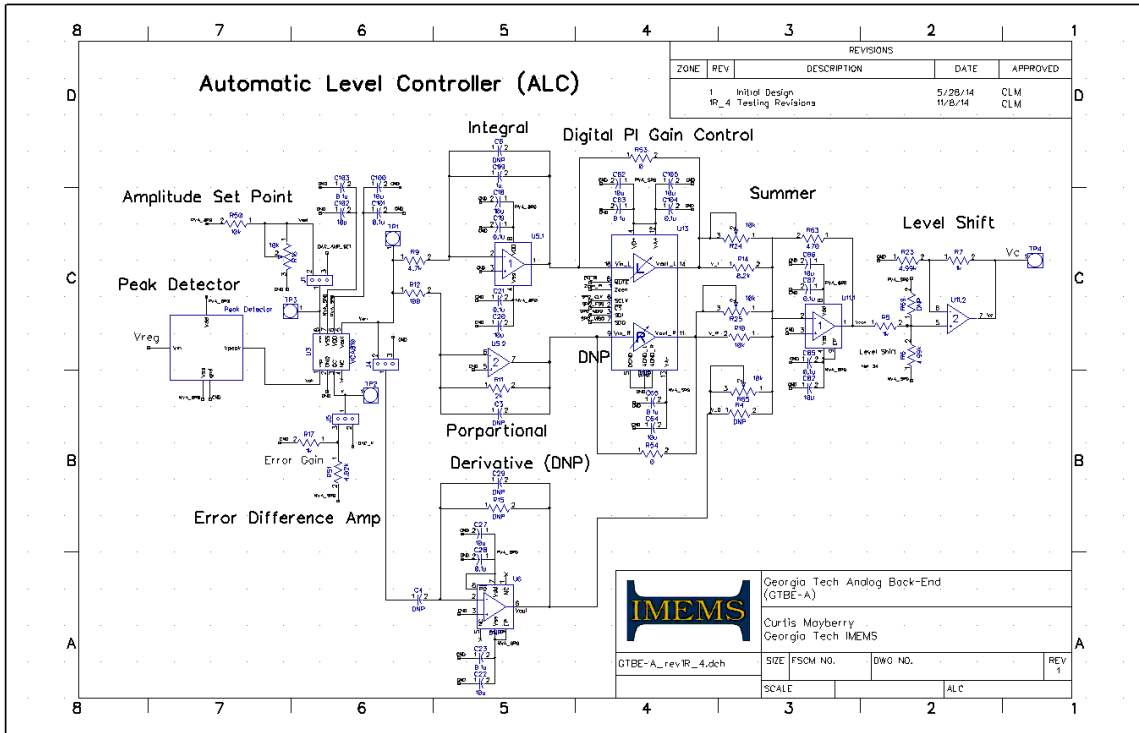
### G.1. Interfaces



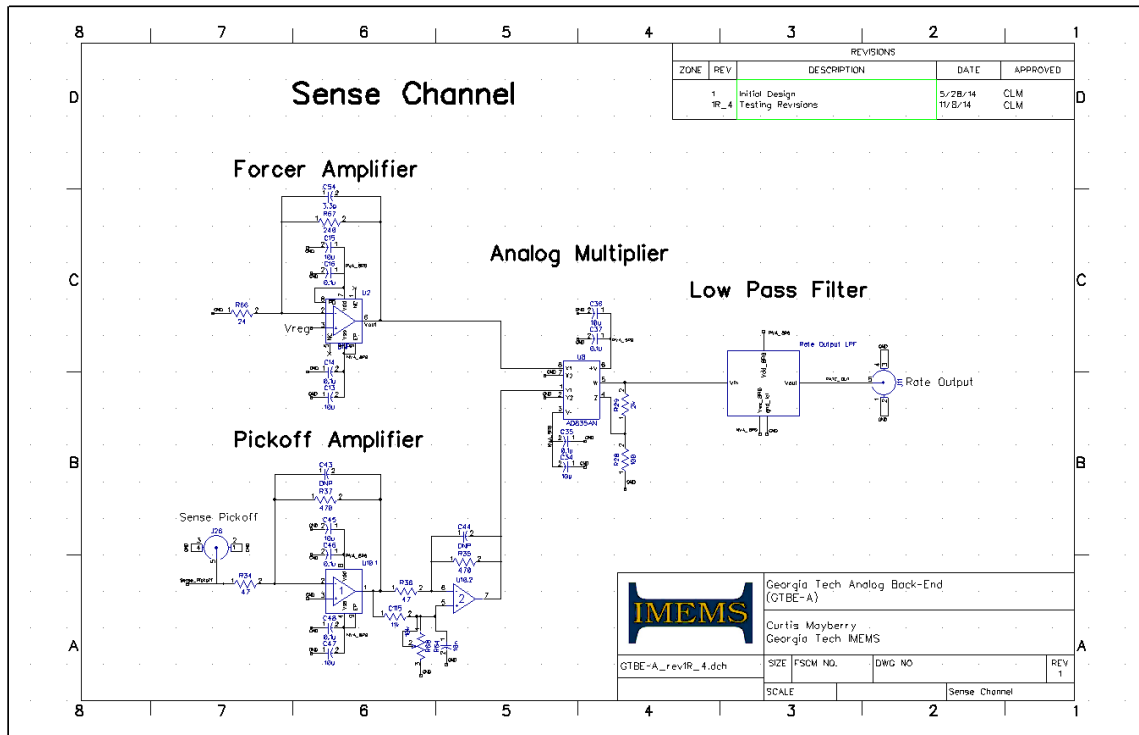
### G.2. Drive Channel



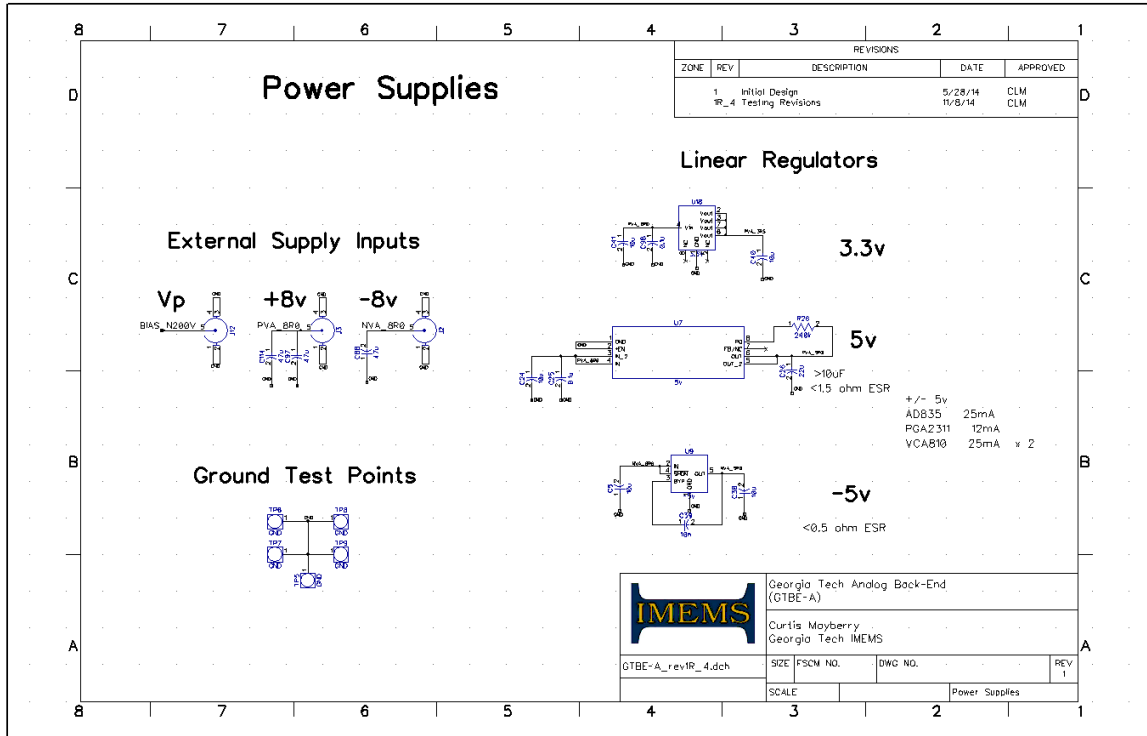
### G.3. Automatic Level Controller



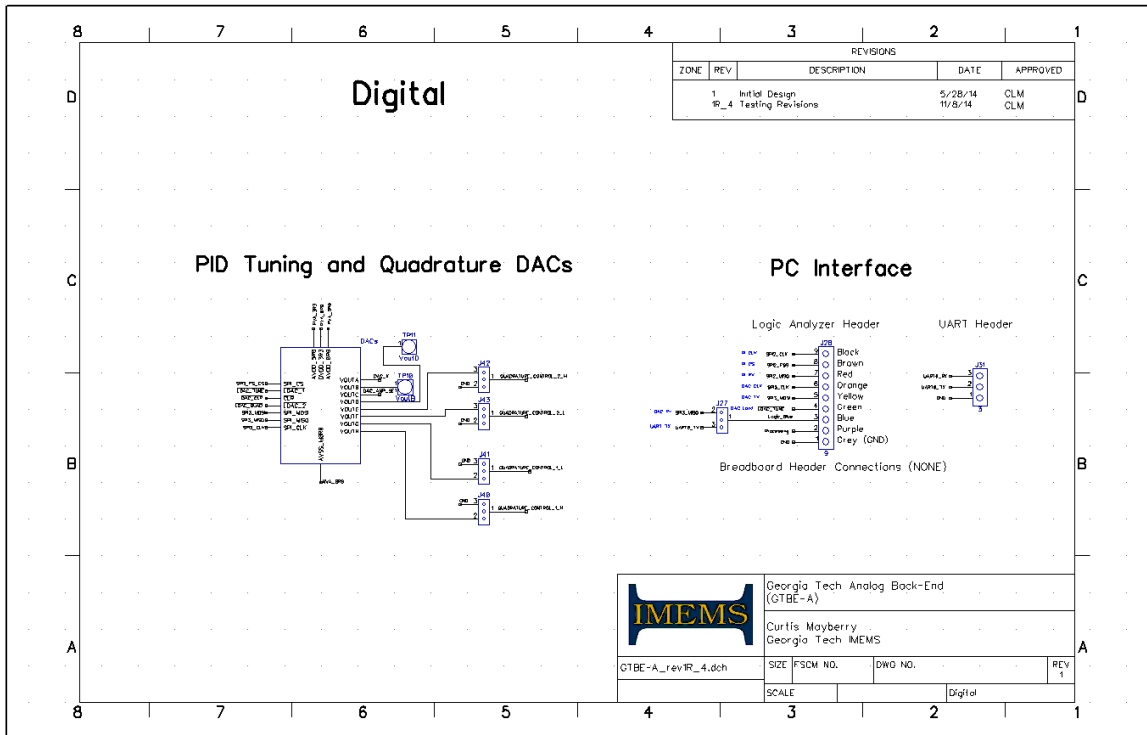
### G.4. Sense Channel



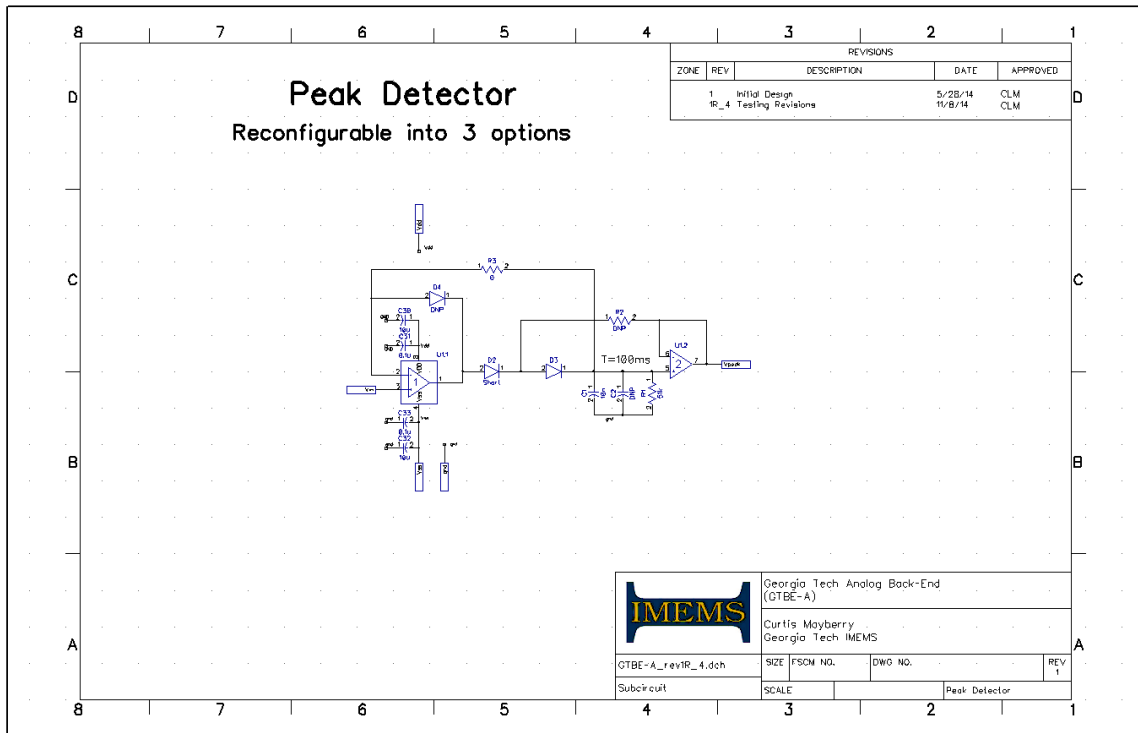
## G.5. Power Supplies



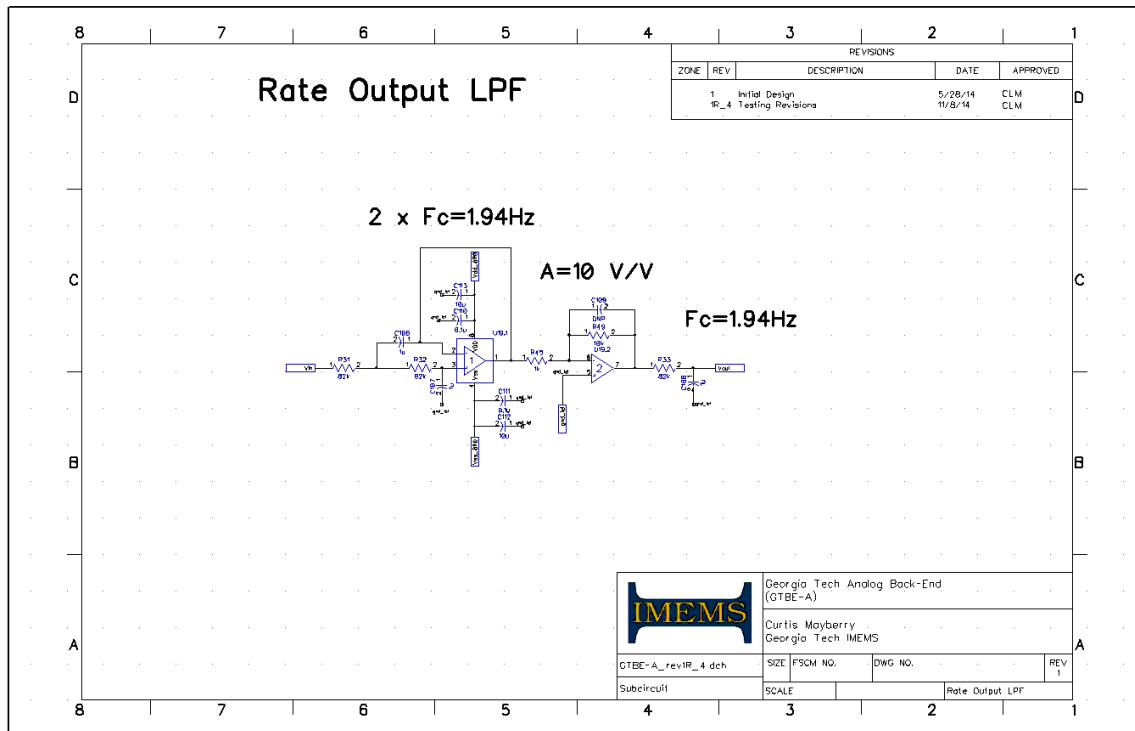
## G.6. Digital



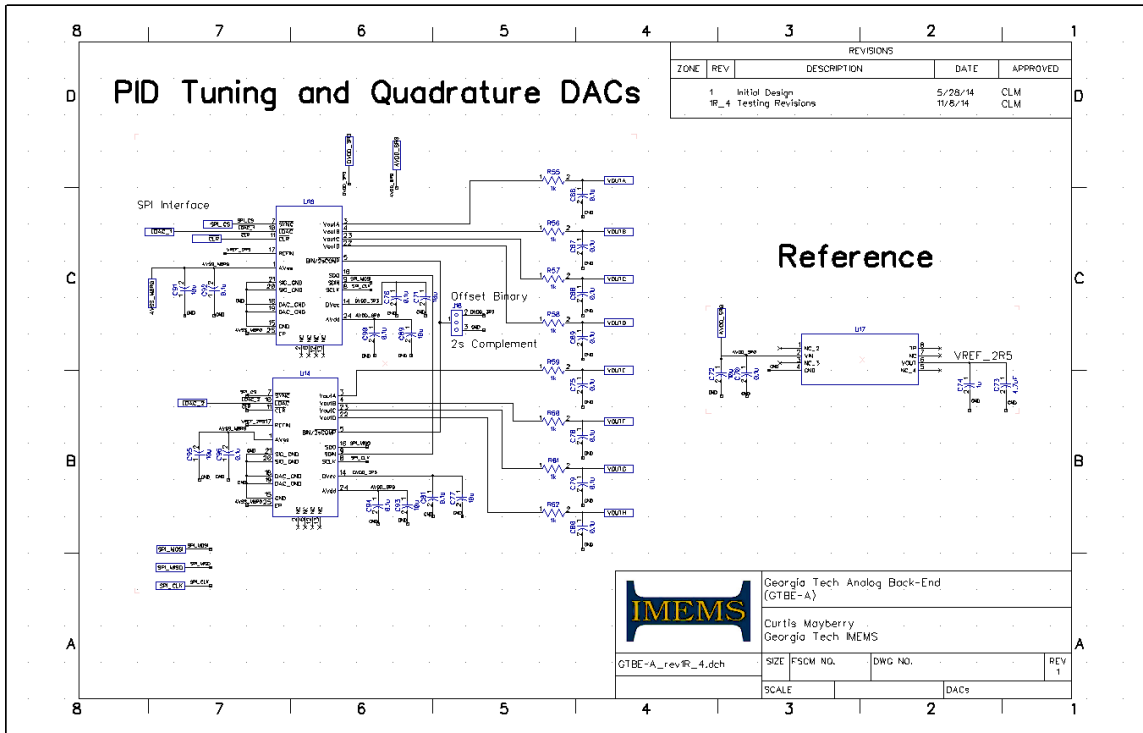
## G.7. Peak Detector



## G.8. Rate Output Low Pass Filter



## G.9. PID Tuning and Quadrature DACs



# Appendix H: gyroChar MATLAB Toolbox

## H.1. Toolbox Summary

A MATLAB toolbox was developed for analysis of gyroscope characterization data. The toolbox includes functions for plotting the frequency response, scale factor, and spectrum of the  $\mu$ HRG.

The toolbox is available at: <https://github.com/IMEMS/Public/tree/master/SOFTWARE-LIBRARIES/MATLAB/gyroChar%20Toolbox>

Function Summary:

- **gyroChar\_FreqResponse** – Plots the frequency response of both the drive and sense mode pickoffs and then both responses on the same plot. Works with .csv files saved from an Agilent E5061B network analyzer. It also displays the insertion loss and frequency of each peak.
- **gyroChar\_ScaleFactor** – Plots the scale factor from transient scale factor measurements.
- **gyroChar\_Spectrum** – Plots the spectrum measured on an Agilent 35670A dynamic signal analyzer.
- **gyroChar\_E5061B\_Bode** – Plots the frequency response from an Agilent E5061B network analyzer.

## H.2. Contents.m

```
% GYROCHAR
% Version 001 27-Nov-2014
%
% Toolbox for the processing of gyroscope characterization data.
%
% Curtis Mayberry
% Georgia Tech IMEMS Lab
%
% Files
% gyroChar_FreqResponse - plots the resonator frequency response
% gyroChar_ScaleFactor - gyroChar_ScaleFactor Plots rotation rate
%   scale factor and transient rate plots
% gyroChar_Spectrum - gyroChar_Spectrum - Generates the frequency
%   spectrum from dynamic signal analyzer data
% gyroChar_E5061B_Bode - imports data from the Agilent E5061B
%   network analyzer and generates a Bode plot
% gyroChar_Analysis_Example - An example analysis script utilizing
%   the gyroChar toolbox.
```

## Appendix I: Digital Control Firmware

The firmware for the digital control of the back-end provides digital control for the tuning voltages and digital control of the ALC PI gains. The firmware consists of a driver library and the main back-end interface control program.

**Driver Library (gtbelib):** The driver library has firmware drivers for a variety of devices, including the ADCs and PGA used in the back-end. It also contains several utilities for use with the Tiva C Series Launchpad microcontroller boards.

**Back-end Main Control Firmware (GTBEA\_basic):** Firmware for control of the analog back-end. It provides control of all the ADCs to provide the tuning voltages digitally. A PC is used to set the tuning voltages by communicating with the microcontroller through a USB connection.

The latest firmware is available on the IMEMS GIT repository:

<https://github.com/IMEMS/Public/tree/master/SOFTWARE-LIBRARIES>

## References

- [1] A. Shkel. (2011, September), Microtechnology Comes of Age. *GPS World*. Available: <http://gpsworld.com/defense-warfighter-microtechnology-comes-age/>
- [2] P. Shao, L. D. Sorenson, and F. Ayazi, "Wineglass-on-a-Chip," in *Solid-state Sensors, Actuators, and Microsystems Workshop (Hilton Head 2012)*, Hilton Head Island, SC, 2012, pp. 275-278.
- [3] P. Shao, V. Tavassoli, C.-S. Liu, L. Sorenson, and F. Ayazi, "Electrical Characterization of ALD-coated Silicon Dioxide Micro-hemispherical Shell Resonators," in *IEEE International Conference on Micro Electro Mechanical Systems (MEMS 2014)*, San Francisco, 2014, pp. 612-615.
- [4] L. D. Sorenson, X. Gao, and F. Ayazi, "3-D Micromachined Hemispherical Shell Resonators with Integrated Capacitive Transducers," presented at the IEEE International Conference on Micro Electro Mechanical Systems (MEMS 2012), Paris, France, 2012.
- [5] A. Heidari, M.-L. Chan, H.-A. Yang, G. Jaramillo, P. Taheri-Tehrani, P. Fonda, *et al.*, "Hemispherical Wineglass Resonators Fabricated from the Microcrystalline Diamond," *J. Micromech. Microeng.*, vol. 23, p. 125016, 2013.
- [6] M. M. Rahman, Y. Xie, C. Mastrangelo, and H. Kim, "3-D Hemispherical Micro Glass-shell Resonator with Integrated Electrostatic Excitation and Capacitive Detection Transducers," in *IEEE International Conference on Micro Electro Mechanical Systems (MEMS 2014)*, San Francisco, 2014.
- [7] P. Shao, C. L. Mayberry, X. Gao, V. Tavassoli, and F. Ayazi, "A Polysilicon Microhemispherical Resonating Gyroscope," *IEEE Journal of Microelectromechanical Systems*, pp. 762-764, 2014.
- [8] P. Shao, V. Tavassoli, C. L. Mayberry, and F. Ayazi, "A 3D-HARPSS Polysilicon Micro-hemispherical Shell Resonating Gyroscope: Design, Fabrication, and Characterization," *IEEE Sensors Journal (Under Review)*, 2014.
- [9] A. M. Shkel, "Type I and Type II Micromachined Vibratory Gyroscopes," in *Position, Location, And Navigation Symposium, 2006 IEEE/ION*, 2006, pp. 586-593.
- [10] A. D. Meyer and D. M. Rozelle, "milli-HRG Inertial Navigation System," in *Proc. IEEE/ION PLANS*, Myrtle Beach, SC, 2012.
- [11] D. Rozelle, "The Hemispherical Resonator Gyro: From Wineglass to the Planets", in *AAS/AIAA Space*, Savannah, Georgia, 2009.
- [12] M. Ferraresi, G. Giuffrida, and N. Palella, "Innovative MEMS Sensors in Advanced Positioning Systems," in *Advanced Microsystems for Automotive*, ed Switzerland: Springer International Publishing, 2013, pp. 329-339.
- [13] N. Yazdi, F. Ayazi, and K. Najafi, "Micromachined Inertial Sensors," *Proceedings of the IEEE*, vol. 86, pp. 1640-1659, 1998.
- [14] P. Aggarwal, *MEMS-based Integrated Navigation*. Boston: Artech House, 2010.
- [15] F. Ayazi, "A High Aspect-Ratio High-Performance Polysilicon Vibrating Ring Gyroscope," *Electrical Engineering*, 2000.
- [16] R. Lawler. (2014, iFixit cracks open an iPhone 6 Plus to get at the massive battery inside. *engadget*.
- [17] F. Ayazi, "Multi-DOF Inertial MEMS: From Gaming to Dead-reckoning," in *Transducers '11*, Beijing, China, 2011.
- [18] M. J. Klowden, "Chapter 10 - Locomotor Systems," in *Physiological Systems in Insects (Third Edition)*, M. J. Klowden, Ed., ed San Diego: Academic Press, 2013, pp. 475-527.

- [19] W. P. Chan, F. Prete, and M. H. Dickinson, "Visual Input to the Efferent Control System of a Fly's "Gyroscope"," *Science*, vol. 280, pp. 289-292, April 10, 1998 1998.
- [20] G. Nalbach, "Extremely non-orthogonal axes in a sense organ for rotation: Behavioural analysis of the dipteran haltere system," *Neuroscience*, vol. 61, pp. 149-163, 7// 1994.
- [21] A. Shkel and C. Acar, *MEMS Vibratory Gyroscopes: Structural Approaches to Improve Robustness*: Springer US, 2009.
- [22] M. N. Armenise, C. Ciminelli, F. Dell'Olio, and V. M. N. Passaro, *Advances in Gyroscope Technologies*. Berlin Heidelberg: Springer, 2011.
- [23] D. Meyer and M. Larsen, "Nuclear magnetic resonance gyro for inertial navigation," *Gyroscopy and Navigation*, vol. 5, pp. 75-82, 2014/04/01 2014.
- [24] A. Matthews and F. J. Rybak, "Comparison of hemispherical resonator gyro and optical gyros," *Aerospace and Electronic Systems Magazine, IEEE*, vol. 7, pp. 40-46, 1992.
- [25] P. Bouyer, "The centenary of Sagnac effect and its applications: From electromagnetic to matter waves," *Gyroscopy and Navigation*, vol. 5, pp. 20-26, 2014/01/01 2014.
- [26] Y. Paturel, J. Honthaas, H. Lefèvre, and F. Napolitano, "One nautical mile per month fog-based strapdown inertial navigation system: A dream already within reach?," *Gyroscopy and Navigation*, vol. 5, pp. 1-8, 2014/01/01 2014.
- [27] Hubi, "Corioliskraftanimation," vol. 200 x 283, Corioliskraftanimation.gif, Ed., ed. German Wikipedia, 2003, p. Illustration of the coriolis force.
- [28] C. Acar and A. M. Shkel, "Inherently robust micromachined gyroscopes with 2-DOF sense-mode oscillator," *Microelectromechanical Systems, Journal of*, vol. 15, pp. 380-387, 2006.
- [29] M. F. Zaman, A. Sharma, H. Zhili, and F. Ayazi, "A Mode-Matched Silicon-Yaw Tuning-Fork Gyroscope With Subdegree-Per-Hour Allan Deviation Bias Instability," *Microelectromechanical Systems, Journal of*, vol. 17, pp. 1526-1536, 2008.
- [30] M. S. Weinberg and A. Kourepenis, "Error sources in in-plane silicon tuning-fork MEMS gyroscopes," *Microelectromechanical Systems, Journal of*, vol. 15, pp. 479-491, 2006.
- [31] M. F. Zaman, "Degree-Per-Hour Mode-Matched Micromachined Silicon Vibratory Gyroscopes," Ph.D., Electrical and Computer Engineering, Georgia Institute of Technology, Atlanta, 2008.
- [32] F. Ayazi and K. Najafi, "A HARPSS polysilicon vibrating ring gyroscope," *Microelectromechanical Systems, Journal of*, vol. 10, pp. 169-179, 2001.
- [33] H. Johari and F. Ayazi, "Capacitive Bulk Acoustic Wave Silicon Disk Gyroscopes," in *Electron Devices Meeting, 2006. IEDM '06. International*, 2006, pp. 1-4.
- [34] H. Johari, J. Shah, and F. Ayazi, "High frequency XYZ-axis single-disk silicon gyroscope," in *Micro Electro Mechanical Systems, 2008. MEMS 2008. IEEE 21st International Conference on*, 2008, pp. 856-859.
- [35] S. Pourkamali, H. Zhili, and F. Ayazi, "VHF single crystal silicon capacitive elliptic bulk-mode disk resonators-part II: implementation and characterization," *Microelectromechanical Systems, Journal of*, vol. 13, pp. 1054-1062, 2004.
- [36] S. Tsanh-Hung, S. H. Nitzan, P. Taheri-Tehrani, M. H. Kline, B. E. Boser, and D. A. Horsley, "Silicon MEMS Disk Resonator Gyroscope With an Integrated CMOS Analog Front-End," *Sensors Journal, IEEE*, vol. 14, pp. 3426-3432, 2014.
- [37] H. Zhili, S. Pourkamali, and F. Ayazi, "VHF single-crystal silicon elliptic bulk-mode capacitive disk resonators-part I: design and modeling," *Microelectromechanical Systems, Journal of*, vol. 13, pp. 1043-1053, 2004.

- [38] J. Cho, J. A. Gregory, and K. Najafi, "High-Q, 3kHz Single-Crystal-Silicon Cylindrical Rate-Integrating Gyro (CING)," in *Micro Electro Mechanical Systems (MEMS), 2012 IEEE 25th International Conference on*, 2012, pp. 172-175.
- [39] J. Cho, J. A. Gregory, and K. Najafi, "Single-crystal-silicon vibratory cylindrical rate integrating gyroscope (CING)," in *Solid-State Sensors, Actuators and Microsystems Conference (TRANSDUCERS), 2011 16th International*, 2011, pp. 2813-2816.
- [40] J. A. Gregory, J. Cho, and K. Najafi, "Characterization and control of a high-Q MEMS Inertial Sensor Using Low-cost Hardware," in *IEEE/ION Position Location and Navigation Symposium (PLANS)*, Myrtle Beach, South Carolina, 2012.
- [41] J. Cho, T. Nagourney, A. Darvishian, B. Shiari, J.-K. Woo, and K. Najafi, "Fused Silica Micro Birdbath Shell Resonators with 1.2 Million Q and 43 Second Decay Time Constant," presented at the Solid-State Sensors, Actuators and Microsystems Workshop, Hilton Head Island, South Carolina, 2014.
- [42] J.-K. Woo, J. Y. Cho, C. Boyd, and K. Najafi, "Whole-angle-mode micromachined fused-silica birdbath resonator gyroscope (WA-BRG)," in *Micro Electro Mechanical Systems (MEMS), 2014 IEEE 27th International Conference on*, 2014, pp. 20-23.
- [43] J. Cho, J. K. Woo, J. Yan, R. L. Peterson, and K. Najafi, "A high-Q birdbath resonator gyroscope (BRG)," in *Solid-State Sensors, Actuators and Microsystems (TRANSDUCERS & EUROSENSORS XXVII), 2013 Transducers & Eurosensors XXVII: The 17th International Conference on*, 2013, pp. 1847-1850.
- [44] J. Y. Cho, J.-K. Woo, J. Yan, R. L. Peterson, and K. Najafi, "Fused-Silica Micro Birdbath Resonator Gyroscope (u-BRG)," *Microelectromechanical Systems, Journal of*, vol. 23, pp. 66-77, 2014.
- [45] D. Senkal, M. J. Ahamed, A. A. Trusov, and A. M. Shkel, "High temperature micro-glassblowing process demonstrated on fused quartz and ULE TSG," *Sensors and Actuators A: Physical*, vol. 201, pp. 525-531, 10/15/ 2013.
- [46] D. Senkal, M. J. Ahamed, A. A. Trusov, and A. M. Shkel, "Electrostatic and mechanical characterization of 3-D micro-wineglass resonators," *Sensors and Actuators A: Physical*, vol. 215, pp. 150-154, 8/15/ 2014.
- [47] D. Senkal, M. J. Ahamed, A. A. Trusov, and A. M. Shkel, "Achieving Sub-Hz Frequency Symmetry in Micro-Glassblown Wineglass Resonators," *Microelectromechanical Systems, Journal of*, vol. 23, pp. 30-38, 2014.
- [48] N. Mehanathan, V. Tavassoli, P. Shao, L. Sorenson, and F. Ayazi, "INVAR-36 Micro Hemispherical Shell Resonators," in *IEEE International Conference on Micro Electro Mechanical Systems (MEMS 2014)*, San Francisco, 2014, pp. 40-43.
- [49] L. D. Sorenson, P. Shao, and F. Ayazi, "Effect of Thickness Anistropy on Degenerate Modes in Oxide Micro-hemispherical Shell Resonators," in *IEEE International Conference on Micro Electro Mechanical Systems (MEMS 2013)*, Taipei, Taiwan, 2013.
- [50] P. Shao, "Microscale Hemispherical Shell Gyroscopes," PhD, Mechanical Engineering, Georgia Institute of Technology, Atlanta, GA, 2014.
- [51] A. Duwel, R. N. Candler, T. W. Kenny, and M. Varghese, "Engineering MEMS Resonators With Low Thermoelastic Damping," *Microelectromechanical Systems, Journal of*, vol. 15, pp. 1437-1445, 2006.
- [52] R. Lifshitz and M. L. Roukes, "Thermoelastic damping in micro- and nanomechanical systems," *Physical Review B*, vol. 61, pp. 5600-5609, 02/15/ 2000.
- [53] A. Sharma, "CMOS Systems and Circuits for Sub-degree Per Hour MEMS Gyroscopes," Doctor of Philosophy, Electrical and Computer Engineering, Georgia Institute of Technology Thesis, Atlanta, 2007.

- [54] D. W. Allan, "Statistics of atomic frequency standards," *Proceedings of the IEEE*, vol. 54, pp. 221-230, 1966.
- [55] IEEE, "IEEE Standard Specification Format Guide and Test Procedure for Single-Axis Laser Gyros," in *IEEE Std 647-2006 (Revision of IEEE Std 647-1995)*, ed, 2006, pp. 0\_1-83.
- [56] A. Sharma, M. F. Zaman, and A. Farrokh, "CMOS Systems and Interfaces for Microgyroscopes," in *Circuits at the Nanoscale*, ed: CRC Press, 2008, pp. 601-622.
- [57] M. H. Kline, Y. Yeh, B. Eminoglu, H. Najar, M. Daneman, D. A. Horsley, *et al.*, "Quadrature FM gyroscope," in *Micro Electro Mechanical Systems (MEMS), 2013 IEEE 26th International Conference on*, 2013, pp. 604-608.
- [58] S. A. Zotov, I. P. Prikhodko, B. Simon, A. A. Trusov, and A. M. Shkel, "Optimization of orbital trajectory for frequency modulated gyroscope," in *Inertial Sensors and Systems (ISISS), 2014 International Symposium on*, 2014, pp. 1-2.
- [59] S. A. Zotov, A. A. Trusov, and A. M. Shkel, "High-Range Angular Rate Sensor Based on Mechanical Frequency Modulation," *Microelectromechanical Systems, Journal of*, vol. 21, pp. 398-405, 2012.
- [60] M. Dalal, A. N. Shirazi, W.-K. Sung, and F. Ayazi, "Novel Readout Scheme for MEMS Vibratory Gyroscopes Based on Signal Phase Shift," presented at the Solid-State Sensors, Actuators and Microsystems Workshop, Hilton Head Island, South Carolina, 2012.
- [61] G. Casinovi, W.-K. Sung, M. Dalal, A. N. Shirazi, and F. Ayazi, "Electrostatic Self-Calibration of Vibratory Gyroscopes," in *IEEE International Conference on Micro Electro-mechanical Systems (MEMS 2012)*, Paris, France, 2012.
- [62] A. N. Shirazi, G. Casinovi, M. Dalal, and F. Ayazi, "Combined phase-readout and self-calibration of MEMS gyroscopes," in *Solid-State Sensors, Actuators and Microsystems (TRANSDUCERS & EUROSensors XXVII), 2013 Transducers & Eurosensors XXVII: The 17th International Conference on*, 2013, pp. 960-963.
- [63] A. Norouzpour-Shirazi, "Interface Circuits and Systems for Inertial Sensors," in *IEEE Sensors 2013: Tutorials*, Baltimore, MD, USA, 2013.
- [64] A. Sharma, M. F. Zaman, and F. Ayazi, "A 104-dB Dynamic Range Transimpedance-Based CMOS ASIC for Tuning Fork Microgyroscopes," *Solid-State Circuits, IEEE Journal of*, vol. 42, pp. 1790-1802, 2007.
- [65] R. T. M'Closkey and A. Vakakis, "Analysis of a Microsensor Automatic Gain Control Loop," in *American Control Conference*, San Diego, California, 1999, pp. 3307-3311.
- [66] J. Cui, X. Z. Chi, H. T. Ding, L. T. Lin, Z. C. Yang, and G. Z. Yan, "Transient response and stability of the AGC-PI closed-loop controlled MEMS vibratory gyroscopes," *Journal of Micromechanics and Microengineering*, vol. 19, p. 125015, 2009.
- [67] S. F. Wyse and R. E. Stewart, "Vibratory gyro bias error cancellation using mode reversal," ed: Google Patents, 2013.
- [68] M. H. Kline, Y. C. Yeh, B. Eminoglu, I. I. Izyumin, M. Daneman, D. A. Horsley, *et al.*, "MEMS gyroscope bias drift cancellation using continuous-time mode reversal," in *Solid-State Sensors, Actuators and Microsystems (TRANSDUCERS & EUROSensors XXVII), 2013 Transducers & Eurosensors XXVII: The 17th International Conference on*, 2013, pp. 1855-1858.
- [69] Swagelok. (2014). *Ultra-Torr-316: Ultra-Torr Vacuum Fittings*. Available: <http://www.swagelok.com/downloads/webcatalogs/en/ms-01-32.pdf>
- [70] T. Instruments. (2010). VCA810: High Gain Adjust Range, Wideband Variable Gain Amplifier datasheet. Available: <http://www.ti.com/lit/ds/symlink/vca810.pdf>
- [71] A. S. Sedra and K. C. Smith, *Microelectronic Circuits Revised Edition*: Oxford University Press, Inc., 2007.

- [72] A. Devices. (2010, AD835: 250MHz, Voltage Output, 4-Quadrant Multiplier. Available: [http://www.analog.com/static/imported-files/data\\_sheets/AD835.pdf](http://www.analog.com/static/imported-files/data_sheets/AD835.pdf)
- [73] A. Devices. (2011, AD5754: Complete, Quas, 16-bit , Serial Input, Unipolar/Bipolar Voltage Output DACs Datasheet. Available: [http://www.analog.com/static/imported-files/data\\_sheets/AD5724\\_5734\\_5754.pdf](http://www.analog.com/static/imported-files/data_sheets/AD5724_5734_5754.pdf)
- [74] T. Instruments. (2001, PGA2311: Stereo Audio Volume Control Datasheet. Available: <http://www.ti.com/lit/ds/symlink/pga2311.pdf>
- [75] J. A. Gregory, J. Cho, and K. Najafi, "MEMS rate and rate-integrating gyroscope control with commercial software defined radio hardware," in *Solid-State Sensors, Actuators and Microsystems Conference (TRANSDUCERS), 2011 16th International*, 2011, pp. 2394-2397.
- [76] J. A. Gregory, "Characterization, Control and Compensation of MEMS Rate and Rate-Integrating Gyroscopes," PhD, Electrical and Computer Engineering, University of Michigan, 2012.
- [77] D. Senkal, M. J. Ahamed, A. A. Truson, and A. Shkel, "Adaptable Test-bed for Characerization of Micro-wineglass Resonators," in *IEEE International Conference on Micro Electro Mechanical Systems (MEMS 2013)*, Taipei, Taiwan, 2013.